

Methods¹

M. Strasser, B. Dugan, K. Kanagawa, G.F. Moore, S. Toczko, L. Maeda, Y. Kido, K.T. Moe, Y. Sanada, L. Esteban, O. Fabbri, J. Geersen, S. Hammerschmidt, H. Hayashi, K. Heirman, A. Hüpers, M.J. Jurado Rodriguez, K. Kameo, T. Kanamatsu, H. Kitajima, H. Masuda, K. Milliken, R. Mishra, I. Motoyama, K. Olcott, K. Oohashi, K.T. Pickering, S.G. Ramirez, H. Rashid, D. Sawyer, A. Schleicher, Y. Shan, R. Skarbek, I. Song, T. Takeshita, T. Toki, J. Tudge, S. Webb, D.J. Wilson, H.-Y. Wu, and A. Yamaguchi²

Chapter contents

Introduction	1
Logging while drilling	6
Lithology	10
Structural geology	15
Biostratigraphy	16
Geochemistry	19
Physical properties	27
Paleomagnetism	35
Cuttings-core-log-seismic integration	37
X-ray computed tomography	38
References	38
Figures	44
Tables	67
Appendix A	78
Appendix A figures	81
Appendix A tables	87
Appendix B	89
Appendix B figures	90
Appendix B tables	92

¹Strasser, M., Dugan, B., Kanagawa, K., Moore, G.F., Toczko, S., Maeda, L., Kido, Y., Moe, K.T., Sanada, Y., Esteban, L., Fabbri, O., Geersen, J., Hammerschmidt, S., Hayashi, H., Heirman, K., Hüpers, A., Jurado Rodriguez, M.J., Kameo, K., Kanamatsu, T., Kitajima, H., Masuda, H., Milliken, K., Mishra, R., Motoyama, I., Olcott, K., Oohashi, K., Pickering, K.T., Ramirez, S.G., Rashid, H., Sawyer, D., Schleicher, A., Shan, Y., Skarbek, R., Song, I., Takeshita, T., Toki, T., Tudge, J., Webb, S., Wilson, D.J., Wu, H.-Y., and Yamaguchi, A., 2014. Methods. In Strasser, M., Dugan, B., Kanagawa, K., Moore, G.F., Toczko, S., Maeda, L., and the Expedition 338 Scientists, *Proc. IODP*, 338: Yokohama (Integrated Ocean Drilling Program). doi:10.2204/iodp.proc.338.102.2014

²Expedition 338 Scientists' addresses.

Introduction

This chapter documents the methods used for shipboard measurements and analyses during Integrated Ocean Drilling Program (IODP) Expedition 338. Riser drilling was conducted, including cuttings, mud gas, logging while drilling (LWD), and measurement while drilling (MWD) from 852.33 to 2005.5 meters below seafloor (mbsf) in IODP Hole C0002F, which had been suspended for 2 years since being drilled during IODP Expedition 326 by the D/V *Chikyu* in 2010 (Expedition 326 Scientists, 2011). Due to damage incurred to the intermediate flex joint of the upper riser assembly during an emergency disconnect sequence after the passing of a cold weather front with associated high winds and rapid changes in wind direction while in the high-current area, the Japan Agency for Marine-Earth Science and Technology (JAMSTEC)/Center for Deep Earth Exploration (CDEX) decided to discontinue riser operations at Site C0002 on 23 November 2012 (see “Operations” in the “Site C0002” chapter [Strasser et al., 2014b]). In light of this decision, we completed riserless coring in IODP Holes C0002H (1100.5–1120 mbsf), C0002J (902–926.7 mbsf), C0002K (200–286.5 mbsf), C0002L (277–505 mbsf), C0021B (0–194.5 mbsf), and C0022B (0–419.5 mbsf). Riserless LWD operations were completed in IODP Holes C0012H (0–710 mbsf), C0018B (0–350 mbsf), C0021A (0–294 mbsf), and C0022A (0–420.5 mbsf) (Table T1 in the “Expedition 338 summary” chapter [Strasser et al., 2014a]).

Previous IODP work at Site C0002 included logging and coring during Nankai Trough Seismogenic Zone Experiment (NanTro-SEIZE) Stages 1 and 2. LWD operations provided data from 0 to 1401.5 mbsf (Hole C0002A; Expedition 314 Scientists, 2009a) and 0 to 980 mbsf (Hole C0002G; Expedition 332 Scientists, 2011). Coring at Site C0002 previously sampled 0–203.5 mbsf (Holes C0002C and C0002D) and 475–1057 mbsf (Hole C0002B) (Expedition 315 Scientists, 2009b). During riser operations, we expanded the data sets at Site C0002. Gas from drilling mud was analyzed in near real time in a mud-gas monitoring laboratory and was sampled for postcruise research. Continuous LWD/MWD data were collected in real time for quality control and for initial assessment of borehole environment and formation properties. Recorded-mode LWD data provided higher spatial sampling of downhole parameters and conditions. Cuttings were sampled for standard shipboard analyses and shore-based research. Riserless



coring in Holes C0002H and C0002J–C0002L provided additional core samples (whole round and discrete) for standard shipboard and shore-based research.

Riserless operations at Site C0012 provided an extensive LWD data set for characterization of the sediment and basement conditions and properties. These logging data, which extend from 0 to 710 mbsf, complemented previous coring work at Site C0012 (Expedition 322 Scientists, 2010c; Expedition 333 Scientists, 2012b) and provided additional data in intervals where core recovery was sparse, especially within the basement.

Hole C0018B was the logging complement to coring in Hole C0018A. The LWD hole provided in situ characterization of mass transport deposits (MTDs) that were cored in Hole C0018A (Expedition 333 Scientists, 2012c) as part of the Nankai Trough Submarine Landslide History ancillary project letter. Hole C0018A sampled a stacked series of MTDs that are related to active tectonic processes. Logging data provide additional characterization of the features in the MTDs and the sediments that bound them, which allows additional constraints on the evolution of MTDs.

Riserless coring and LWD operations at Site C0021 (proposed Site NTS-1C) targeted a more proximal site for MTDs observed at Site C0018. Combined with LWD and core data obtained at Site C0018, LWD and coring at Site C0021 provide additional information on the nature, provenance, and kinematics of MTDs, as well as constraints on sliding dynamics and the tsunamigenic potential of MTDs.

Riserless coring and LWD operations at Site C0022 (proposed Site NT2-13A) were initiated to provide new constraints on the timing of activity along the splay fault. Site C0022 is located between IODP Sites C0004 and C0008 (Expedition 314 Scientists, 2009b; Expedition 316 Scientists, 2009b, 2009c). The objectives of the site were to obtain samples for precise age dating of sediment deformation at the tip of the splay fault to determine the age of activity. Core data provided samples for dating and deformation analysis. Logging data provided in situ conditions and resistivity images of deformation features.

Drilling operations

Site C0002

Reaming while drilling (RWD) was employed for the first time for scientific ocean drilling during Expedition 338 in order to allow cutting the 12¼ inch diameter pilot hole and opening the hole to 20 inches at the same time. This procedure was employed to facilitate installation of casing strings; however, these

strings were not installed because of the early termination of riser operations (see “**Operations**” in the “Site C0002” chapter [Strasser et al., 2014b]). There is a concentric hole opener between the bit and the underreamer (Fig. F1). The underreamer used to enlarge the hole to 20 inches was the National Oilwell Varco Anderreamer (Fig. F2). The design of the bottom-hole assembly (BHA) also included a complete LWD tool suite (Fig. F3). During riserless coring, no underreamer was used and the bit had a 12¼ inch diameter and used the standard rotary core barrel coring system for Holes C0002H, C0002I, and C0002J. Hole C0002K was cored with a hydraulic piston coring system (HPCS), extended punch coring system (EPCS), and extended shoe coring system (ESCS), whereas Hole C0002L was cored with the ESCS only (Table T1).

Site C0012

Hole C0012H was drilled with an LWD tool string similar to that used for logging in Hole C0002F (Fig. F3); however, the underreamer was not used. The 12¼ inch polycrystalline diamond compact (PDC) bit was employed to allow drilling in soft and semi-indurated sediment and into basement.

Site C0018

Hole C0018B was drilled with an LWD tool string similar to that used for logging in Hole C0002F (Fig. F3); however, neither the underreamer nor the sonicVISION were used. The 12¼ inch PDC bit was employed to allow drilling in soft and semi-indurated sediment.

Site C0021

Hole C0021A was drilled with the same LWD tool string that was used for logging in Hole C0018B (Fig. F3). Hole C0021B was cored with HPCS and EPCS.

Site C0022

Hole C0022A was drilled with the same LWD tool string that was used for logging in Hole C0018B (Fig. F3). Hole C0022B was cored with HPCS, EPCS, and ESCS.

Reference depths

Depths of each measurement or sample are reported relative to both the drilling vessel rig floor (rotary table) and the seafloor (mbsf) (see Table T2). These depths are determined by drill pipe and are correlated to each other by the use of distinct reference points. Drilling engineers refer to pipe length when reporting depth and report it as drilling depth below rig floor (DRF) in meters. Core depths are based on

drilling depth below rig floor to the top of the cored interval and curated length of the recovered core. During Expedition 338, core depths are converted to core depth below seafloor, Method A (CSF-A), which allows overlap relative to the cored interval and section boundaries in cases of >100% core recovery due to expansion after coring (Table T2) (IODP Depth Scales, www.iodp.org/program-policies/procedures/guidelines/). Cuttings and mud depths are reported as mud depth below rig floor (MRF) based on drillers depth (DRF) and the calculated lag depth of the cuttings (see below for additional details).

In referring to LWD results, depths are measured as LWD depth below rig floor (LRF) and reported as LWD depth below seafloor (LSF) (see “[Logging while drilling](#)” for further details). The depths reported in depths below rig floor (DRF, MRF, and LRF) are converted to depths below seafloor (drilling depth below seafloor [DSF] or CSF-A, mud depth below seafloor [MSF], and LSF, respectively) by subtracting water depth and the height of the rig floor from the sea surface, with corrections relative to drillers depth where appropriate. These depths below seafloor (DSF, CSF-A, MSF, and LSF) are therefore all equivalent. Seismic depths are reported in either time (s) or depth (m). For time sections, a two-way traveltime (s) below sea level scale is used. For depth sections, seismic depth below seafloor (SSF) or seismic depth below sea level (SSL) are used. In this report, meters below sea level (mbsl) or mbsf are used in place of the various depth measures, unless otherwise noted.

Cuttings and mud depths

During riser drilling, drilling mud circulates within the riser pipe between the drillship and the bottom of the hole. As the drill bit cuts through the formation, cuttings are suspended in the drilling mud and carried with the drilling mud, formation fluid, and formation gas back to the ship. A cuttings sample is assumed to be an average mixture of rock fragments and sediments from a sampled interval. The time between when the formation is cut by the drill bit and when these cuttings arrive at the ship is known as the “lag time,” which is a function of drilling mud pumping rate and annular mud volume, and is used to calculate the “lag depth.” At a constant pump rate, lag time and lag depth increase as the hole is deepened and the volume of circulating mud increases. All of the depths recorded for cuttings and mud gas in Hole C0002F have been corrected for this lag.

Depth precision estimates of cuttings

Cuttings were retrieved from 5 m depth intervals, and lag depth was calculated and calibrated as discussed above. Sample depths were recorded as the bit depth at the bottom of the 5 m advance, but samples are assumed to be representative of the 5 m interval. In addition to sampling over a 5 m advance interval, RWD produces cuttings from more than one depth at any moment in time. For the BHA employed during Expedition 338 riser operations, the offset between the bit and the cutting region of the concentric string tool was 38.3 m and the offset between the bit and the cutting portion of the underreamer was 43.8 m. Therefore, if the bit was producing cuttings at 100 mbsf, the concentric string tool was producing cuttings at 61.7 mbsf and the underreamer was producing cuttings at 56.2 mbsf. All cuttings were returned to the drillship for analyses and there was an unavoidable mixing of cuttings produced from three different intervals. This mixing created an uncertainty in the origin depth of the cuttings of at least 43.8 m and also created problems for interpreting thickness of layers that were drilled and percent of different lithologies that comprise those layers. To illustrate this complication, we provide three simplified scenarios. In each scenario, we consider drilling with a 12¼ inch bit and a 20 inch underreamer, neglecting the influence of the concentric string tool. Based on these size cutting tools, on a volumetric percent the bit is producing 38% of the cuttings and the underreamer is producing 62% of the cuttings. We then simulate drilling in three environments:

1. A two-layered system with 100% silty claystone overlaying 100% sandstone. The boundary between the layers is at 200 mbsf (Fig. F4A).
2. A 50 m thick, 100% sandstone layer that is bounded by 100% silty claystone on the top and bottom. The top of the sandstone is 200 mbsf and the bottom of the sandstone is 250 mbsf (Fig. F4B).
3. A 15 m thick, 100% sandstone layer that is bounded by 100% silty claystone on the top and bottom. The top of the sandstone is 200 mbsf and the bottom of the sandstone is 215 mbsf (Fig. F4C).

In Scenario 1, the cuttings indicate 100% silty claystone to 200 mbsf. At 200 mbsf, the first occurrence of sandstone appears but the cuttings indicate a formation that is 62% silty claystone and 38% sandstone (Fig. F4A). This is because as the bit produces cuttings in the sandstone at 200 mbsf, the underreamer produces cuttings in the silty claystone at

156.2 mbsf. Drilling progresses with this pattern until the underreamer and bit are in the sandstone (243.8 mbsf), at which point the cuttings indicate 100% sandstone. The net result is an interpreted lithostratigraphy from cuttings that correctly identifies the top of the sand horizon but does not accurately reflect the true sandstone content until the underreamer and bit are in the sandstone unit.

Similar to the first scenario, the cuttings produced in Scenario 2 indicate 100% silty claystone to 200 mbsf. Once the bit enters the sandstone unit, the cuttings indicate 62% silty claystone and 38% sandstone until the underreamer enters the sandstone unit (243.8 mbsf) (Fig. F4B). For the next 6.2 m, the underreamer and bit produce cuttings from the sandstone unit, so cuttings analysis shows 100% sandstone. Below the bottom of the sandstone unit (250 mbsf), the bit produces silty claystone cuttings and the underreamer produces sandstone cuttings, which yields a cuttings-interpreted lithology of 62% sandstone and 38% silty claystone from 250 to 293.8 mbsf. Once the underreamer is deeper than the sandstone layer, the cuttings indicate 100% silty claystone. The net effect is a smeared out sand horizon in the cuttings analysis that does not reflect the depth distribution (200–250 mbsf versus 200–293.8 mbsf) or sand content (100% versus 38%–100%) of the true formation.

For Scenario 3, we consider an isolated sandstone layer between silty claystone but assume the sandstone layer is only 15 m thick, which is smaller than the distance between the bit and the underreamer. Above 200 mbsf, the cuttings-inferred lithology is 100% silty claystone, but once the bit crosses into the sandstone (200–215 mbsf), the cuttings-inferred lithology is 62% silty claystone and 38% sandstone (Fig. F4C). Once the bit passes through the sandstone, both the bit and the underreamer produce silty claystone. As the underreamer enters the sandstone (bit at 243.8 mbsf), the underreamer produces sand cuttings whereas the bit produces silty claystone cuttings, so the cuttings-interpreted lithology is a 15 m thick layer that is 62% sandstone and 38% silty claystone. In this scenario, the interpreted lithology would be sandy interbeds (38% sand, 62% sand) within a silty claystone-dominated section, which does not accurately reflect the single, thin, 100% sandstone bed.

Although these three scenarios are simplified examples, they provide insight into the first-order complexity of interpreting formation lithology with cuttings that are produced during RWD operations. These complications, which are controlled by the diameter of the different tools, bed thickness, and bed composition, result in uncertainty in assessing the

true composition of individual beds and the true depth distribution of beds. Thus, sand content and sand thickness interpreted from cuttings data should be used as a guide but not as an absolute measure of the formation. Beyond the geometry of the system, erosion of the borehole wall from mud circulation adds another level of difficulty for interpretations. Such processes may spread out thickness and concentration variations significantly (see “**Physical properties**” in the “Site C0002” chapter [Strasser et al., 2014b] for more details).

By comparison, LWD data are acquired above the bit but below the underreamer, so the data provide petrophysical measurements over well-defined intervals that are not influenced by the underreamer but could be influenced by borehole enlargement because of borehole erosion. Therefore, cuttings data and logging data should be used in conjunction to help interpret lithology, composition, and bed thicknesses, always keeping in mind that the nature of RWD imparts a minimum of 43.8 m uncertainty and perhaps >80 m of uncertainty (see “**Physical properties**” in the “Site C0002” chapter [Strasser et al., 2014b]) in the origin depth of any cuttings sample.

Sampling and classification of material transported by drilling mud

A total of 312 cuttings samples were collected between 865.5 and 2004.5 mbsf during drilling in Hole C0002F (see Table T1 in the “Site C0002” chapter [Strasser et al., 2014b]). Cuttings were taken at every 5 m depth interval from the shale shakers. Drilling mud and mud gases were also regularly sampled during drilling (see “**Geochemistry**”). Mud gas, fluids, and cuttings samples were classified by drill site and hole using a sequential material number followed by an abbreviation describing the type of material. The material type identifiers are

SMW = solid taken from drilling mud (cuttings).

LMW = liquid taken from drilling mud.

GMW = gas taken from drilling mud.

Additional information of individual samples (e.g., cuttings size fraction) is provided in the comments section of the J-CORES database and reported in text as, for example, “338-C0002F-123-SMW, 1–4 mm” (for the 1–4 mm size fraction aliquot of the 123rd cuttings sample recovered from Hole C0002F during Expedition 338).

Influence of drilling mud composition on cuttings

Because of the recirculation of drilling mud and continuous production of formation cuttings and fluids, cuttings samples are contaminated. Expedition 319

Scientists (2010c) discussed the possible effects of contamination on different types of measurements. New observations of contamination and artifacts induced by riser and RWD operations and further quality assurance/quality control analysis were performed during Expedition 338 and reported in the individual methods and site chapters.

Cuttings handling

Every 5 m between 865.5 and 2004.5 mbsf, we routinely collected 3000–5000 cm³ of cuttings material from the shale shaker for shipboard analysis, long-term archiving, and personal samples for postcruise research. Varying initial sampling volume from the shale shaker relates to varying amounts of personal samples taken at a specific depth. Between 860 and 1075 mbsf (i.e., the interval that overlaps with the cored interval in Hole C0002B [Expedition 315 Scientists, 2009b]), all samples were processed following the procedure outlined below. Below 1075 mbsf, every other sample was kept as a “temporary archive” without further processing, and thus standard shipboard analyses were performed on a 10 m depth interval. Specific temporary archive samples were reintroduced into the cuttings processing flow at a later stage during the expedition to refine intervals of special interest identified by preliminary shipboard analysis. Unused temporary archive samples and an archive split of all processed cuttings samples were sent to the Kochi Core Center (KCC) in Kochi, Japan, for permanent archiving.

The standard cuttings laboratory flow is summarized in Figure F5. Unwashed cuttings samples were taken for the following objectives:

- 70 cm³ for lithology description,
- 30 and 100 cm³ for micropaleontology (calcareous nannofossils and radiolarians), and
- 400 cm³ for measuring natural gamma radiation (NGR) (see “Physical properties” in the “Site C0002” chapter [Strasser et al., 2014b] for further details) and archiving at the KCC core repository.

The remaining cuttings were washed gently with seawater in a 250 µm sieve at the core cutting area. Samples then were further washed and sieved with seawater using a 0.25, 1, and 4 mm mesh. During sieving, a hand magnet was used to remove iron contaminants originating from drilling tools and casing. Cuttings were separated by size fraction as 0.25–1 mm, 1–4 mm, and >4 mm. A split of the 1–4 mm and >4 mm fractions was used for bulk moisture and density (MAD) measurements. A volume of 220 cm³ of the 1–4 mm and >4 mm fractions was vacuum-dried. Aliquots (10 cm³) from each size fraction were

ground as bulk samples for X-ray diffraction (XRD), X-ray fluorescence (XRF), and geochemistry analysis (carbon and nitrogen). The remaining cuttings were described and analyzed for structures and lithology, including microscopy observation on thin sections from selected cuttings. Occasionally, after dividing and description, samples of interest that were divided by major and minor lithology were selected for additional XRD, XRF, and carbon and nitrogen analysis.

Drilling mud handling

Drilling mud samples were collected at two locations: mud tanks (LMT samples) and the mud return ditch. Sampling was conducted regularly every 2–3 days. Drilling mud samples were used for measuring background and contamination effects for NGR and total organic carbon (TOC) analysis (see “Physical properties” and “Geochemistry”).

Mud gas handling

Mud gas was extracted from drilling mud immediately after the mud returned from the borehole. A degasser with an agitator was installed on the bypass mud-flow line, and the gas extracted in the degasser chamber was pumped to the mud-gas monitoring laboratory via a polyvinyl chloride (PVC) tube. Analysis in the unit is described in “Geochemistry.”

Core handling

Standard IODP coring tools, including plastic core liners (diameter = 6.6 cm) were used during Expedition 338. Cores were usually cut into ~1.4 m sections in the core cutting area and logged and labeled by the shipboard curator.

Figure F6 shows the basic core processing flow chart. A small (~5–10 cm³) sample was taken for micropaleontology from the core catcher section. Time-sensitive samples for interstitial water analysis, microbiological analysis, and anelastic strain recovery (ASR) were identified as whole core sections in the core cutting area. These time-sensitive whole-round samples were then run through the X-ray computed tomography (CT) scanner, and a core watchdog ensured that the samples could be used and using them would not destroy any critical structures. Once approved, these whole-round samples were identified as core sections. Interstitial water sample lengths varied depending on core recovery and estimated volumetric fluid in the formation. Microbiological and ASR samples were ~10 cm long. All other core sections were taken to the core processing deck for standard X-ray CT scanning and whole-round multi-sensor core logger (MSCL-W) measurements.

After X-ray CT scanning and MSCL-W measurements, community whole-round samples up to ~20 cm in length were taken where intact, relatively homogeneous sections could be identified. The number of community whole rounds was limited by core recovery and core quality. All whole rounds were stored at 4°C and were allocated to individual shipboard and shore-based researchers at the end of the expedition. Adjacent to each community whole-round, ASR, and interstitial water sample, a cluster sample was taken. The cluster sample is used for routine MAD, XRD, XRF, carbon, nitrogen, and sulfur analyses on board the ship. Subsamples of the cluster samples were taken for shore-based research on clay-fraction XRD, grain size analysis, and potential thin sections.

The core sections remaining after whole-round core sampling were split into working and archive halves. Digital images of archive-half sections were taken with the photo image logger (MSCL-I) before visual core description (VCD) by sedimentologists and color reflectance measurement by the color spectroscopy logger (MSCL-C). Thermal conductivity measurements were performed on samples from the working half using the half-space method. Discrete cubes for *P*-wave velocity, impedance analysis, paleomagnetic measurement with superconducting rock magnetometer (SRM), and unconfined compressive strength (UCS) were sampled from the working half. Additional samples were taken for MAD, XRD, XRF, carbon, nitrogen, and sulfur analyses. After the expedition, all cores were transported in refrigerated storage for archiving at KCC.

Authorship of site chapters

The separate sections of the site chapters and methods chapter were written by the following shipboard scientists (authors are listed in alphabetical order):

Principal results: Shipboard Science Party
 Logging: Jurado, Olcott, Skarbeck, Tudge, Webb, Wilson, Wu
 Lithology: Heirman, Milliken, Mishra, Pickering, Ramirez, Sawyer (shore-based), Schleicher
 Structural geology: Fabbri, Geersen, Oohashi, Takeshita, Yamaguchi, Yehua
 Biostratigraphy: Hayashi (shore-based), Kameo (shore-based), Kanagawa, Motoyama (shore-based), Strasser, Toczko
 Geochemistry: Hammerschmidt, Masuda, Rashid, Toki
 Physical properties: Esteban, Hüpers, Kitajima, Song
 Paleomagnetism: Kanamatsu

Cuttings-core-log-seismic integration: Dugan, Moore, Olcott, Wilson

Logging while drilling

LWD and MWD tools continuously record in situ physical properties and downhole drilling parameters that can be analyzed (1) during drilling (using uphole mud pulse data transmission) and (2) shipboard after recovering memory data from the BHA. These measurements can be tied to core, cuttings, and seismic data to help define lithofacies, structure, and physical properties (see “[Cuttings-core-log-seismic integration](#)”). During Expedition 338, LWD and MWD data acquisition was conducted under contract by Schlumberger Drilling and Measurements Services in five holes: C0002F (852.33–2005.5 mbsf), C0012H (0–709.0 mbsf), C0018B (0–350.0 mbsf), C0021A (0–294.0 mbsf), and C0022A (0–420.5 mbsf). These measurements were interpreted in conjunction with LWD and core data collected during previous IODP NanTroSEIZE expeditions (Expedition 314 Scientists, 2009a; Expedition 322 Scientists, 2010c; Expedition 333 Scientists, 2012b).

The LWD and MWD tools used were Schlumberger’s arcVISION, geoVISION, sonicVISION, and TeleScope. LWD and MWD data were obtained to provide a wide range of in situ measurements and drilling parameters, including gamma ray, azimuthal resistivity images, annular pressure and temperature (all logged holes), and sonic slowness (only in Holes C0002F and C0012H). The advantage of LWD/MWD over wireline logging is that measurements are taken very soon after the borehole is drilled, thus minimizing the effects of disturbance and invasion of drilling mud into the formation. Combining these measurements with surface drilling parameters allows for improved real-time monitoring of drilling progress and assessment of data quality. The configuration of the BHA for each site is shown in Figure [F3](#). Acronyms and tool specifications can be found in Tables [T3](#), [T4](#), and [T5](#).

LWD systems and tools

LWD equipment is powered by battery, and data are recorded on an erasable chip located in the tool string. During drilling, selected data are transmitted to the surface by a modulated pressure wave in the drilling mud, allowing for real-time data analysis and monitoring of drilling conditions. Because of bandwidth limitations on mud pulse transmission, the real-time data are a sample of the full data set. The complete data set is only available after the BHA is

recovered and the data are downloaded from the tool memory.

geoVISION

Schlumberger's geoVISION tool (Fig. F3), the primary LWD tool, measures natural gamma ray emission and resistivity of the formation. The geoVISION tool provides five different resistivity measurements. The bit, ring, and three button resistivity measurements provide different depths of investigation into the formation (Table T4). Bit resistivity uses the tool and bit as a measuring electrode, allowing current from the lower transmitter to flow through the bit and return to the drill collar farther up the tool. The vertical resolution is 12–24 inches (30.5–61 cm). Ring resistivity uses two transmitter coils to produce a current that flows out of the ring electrode and into the formation with a vertical resolution of 2–3 inches (5.0–7.6 cm) and a 7 inch (17.8 cm) depth of investigation (Schlumberger, 2007).

Button resistivity consists of three button electrodes, each 2.5 inches (6.4 cm) in diameter with vertical resolution of 2–3 inches (5.0–7.6 cm). The buttons are arranged vertically along the tool at an increasing distance from the transmitter, providing shallow (1 inch penetration), medium (3 inch penetration), and deep (5 inch penetration) resistivity measurements (Schlumberger, 2007) (Table T4). The tool acquires azimuthal readings as it rotates and determines its orientation referenced to Earth's magnetic field using accelerometers and magnetometers. Following data download, 360° images of the borehole wall can be generated. Interpretations of bedding and fracture orientation can be made from these images.

The geoVISION tool also measures azimuthal natural gamma ray emission by means of a NaI scintillation detector. The measurements have a 90° resolution and a depth of investigation of 5–15 inches (12.7–38.1 cm) (Schlumberger, 2007).

arcVISION

Schlumberger's arcVISION tool (Fig. F3) measures gamma ray, azimuthal resistivity, and pressure and temperature in the annulus. During Expedition 338, the arcVISION tool was primarily used to measure annular temperature and annular pressure while drilling with an accuracy of $\pm 0.5^\circ\text{C}$ and 1 psi (6.895 kPa or 0.07 kg/cm²), respectively (Schlumberger, 2010a). Annular pressure data were used to calculate the equivalent circulating density, which is the density of the drilling fluid during pumping. Changes in downhole pressure can reveal flow from or into the formation. Such pressure changes and flows are re-

lated to formation pressure and permeability and may indicate the presence of fractures.

The arcVISION tool can also measure gamma ray and resistivity attenuation (Schlumberger, 2011). These data were acquired during Expedition 338 as a backup to be released by Schlumberger in the event that the geoVISION tool failed.

sonicVISION

Schlumberger's sonicVISION tool (Fig. F3) measures the traveltime (Δt) of acoustic waves transmitted through the formation. The measurement range, converted to slowness, is 40–230 $\mu\text{s}/\text{ft}$ (equivalent to *P*-wave velocities of 7.6–1.3 km/s), although the actual measurement range depends on the type of drilling mud used (Table T5). Four azimuthal receivers obtain full waveform acoustic signals emitted by a transmitter (Schlumberger, 2010b). The compressional and shear wave traveltimes are sent uphole in real time and used to create a semblance plot. Problems may arise with the sonic tool when measuring very slow formations with compressional velocity similar to or less than that of the drilling mud. No shear wave data were available in the slow formations.

Because of operational constraints, the sonicVISION tool was not available for use at Sites C0018, C0021, or C0022.

Onboard data flow and quality check

The LWD tools record data at a preset sampling rate. The sampling rate was 15 s at Site C0002 and 10 s at Sites C0012, C0018, C0021, and C0022. For standard interpretation, LWD and MWD data need to be referenced to meters below the seafloor. Schlumberger's integrated logging and drilling surface system allows the rate of penetration (ROP) and depth of the drill string to be determined using the length of the drill string and derrick top drive position. To minimize errors in data related to heave and to increase the accuracy of the weight on bit (WOB), a crown-mounted motion compensator is installed on top of the derrick.

The real-time data, in both time and depth, were provided every 6 h to allow for preliminary analysis. This was particularly important for Hole C0002F, where deep drilling prevented quick recovery of the memory data. After the tools were recovered, the memory data were downloaded and the time measurements were converted to depth (referenced to the rig floor, DRF). Data were converted to depth referenced to the seafloor (LSF) by determining the position of the seafloor from a break in the gamma ray log (and resistivity logs, when available). Time and

depth data were provided to the Shipboard Science Party with the time data in log ASCII standard (LAS) format and the depth data in digital log information standard (DLIS) and LAS formats.

Data quality check

The Logging Staff Scientist documented the LWD/MWD operations and performed initial quality assessment (highlighting any abnormalities). Data quality was also assessed by a detailed analysis of the shallow and deep button resistivity scalar logs. This allowed estimations of hole conditions (caving, washout, bridge, or invasion) and the possible impact of hole conditions on logging data quality. Results of these and other detailed quality assessment of borehole images (mostly shallow, medium, and deep button resistivity images and natural gamma ray) were documented by the Logging Staff Scientist.

Quality of LWD/MWD data was assessed by cross-correlating available logs. There were two types of logs available:

- Drilling control logs, including surface drilling parameters (e.g., ROP, surface WOB, hook load, and standpipe pressure) and downhole drilling parameters (e.g., collar [bit] rotation, hole deviation, radial shock rate, tangential shock rate, shock peak, and stick-slip indicator); and
- Geophysical control logs such as gamma ray, annular pressure, and annular temperature.

In high stick-slip zones, resistivity image quality can be affected. Additionally, because all measurements, even those recorded by the same tool, are not sampled at the same time, inadequate heave compensation and irregular movement (vibration, shocks, or bending) of the BHA can result in a local depth shift between measurements of up to several tens of centimeters.

Real-time observation of logging data for quality control

During data acquisition, the Logging Staff Scientist and logging scientists continuously monitored the real-time data feed and closed-circuit television of the rig floor and recorded important observations of changes in drilling and/or logging parameters on logging watchdog sheets. The purpose of monitoring real-time data was to perform an initial quality check on the data and to track events (e.g., time off bottom) that could affect the log response.

Log characterization and lithologic interpretation

LWD measurements provide in situ and real-time petrophysical information on rocks and pore fluids. Changes in the log response (e.g., amplitude and/or frequency of the signal) are commonly associated with changing composition and/or texture of rocks. Qualitative and quantitative methods were used for logging unit characterization.

Lithologic characterization and definition of logging units

Logging unit boundaries and bedding information were defined from borehole images and scalar LWD logs. Rock textures and structures were analyzed on borehole images. Composition information was derived mainly from variations in the gamma ray data, and textural variations were based on the sonic logs and resistivity images.

The first approach to unit definition was identification of the boundaries separating sections of different log responses, indicating distinct changes in rock properties. The full suite of available LWD data was used for this analysis, and the integrated interpretation allowed

- Definition and characterization of logging units, subunits, and unit boundaries;
- Identification of compositional features and trends within each unit; and
- Interpretation of the log data in terms of geological features (fractures, faults, transitions, sequences, and likely lithologic composition).

The gamma ray data were primarily used to determine lithology from unit scale to bed scale, with consideration of coincident changes in the resistivity and sonic logs (where available). In particular, the identification of sand-rich intervals (low gamma ray), clay-rich intervals (high gamma ray), or alternating beds of sand and clay was a primary element of the interpretation. Borehole images provided useful information on bedding, sedimentary structures, bed boundaries, unconformities, fractures, and faults. The defined logging units were compared to core, cuttings, and seismic data from previous IODP expeditions (Expedition 314 Scientists, 2009a; Expedition 322 Scientists, 2010c; Expedition 333 Scientists, 2012b) to further refine the interpretations (see “**Lithology**” and “**Cuttings-core-log-seismic integration**”).

Log-based structural interpretation

Shallow, medium, and deep resistivity borehole images were generated using GeoFrame 4.4, where static resistivity images were processed with 128 color gradation and the dynamic resistivity images were processed with 128 color gradation and a window length of 1 m. Static normalization is useful to see overall changes in resistivity in a single borehole, as it displays a color scale covering the entire range of resistivity (0.2–200 Ωm) for a single borehole. Dynamic normalization develops a color scale for a specific interval of resistivity and thus is useful for highlighting subtle details in a log such as changes in facies or lithology, fracture resistivity, or compressional borehole breakout width. The statically normalized shallow, medium, and deep button resistivity images were the primary images used for structural and geomechanical analyses.

Structural analysis was performed on the processed resistivity images using GMI Imager (Geomechanics International Inc.), Geolog/Geomage (Paradigm Geotechnology B.V.), and Petrel (Schlumberger). These software packages allow the azimuthal button resistivity measurements to be displayed as unwrapped, 360° images of the borehole wall and also allow 3-D borehole visualization.

Vertical resolution for LWD resistivity images is ~8–12.5 cm if ROP is maintained at ~20–30 m/h with a sampling interval of 10 or 15 s. Resistivity contrasts in the formation determine whether a geological feature can be identified on images. Planar surfaces appear as sinusoidal curves in unwrapped resistivity images, and nonplanar surfaces appear as irregular curves. To determine the dip and azimuth of planar features such as fractures, faults, and bedding, sinusoids were fitted to features using log interpretation software. Features were classed based on type, width, and shape and as conductive or resistive with care taken not to misinterpret artifacts created by inadequate heave compensation or rotational or vertical stick-slip. Because of the lack of an independent caliper measurement, the borehole size was set to match the bit size (12¼ inch) and assumed to be constant. This assumption potentially introduces a small error in the dip angles with dip overestimated in zones of enlarged borehole size. Therefore, all reported dip angles should be considered as a maximum bound.

Fractures were classified as conductive or resistive in comparison to background resistivity. Only unambiguously resistive or conductive fractures were classified. Features were classified as fractures when dip varied dramatically relative to bedding or where there was clear crosscutting of other features. Frequency of occurrence and distribution of azimuth were also examined. Results were compared to other

geophysical logs and cores to help interpret lithology, deformation style, and physical properties (see “[Cuttings-core-log-seismic integration](#)”).

Borehole wall analysis from LWD resistivity images

Borehole breakouts and drilling-induced tensile fractures (DITFs) can be used to determine stress orientation in the borehole. The principal stresses near the borehole are changed (in both orientation and magnitude) from the original principal stresses before drilling, which are equal to the far-field principal stresses, due to excavation of the borehole and the creation of a free surface. The change in principal stresses by drilling causes formation of borehole breakouts and DITFs at the borehole. In a vertical wellbore, the far field vertical stress (S_v) and two horizontal principal stresses (S_{hmin} and S_{hMAX}) are defined as azimuthal stress at the borehole wall by the Kirsch (1898) equations. Compressional borehole breakouts form when the maximum hoop stress exceeds the formation strength. Breakouts appear in resistivity images as parallel, vertical, conductive features 180° around the borehole from each other in a vertical borehole where the vertical (or overburden) stress is one of principal stresses. The minimum hoop stress is 90° from the position of borehole breakouts or parallel to the direction of the maximum horizontal stress (S_{hMAX}). Moving azimuthally around the borehole from the orientation of compressional borehole breakouts, or the orientation of S_{hmin} , the effective stress approaches zero. If the hoop stress drops below zero or becomes tensional instead of compressional, DITFs form parallel to the S_{hMAX} direction when the tensional strength of the rock is exceeded, creating vertical paired cracks in the formation (Zoback, 2007).

Orientation of breakouts and DITFs were analyzed in shallow, medium, and deep button resistivity images using GMI Imager. Azimuth and width of breakouts and DITFs were measured in degrees with respect to north. A benefit of LWD images is the full coverage of the borehole wall, which makes it possible to identify borehole conditions. However, the resistivity image quality is influenced by vertical shifting because of sudden changes in drilling rig elevation by heave and missing pixels. The stick-slip indicator curve measured while drilling is essential for interpreting such anomalies and bad data in the images. The vertical extent of borehole breakouts and DITFs was compared to (a) lithologic interpretations to infer changes in strength and/or pore pressure of formation and (b) MWD drilling parameters to investigate borehole stability, overpressure zones, and formation strength.

Physical properties

Estimation of porosity and bulk density from resistivity

No neutron density tool was available during Expedition 338; therefore, porosity (ϕ) and bulk density (ρ_b) were estimated from LWD resistivity at the bit. Bit resistivity was used because it has a large depth of investigation, and its proximity to the BHA drill bit should minimize the effects of drilling-induced changes in the formation. Porosity was calculated from resistivity using Archie's law (Archie, 1947):

$$\phi = (aR_f/R)^{1/m}, \quad (1)$$

where

- R = bulk resistivity (LWD bit resistivity),
- R_f = pore fluid resistivity,
- a = empirical constant, and
- m = cementation factor (empirical constant), related to the connectivity of pore spaces.

Archie parameters estimated for Hole C0002A during IODP Expedition 314 (Expedition 314 Scientists, 2009a) were applied for Holes C0002F and C0021B. In Holes C0012H, C0018B, and C0022B, Archie parameters were estimated using MAD and resistivity data collected at Sites C0012 and C0018 during IODP Expedition 333 (Expedition 333 Scientists, 2012b, 2012c). Assuming that the pore fluid is seawater, its resistivity (R_f) (Ωm) can be calculated as a function of temperature (T) ($^{\circ}\text{C}$) following Shipley, Ogawa, Blum, et al. (1995):

$$R_f = 1/(2.8 + 0.1T). \quad (2)$$

Temperature profiles were calculated for each hole based on thermal conductivity and temperature measurements made during previous expeditions or during this expedition. Archie's law implicitly assumes that the rock matrix has negligible electric conductivity compared to the pore fluid. It should be noted that matrix conductivities of only 5% of the pore fluid conductivity may cause significant errors in resistivity-derived porosity estimates (Glover et al., 2000).

Bulk density was calculated from the resistivity-derived porosity using the relationship between density and porosity, where a value of $\rho_f = 1.024 \text{ g/cm}^3$ was used for the pore fluid density:

$$\rho_b = \rho_g(1 - \phi) + \rho_f\phi. \quad (3)$$

Average grain density (ρ_g) values from MAD data collected from cuttings in Hole C0002F and cores in Hole C0022B and from MAD data collected during

IODP Expeditions 322 and 333 at Sites C0012 and C0018 (Expedition 322 Scientists, 2010c; Expedition 333 Scientists, 2012b, 2012c) were used.

Lithology

At Sites C0002, C0021, and C0022, cuttings description (Hole C0002F), visual core description (Holes C0002H, C0002J, C0002K, C0002L, C0021B, and C0022B), and LWD data (Holes C0002F, C0018, C0021A, and C0022A), including gamma ray, resistivity, and sonic data, were available to identify lithologic boundaries and units. Methods applied to core description during Expedition 338 draw upon the protocols of IODP Expedition 315 (Expedition 315 Scientists, 2009a), whereas methods applied to cuttings description rely heavily upon procedures established during IODP Expedition 319 (Expedition 319 Scientists, 2010b), in particular the Cuttings Cookbook.

Cuttings samples in Hole C0002F were described based on the examination of 70 cm^3 aliquots of bulk cuttings. Descriptions included the following:

- Macroscopic observations of percent silty claystone versus percent sandstone,
- Microscopic observations (including smear slides and quartz index measurements [see "[Q-index](#)"] from sieved sand fractions), and
- Bulk mineralogical data by XRD and bulk elemental data by XRF.

Core samples in Holes C0002H, C0002J, C0002K, C0002L, C00021B, and C00022B were described based on the following:

- Macroscopic observations following standard IODP visual core description protocols and observation of X-ray CT images,
- Microscopic observations (including smear slides and thin sections), and
- Bulk mineralogical data by XRD, bulk elemental data by XRF, and semiquantitative elemental data by XRF core scanning (Sakamoto et al., 2006).

Depths reported for cores and discrete samples are core depth below seafloor, Method A (CSF-A).

Macroscopic observations of cuttings

Cuttings typically occur as small fragments of rocks, in general 0.25–8 mm in size, often produced as re-aggregates of various lithologies fragmented during drilling. Cuttings were taken for the first time in IODP operations during Expedition 319 (Saffer, McNeill, Byrne, Araki, Toczko, Eguchi, Takahashi, and the Expedition 319 Scientists, 2010). Sampling and analysis of cuttings follow the Cuttings Cookbook

developed during Expedition 319, with some additions and modifications. Cuttings were taken every 5 m from 875.5 to 2005.5 mbsf and separated by laboratory technicians into rock-chip fractions of different sizes (0.25–1 mm, 1–4 mm, and >4 mm). However, at shallow depths, solid fragments from the formation can be suspended in drilling mud and mixed with trace amounts of clay-bearing drilling additives (e.g., bentonite). Rigorous separation of drilling-related mud from formation cuttings is not always possible, especially in the case of very soft cuttings. This hampers quantification of the true clay content. The separation procedure of cuttings from drilling mud, and the division into different sizes, is explained in the Cuttings Cookbook.

Based on general visual observations of the cleaned bulk cuttings material, we estimated the relative amount of silty claystone and sandstone, induration state, shape, occurrence of wood, and amount of artificial contamination. All macroscopic observations were recorded on visual cuttings description forms and summarized in CDS_MACRO_SED.PDF in CUTTINGS in VCD_SCAN in [“Supplementary material.”](#)

Macroscopic observations of core

We followed conventional Ocean Drilling Program (ODP) and IODP procedures for recording sedimentological information on Visual Core Description (VCD) forms on a section-by-section basis (Mazzullo and Graham, 1988). Core descriptions were transferred to section-scale templates using the J-CORES database and then converted to core-scale depictions using Strater (Golden Software). Texture (defined by the relative proportions of sand, silt, and clay) follows the classification of Shepard (1954). The classification scheme for siliciclastic lithologies follows Mazzullo et al. (1988).

To emphasize the differences in composition of volcanic sandstones in cuttings and core, we modified the classification scheme of Fisher and Schmincke (1984). In general, coarser-grained sedimentary rocks (63 μm –2 mm average grain size) are named “sandstone,” where volcanoclastic components are <25% of the total clasts. Volcanoclastic grains can be (1) reworked and commonly altered heterogeneous fragments of preexisting volcanic rock, tuff, or tephra or (2) fresh, or less altered, compositionally homogeneous pyroclasts. Pyroclasts are produced by many types of processes associated with volcanic eruptions without reference to the eruption causes or particle origin. Pyroclasts can include crystals, glass shards, and rock fragments. If the sedimentary rock contains >25% but <75% volcanoclasts, it is designated a “volcanoclastic sandstone.” As a subset of volcanoclastic

sandstone, if >25% but <75% of the volcanoclasts are vitric pyroclasts, then we used the term “tuffaceous sandstone.” If the total clast composition is >75% pyroclasts, then the sediment is classified as “ash” or, if lithified, as “tuff.” Depending on the grain size and degree of compaction, the nomenclature is adjusted accordingly (e.g., tuff versus ash), as shown in Table T6. Because of problems with accuracy, compositions close to the dividing lines of the classification scheme are problematic. In addition, with the exception of fresh glass shards in the population of pyroclasts, it is difficult to use smear slides to discriminate unequivocally between primary eruptive products and crystals or rock fragments created by the erosion of fresh volcanic material.

Where applicable in cores, bioturbation intensity in deposits was estimated using the semiquantitative ichnofabric index as described by Droser and Bottjer (1986, 1991). The indexes refer to the degree of biogenic disruption of primary fabric such as lamination and range from 1 for nonbioturbated sediment to 6 for total homogenization:

- 1 = no bioturbation recorded; all original sedimentary structures preserved.
- 2 = discrete, isolated trace fossils; <10% of original bedding disturbed.
- 3 = ~10%–40% of original bedding disturbed; burrows are generally isolated but locally overlap.
- 4 = last vestiges of bedding discernible, ~40%–60% disturbed; burrows overlap and are not always well defined.
- 5 = bedding is completely disturbed, but burrows are still discrete in places and the fabric is not mixed.
- 6 = bedding is nearly or totally homogenized.

The ichnofabric index in cores was identified with the help of visual comparative charts (Heard and Pickering, 2008). Distinct burrows that could be identified as particular ichnotaxa were also recorded.

The Graphic lithology column on each VCD plots all beds that are ≥ 2 cm thick to scale. Interlayers <2 cm thick are identified as laminae in the Sedimentary structures column. It is difficult to discriminate between the dominant lithologies of silty claystone and clayey siltstone without quantitative grain size analysis; therefore, we grouped this entire range of textures into the category “silty claystone” on all illustrations. A more detailed description of rock texture was attempted on the smear slide description sheets (see smear slides for each site in [“Core descriptions”](#)). We did not use separate patterns for more heavily indurated examples of the same lithologies (e.g., silty clay versus silty claystone) because the dividing line is arbitrary. Figure F7 shows the graphic patterns for all lithologies encountered dur-

ing Expedition 338. Also shown are symbols for sedimentary structures, soft-sediment deformation structures, severity of core disturbance, and features observed in X-ray CT images in both soft sediment and indurated sedimentary rock.

X-ray computed tomography

X-ray CT imaging provided real-time information for core logging and sampling strategies. A similar methodology to that used during IODP Expedition 316 was followed (Expedition 316 Scientists, 2009a). All core samples during this expedition were routinely scanned with the X-ray CT. X-ray CT scanning was performed immediately after core cutting so that time-sensitive whole-round samples (e.g., those for interstitial water) could be included in this screening process.

The scans were used to provide an assessment of core recovery, determine the appropriateness of whole-round and interstitial water sampling (avoid destructive testing on core samples with critical structural features), identify the location of subtle features that warrant detailed study and special handling during visual core description and sampling, and determine the 3-D geometry, crosscutting and other spatial relations, and orientation of primary and secondary features. See “[X-ray computed tomography](#)” for details about the X-ray CT methods.

Microscopic observation of cuttings

Microscopic investigations of the washed >63 μm sand-size fraction of cuttings samples using a binocular microscope allowed us to distinguish different minerals in the sediments; their abundance, roundness, and sorting; and the relative abundances of wood/lignite fragments and fossils. These data are summarized in “[Lithology](#)” and Figure F20, both in the “Site C0002” chapter (Strasser et al., 2014b), and in CDS_MICRO_SED.PDF in CUTTINGS in VCD_SCAN in “[Supplementary material](#).” Errors can be large, especially for fine silt and clay-size fractions. Thus, it would be misleading to report values as exact percentages. Instead, the visual estimates are grouped into the following categories:

- D = dominant (>50%).
- A = abundant (>10%–50%).
- C = common (>1%–10%).
- F = few (0.1%–1%).
- R = rare (<0.1%).

Q-index

An additional means of characterizing the sediment is the introduction of a new parameter called the “quartz index” (Q-index). Although the overall sand-

iness is measured by the percent of silty claystone versus percent of sandstone, the Q-index is a measure of the bulk sand fraction or caliber (i.e., the bulk mean grain size of the sand fraction). For example, it is possible to have a thick stratigraphic section of fine-grained sandstone (high percent of sandstone but a relatively low Q-index) or a relatively thin section of coarse-grained sandstone (low percent of sandstone and relatively high Q-index). Thus, it is important to appreciate that these parameters do not necessarily measure the same lithologic attributes. When comparing the Q-index with the percent of silty claystone versus percent of sandstone, it is apparent that there is a reasonable correspondence (see Figs. F18, F22, both in the “Site C0002” chapter [Strasser et al., 2014b]). For example, lithologic Units III and V at Site C0002 both have higher silty claystone versus sandstone content and a lower Q-index, and lithologic Unit IV has higher sandstone versus silty claystone content and a higher Q-index.

To obtain the Q-index, the sieved and washed >63 μm fraction representing a 5 m cuttings interval was inspected under the binocular microscope. The largest quartz grain in the field of view was selected (ignoring any exceptionally outsized grains) and photographed. The long axis of the grain was measured with the line measuring tool on the Digital Sight microscope camera. In cases of many large grains of similar size, several were measured and the largest one was chosen to represent the Q-index. The exclusion of the larger “rogue grains” does not affect the trends or relative grain sizes in this case because such solitary outsize grains always occur in sand fractions with the largest grain-size populations.

Smear slides

Smear slides are useful for identifying and reporting basic sediment attributes (texture and composition) in both cuttings and cores samples, but the results are semiquantitative at best (Marsaglia et al., 2013). We estimated the abundance of biogenic, volcanoclastic, and siliciclastic constituents using a visual comparison chart (Rothwell, 1989). Cuttings pieces were chosen for smear slide production based on the dominant lithology present in a given interval. If a distinct minor lithology was abundant, an additional smear slide was made for that interval. For cuttings, we estimated the percentage of minerals observed, normalized them to 100%, and reported the results in “[Core descriptions](#).”

For cores, estimates of sand, silt, and clay percentages are entered into the J-CORES database using the Samples application along with abundance intervals for the observed grain types, as given above. Additional observations, including visual estimates for

normalized percentages of grain size and mineral abundance, are recorded on the written smear slide forms, which are scanned and provided as supplementary data (see CORES in SCANS in SS_TS in “[Supplementary material](#).”). The sample location for each smear slide was entered into the J-CORES database with a sample code of SS using the Samples application.

The relative abundance of major mineralogy was also validated by XRD (see “[X-ray diffraction](#)”), and the absolute weight percent of carbonate was verified by coulometric analysis (see “[Geochemistry](#)”).

Smear slides were observed in transmitted light using an Axioskop 40A polarizing microscope (Carl Zeiss) equipped with a Nikon DS-Fi1 digital camera.

Thin sections

Thin sections were prepared for microscopic studies of mineralogy, petrology, paleontology, internal structures, and fabrics of rocks and sediments. A thin section was prepared as a 30 μm (0.03 mm) thick slice of core or cuttings sample. The standard size of billets for thin section preparation was 2 cm \times 3 cm \times 0.8 cm.

Soft sediments, cuttings, and rocks that were altered, badly weathered, or contained high clay content were dried first in the freeze dryer and then impregnated under vacuum (Epovac) with epoxy (Epofix) prior to mounting. Core or cuttings samples were attached to a glass slide with Petropoxy 154. Before microscopic observation, thin sections were covered by a cover glass using index oil. Thin sections were observed in transmitted light using an Axioskop 40A polarizing microscope (Carl Zeiss) equipped with a Nikon DS-Fi1 digital camera.

X-ray diffraction

The principal goal of XRD analysis of cuttings and cores was to estimate the relative weight percentages of total clay minerals, quartz, feldspar, and calcite from peak areas. For cuttings, XRD analysis was conducted on 10 g samples of the 1–4 mm size fraction every 5 m. This same 10 g sample provided aliquots for analysis of bulk carbonate and XRF elemental chemistry. Some measurements were also made on the >4 mm size fraction for comparison (Samples 338-C0002F-20-SMW through 289-SMW). For cores, material for XRD analysis was obtained from a 10 cm^3 sample that was also used for XRF and carbonate analyses. All samples were vacuum-dried, crushed with a ball mill, and mounted as randomly oriented bulk powders. Routine XRD analyses of bulk powders were performed using a PANalytical CubiX PRO

(PW3800) diffractometer. XRD instrument settings were as follows:

Generator = 45 kV.

Current = 40 mA.

Tube anode = Cu.

Wavelengths = 1.54060 \AA ($K_{\alpha 1}$) and 1.54443 \AA ($K_{\alpha 2}$).

Step spacing = $0.005^\circ 2\theta$.

Scan step time = 0.648 s.

Divergent slit = automatic.

Irradiated length = 10 mm.

Scanning range = 2° – $60^\circ 2\theta$.

Spinning = yes.

In order to maintain consistency with previous NanTroSEIZE results, we used the software MacDiff 4.2.5 for data processing (www.ccp14.ac.uk/ccp/ccp14/ftp-mirror/krumm/Software/macintosh/macdiff/MacDiff.html). We adjusted each peak's upper and lower limits following the guidelines shown in Table T7. Calculations of relative mineral abundance utilized a matrix of normalization factors derived from integrated peak areas and singular value decomposition (SVD). As described by Fisher and Underwood (1995), calibration of SVD factors depends on the analysis of known weight percent mixtures of mineral standards that are appropriate matches for natural sediments. SVD normalization factors were recalculated during Expeditions 315 and 338 after the diffractometer's high-voltage power supply and X-ray tube were replaced (Ashi et al., 2008). The mixtures were rerun at the beginning of Expedition 338 (Table T8). Bulk powder mixtures for the Nankai Trough are the same as those reported by Underwood et al. (2003): quartz (Saint Peter sandstone), feldspar (plagioclase), calcite (Cyprus chalk), smectite (Ca-montmorillonite), illite (Clay Mineral Society IMt-2, 2M1 polytype), and chlorite (Clay Mineral Society CCa-2). Examples of diffractograms for standard mixtures are shown in Figure F8.

Average errors (SVD-derived estimates versus true weight percent) of the standard mineral mixtures are as follows: total clay minerals = 3.3%, quartz = 2.1%, feldspar = 1.4%, and calcite = 1.9%. Despite its precision with standard mixtures, the SVD method is only semiquantitative, and results for natural specimens should be interpreted with caution. One of the fundamental problems with any bulk powder XRD method is the difference in peak response between poorly crystalline minerals at low diffraction angles (e.g., clay minerals) and highly crystalline minerals at higher diffraction angles (e.g., quartz and feldspar). Clay mineral content is best characterized by measuring the peak area, whereas peak intensity may more accurately quantify quartz, feldspar, and calcite. Analyzing oriented aggregates enhances basal

reflections of the clay minerals, but this is time consuming and requires isolation of the clay-size fraction (<2 μm) to be effective. For clay mineral assemblages in bulk powders, the two options are to individually measure one peak for each mineral and add the estimates together (thereby propagating the error) or to measure a single composite peak at $19.4^\circ\text{--}20.4^\circ 2\theta$. Other sources of error are contamination of mineral standards by impurities such as quartz (e.g., the illite standard contains ~20% quartz) and differences in crystallinity between standards and natural clay minerals. For trace quantities of a mineral and peaks with low intensity, use of negative SVD normalization factors may result in negative values of absolute weight percent. In such cases, we inserted the numerical value of 0.1% as a proxy for “trace.”

In the final assessment, calculated mineral abundances should be regarded as relative percentages within a four-component system of clay minerals + quartz + feldspar + calcite. How close those estimates are to their absolute percentages within the total solids depends on the abundance of amorphous solids (e.g., biogenic opal and volcanic glass), as well as the total of all other minerals that occur in minor or trace quantities. For most natural samples, the difference between calculated and absolute abundance percentage is probably between 5% and 10%. To compound the error, the XRD data from cuttings show effects of contamination by drilling fluid. The severity of these artifacts is especially obvious in the calculated values of percent calcite. Figures [F28](#) and [F29](#) and Table [T9](#) are all available in the “Site C0002” chapter (Strasser et al., 2014b).

X-ray fluorescence

XRF analyses were obtained in two modes: analysis of whole-rock powder and scanning of the whole-round core surface on some selected intervals.

Whole-rock quantitative XRF spectrometry analysis was performed for major elements on cuttings and cores. For cuttings, the 1–4 mm size fraction (and in some cases the >4 mm size fraction) was used for these measurements as well as for XRD and carbonate analyses. For cores, material for XRF was obtained from a 10 cm^3 sample that was also used for XRD and bulk carbon-nitrogen-sulfur (CNS) analyses.

For both cuttings and cores, all samples were vacuum-dried, crushed with a ball mill, and mounted as randomly oriented bulk powders. Major elements were measured using the fused glass bead method and are presented as weight percent oxide proportions (Na_2O , MgO , Al_2O_3 , SiO_2 , P_2O_5 , K_2O , CaO , TiO_2 ,

MnO , and Fe_2O_3). An aliquot of 0.9 g of ignited sample powder was fused with 4.5 g of SmeltA12 flux for 7 min at 1150°C to create glass beads. Loss on ignition was measured using weight changes on heating at 1000°C for 3 h. Analyses were performed on the wavelength dispersive XRF spectrometer Supermini (Rigaku) equipped with a 200 W Pd anode X-ray tube at 50 kV and 4 mA. Analytical details and measuring conditions for each component are given in Table [T9](#). Rock standards of the National Institute of Advanced Industrial Science and Technology (Geological Survey of Japan) were used as the reference materials for quantitative analysis. Table [T10](#) lists the results for selected standard samples. A calibration curve was created with matrix corrections provided by the operating software, using the average content of each component. Processed data were uploaded into an Excel spreadsheet and are shown in Figure [F30](#) and Table [T10](#), both in the “Site C0002” chapter (Strasser et al., 2014b).

XRF core scanning analysis was performed using the JEOL TATSCAN-F2 energy dispersive spectrometry-based core scanner (Sakamoto et al., 2006). The Rh X-ray source was operated at 30 kV accelerating voltage and a current of 0.170 mA. Data are reported as total counts on the peak and also as semiquantitative oxide weight percent. Semiquantitative analysis was performed using a 200 s accumulation. The following oxides were measured: Na_2O , MgO , Al_2O_3 , SiO_2 , P_2O_5 , K_2O , CaO , TiO_2 , MnO , and Fe_2O_3 . This is the same methodology as the one used during Expedition 316 (Expedition 316 Scientists, 2009a). The archive half was scanned because this technique is nondestructive to the sediment. Section 338-C0002J-5R-8 was scanned at a spatial resolution of 0.5 cm, and the scanning line was located along the center axis of the core section.

Identification of lithologic units

In Hole C0002F, we used LWD data (see details in “[Logging while drilling](#)”) in conjunction with analyses of cuttings to identify lithologic units and boundaries. We identified compositional and textural attributes of the formation mainly using NGR data, resistivity and sonic logs, and resistivity images (see “[Logging while drilling](#)” for details) along with data from cuttings. After evaluating log data quality through the examination of the potential effects of borehole diameter, borehole conditions, and drilling parameters, we defined units using changes in log responses interpreted to reflect differences in rock properties. For this analysis, NGR, sonic logs, and resistivity logs were the main input. Integrated interpretation of all the available logs focused on (1) definition and characterization of units and unit

boundaries, (2) identification of composition and physical properties within each unit, and (3) interpretation in terms of geological features (unit boundaries, transitions, sequences, and lithologic composition).

In Holes C0002H, C0002J, C0002K, C0002L, C0021B, and C0022B we interpreted lithologic units within the cores, as with cuttings, using a broad suite of data including logs, visual core descriptions, smear slides, thin sections, XRD, XRF, CNS analysis, and X-ray CT images.

Structural geology

During Expedition 338, two types of sample material were used for structural geology analyses: (1) cuttings (1–4 mm and >4 mm size fractions) sampled at 5–10 m intervals between 865.5 and 2004.5 mbsf during riser drilling of Hole C0002F and (2) cores recovered from 200.0 to 1112.84 mbsf in Holes C0002H, C0002J, C0002K, from 0 to 419.5 mbsf in Hole C0022B, and from 0 to 194.5 in Hole C0021B. Hole C0021B cores were not processed on board during Expedition 338 but were analyzed postexpedition during a shore-based sampling party at KCC. The methods we used to document the structural geology data of Expedition 338 cores and cuttings are largely based on those used by the Expedition 315 and 319 structural geologists (Expedition 315 Scientists, 2009a; Expedition 319 Scientists, 2010b). Depths reported for cores are in core depth below seafloor, Method A (CSF-A).

Description and data collection

Cuttings

Cuttings were investigated at 5 m depth intervals between 865.5 and 1065.5 mbsf. Below 1065.5 mbsf only every other sample (10 m interval) was routinely analyzed, but at distinct depths the frequency was increased to 5 m intervals (see CUTTINGS STRUCTURE.XLSX in STRUCTURE in [“Supplementary material”](#)). For the upper 510 m (865.5–1375.5 mbsf), structural descriptions were only carried out for the >4 mm size fraction. Between 1375.5 and 2004.5 mbsf, the 1–4 mm size fraction was also investigated.

After cuttings were sieved and vacuum-dried (see cuttings workflow, Fig. F5), they were studied with a binocular or digital microscope. Above 1415.5 mbsf, for the >4 mm size fraction, ~100 cuttings were randomly selected and investigated; below 1415.5 mbsf, we measured the volume of the observed cuttings and converted it to absolute numbers (conversion factor determined empirically: 12 cm³ = 100 cut-

tings). For the 1–4 mm size fraction, we always measured the volume of the analyzed cuttings and converted it to number of cuttings (conversion factor: 1.5 cm³ = 100 cuttings). The number of cuttings containing deformation structures is recorded in an Excel spreadsheet with descriptions of each structure (see [“Structural geology”](#) in the “Site C0002” chapter [Strasser et al., 2014b]). The percentage of cuttings with deformation structures per number of investigated cuttings is shown in CUTTINGS STRUCTURE.XLSX in STRUCTURE in [“Supplementary material”](#) and plotted in Figures F54 and F58, both in the “Site C0002” chapter (Strasser et al., 2014b). In addition to investigating deformation structures, we also estimated the ratio of sandstone to silty claystone in cuttings. These results were compared to the sandstone–silty claystone ratio derived by macroscopic lithologic observations on cuttings before they entered the cuttings workflow (see [“Lithology”](#)).

Deformation structures recognized in cuttings include vein structures, carbonate veins, slickenlined surfaces (or slickensides), and minor faults. Optical thin sections were made every 50–100 m in order to describe microstructures.

Cores

Structures preserved in cores were documented on split cores and on X-ray CT images of whole-round cores (see [“X-ray computed tomography”](#)). Observations on split cores were hand logged onto the structural geology observation sheet (Fig. F9) at the core table and then transferred to both a calculation sheet and the J-CORES database (see [“Data processing”](#)). Core observations and measurements followed procedures of previous ODP and IODP expeditions (e.g., ODP Legs 131, 170, and 190 and IODP Expeditions 315, 316, 319, 322, and 333).

We measured the orientations of all structures observed in cores using a modified plastic protractor (Fig. F10) and noted the measurements on the structural geology observation sheet along with descriptions and sketches of structures. The orientations of planar or linear features in cores were defined with respect to the core reference frame, where the core axis is directed vertically and the double line marked on the working half of the core liner is toward the north (0° or 360°) (Fig. F11). We followed the techniques developed during Leg 131 (Shipboard Scientific Party, 1991) and later refined during Expeditions 315, 316, 319, 322, and 333 (Expedition 315 Scientists, 2009a; Expedition 316 Scientists, 2009a; Expedition 319 Scientists, 2010b; Expedition 322 Scientists, 2010a; Expedition 333 Scientists, 2012a).

To determine the orientations of planes in the core reference frame, the apparent dip angle of any planar feature was measured in two independent sections parallel to the core axis (Fig. F12). The orientation was then calculated using a calculation sheet (see “Data processing”). In practice, one section is typically the split surface of the core, on which the trace of the plane has a bearing (α_1) and a plunge angle (β_1) in the core reference frame. α_1 is either 90° or 270° . The other section is, in most cases, a cut or fractured surface at a right or high angle to the split core surface, on which the bearing (α_2) and plunge angle (β_2) of the trace of the plane are measured. In the case where the second measurement surface is perpendicular to the core split surface, α_2 is either 0° or 180° . Both β_1 and β_2 are between 0° and 90° . Similar measurements were made for planar features visible in X-ray CT images.

Linear features (e.g., slickenlines) were commonly observed on planar structures (typically fault or shear zone surfaces). Their orientations were determined in the core reference frame by measuring either their bearing and plunge or their rakes (or pitches) (ϕ_a) on the planes (Fig. F13). When using rakes, in order to avoid confusion between two lines having the same rake but raking toward two opposite azimuths (e.g., a $N45^\circ\text{--}60^\circ\text{SE}$ fault bearing two striations, one raking 30°NE and the other raking 30°SW), we used the following convention, which applies for all planes except for subvertical planes: if the linear feature rakes from an azimuth between $N1^\circ\text{E}$ and $N179^\circ\text{E}$ or between $N181^\circ\text{E}$ and $N359^\circ\text{E}$, then “90” or “270” will follow the value of the rake. In the example depicted in Figure F13, “270” will be added after the ϕ_a value. In the case of subvertical planes, “+1” will follow the rake value to indicate rakes from the top of the core and “-1” to indicate rakes from the bottom of the core. The calculation sheet takes account of this information for data processing.

All the above-mentioned data as well as any necessary descriptive information were recorded on the structural geology observation sheet. We observed a variety of deformation structures in Expedition 338 cores (see “Structural geology” sections in the relevant site chapters). These included beddings, faults, shear zones, deformation bands, calcite-cemented breccias, fissility surfaces, scaly foliations, vein structures (Brothers et al., 1996; Cowan, 1982; Ogawa, 1980; Ohsumi and Ogawa, 2008), and so forth.

Data processing

Orientation data calculation and true north correction

An Excel spreadsheet developed during Expeditions 315, 316, 319, 322, and 333 was used to calculate orientation data in the core reference frame (Fig. F14; see STRUCTURES_NEW.XLSX in STRUCTURE in “Supplementary material”) (Expedition 315 Scientists, 2009a; Expedition 316 Scientists, 2009a; Expedition 319 Scientists, 2010b; Expedition 322 Scientists, 2010a; Expedition 333 Scientists, 2012a). Based on the measured bearings (α_1 and α_2) and plunge angles (β_1 and β_2), this spreadsheet determines the strikes and dip angles of planar features in the core reference frame. Because of drilling-induced core fragmentation (e.g., biscuiting) and ensuing core recovery and core preparation operations, the orientation of the core with respect to the present-day magnetic north is lost. A correction routine is therefore required to rotate orientations measured in the core reference frame back to the magnetic reference frame. Paleomagnetic data taken by the long-core cryogenic magnetometer on the *Chikyu* (see “Paleomagnetism”) were used to correct drilling-induced rotations of cored sediment whenever there was a paleomagnetic datum point within the same coherent interval. If paleomagnetic data are available, the Excel spreadsheet further converts the core reference data in geographic coordinates.

J-CORES structural database

The J-CORES database has a VCD program to store visual (macroscopic and/or microscopic) descriptions of core structures at a given section index and a record of planar structures in the core coordinate system. The orientations of such features are saved as commentary notes but do not appear on plots from the Composite Log Viewer. During Expedition 338, only the locations of structural features were entered in the J-CORES database, whereas orientation data management and analyses were performed with an Excel spreadsheet as described above. For final publication, structural elements were converted to core-scale depictions using Strater software (Golden Software, Inc.).

Biostratigraphy

Because there were no micropaleontologists on board during Expedition 338, micropaleontological

investigation occurred on shore after Expedition 338. Calcareous nannofossils and radiolarians in core and cuttings samples were collected from holes at Site C0002 and calcareous nannofossils and planktonic foraminifers in core samples were collected from Holes C0021B and C0022B.

Calcareous nannofossils

During Expedition 338, calcareous nannofossils were used to date the core catcher and cuttings samples. When necessary, we took additional samples from the cores to further refine ages.

Zonation and biohorizons

For Expedition 338, we applied a biostratigraphic zonation of calcareous nannofossils based on the zonal schemes of Martini (1971) and Okada and Bukry (1980). Our application of zonal markers and additional datums is mostly based on the compilation by Raffi et al. (2006) and Raffi (2002), in line with previous Expeditions 315, 316, 319, 322, and 333 for biostratigraphic consistency and subsequent correlation (see “Biostratigraphy” in Expedition 315 Scientists [2009a], Expedition 316 Scientists [2009a], Expedition 319 Scientists [2010b], Expedition 322 Scientists [2010a], and Expeditions 333 Scientists [2012a]).

Each nannofossil datum was assigned an astronomically calibrated age compiled by Raffi et al. (2006). The astrochronological frame for the Neogene follows the International Commission on Stratigraphy 2004 timescale (Lourens et al., 2004). The timescale and biostratigraphic zones of calcareous nannofossils are summarized in Figure F15 and Table T11.

Downhole contamination is common in riser drilling cuttings and often poses problems in recognition of a zonal boundary defined by a first occurrence (FO) datum because such a boundary may appear significantly stratigraphically lower than in situ. To circumvent this problem, a last occurrence (LO) datum stratigraphically close to a FO datum, if available, was selected to approximate the zonal boundary; otherwise, the biozone was combined with adjacent zones.

We applied two additional criteria to resolve the reworking of zonal markers, which tends to make the assemblage appear older. First, a datum was defined by the continuous occurrence of a taxon, whereas sparse occurrence was considered reworked. In addition, we used changes in assemblage composition and specimen size to evaluate the occurrence of zonal markers.

Taxonomic remarks

Taxonomy followed the compilation of Perch-Nielsen (1985) and Young (1998). Previous work suggested grouping reticulofenestrid species including genera *Gephyrocapsa* and *Reticulofenestra* by size. This is because their species show a great variation in size and other morphological features (e.g., relative size of the central opening and orientation of the bar in case of *Gephyrocapsa*).

Accordingly, *Gephyrocapsa* is divided into three major groups by maximum coccolith length following biometric subdivision by Rio (1982), Raffi et al. (1993) and Raffi (2002): small *Gephyrocapsa* (<4 μm), medium *Gephyrocapsa* (4–5.5 μm), and large *Gephyrocapsa* spp. (>5.5 μm). Some important morphologic features (e.g., bar orientation) were also considered during the analysis. In addition, *Reticulofenestra pseudumbilicus* should have a coccolith length >7 μm . Other smaller *Reticulofenestra* specimens (<7 μm) are included in *Reticulofenestra* spp., although *Reticulofenestra asanoi*, a characteristic circular taxon >6 μm in diameter, is separated.

Methods

We prepared smear slides from cuttings sampled at 50 m spacing and core catcher samples within the cored interval, following the standard method with photo-curing adhesive as a mounting medium. A simple concentration technique was adopted from Expedition 316 (see “Biostratigraphy” in Expedition 316 Scientists [2009a]) for samples that contained coarse materials or few to rare nannofossils. This technique involves suspending and settling sediment in distilled water to remove sand and silt before making smear slides.

In addition, we used a “mixing” technique for cuttings samples to better represent the 50 m sampling interval. We soaked a few grams of clean shale chips or drilling mud sediment mixture (when no hard rock pieces were present) in water and stirred to disaggregate and suspend the sample materials. The sample material was ground with a mortar and pestle when needed. The suspension was allowed to settle for 60 s, and then we drew ~3 mL of the suspension using a transfer pipet for making standard smear slides.

We examined slides using an Olympus BX 50 microscope under cross-polarized light and transmitted light at 1500 \times magnification.

We estimated relative abundances of nannofossil assemblages based on observations in a traverse at 1500 \times magnification, although usually more than

two transverses (more than ~300 fields of view [FOVs]) were browsed for zonal markers and rare species. A letter code was given to each abundance category and defined as follows:

- V = very abundant (>10 specimens per FOV).
- A = abundant (1–10 specimens per FOV).
- C = common (1 specimen per 2–10 FOVs).
- F = few (1 specimen per 11–100 FOVs).
- R = rare (1 specimen per 101–300 FOVs).
- B = barren (no nannofossils per >300 FOVs; for assemblage abundance only).

We only focus on the presence of nannofossil species in each sample and relative abundance of individual species/genus are not examined. The average preservation state of the nannofossil assemblage in each sample was qualitatively categorized and defined as follows:

- VG = very good (no evidence of dissolution and/or overgrowth; no alteration of diagnostic characteristics; all specimens identifiable at the species level).
- G = good (little or no evidence of dissolution and/or overgrowth; only slight alteration of diagnostic characteristics; most specimens [~95%] identifiable at the species level).
- M = moderate (evident etching and/or overgrowth; diagnostic characteristics sometimes altered; broken specimens frequent and delicate forms decreased; however, the majority of specimens identifiable at the species level).
- P = poor (severe dissolution, fragmentation and/or overgrowth; diagnostic characteristics largely destroyed; many specimens [>50%] not identifiable at the species and/or generic level).

Radiolarians

Radiolarian zones are given in the Neogene North Pacific zonation of Kamikuri et al. (2004, 2007) and in the Cenozoic low-latitude zonation of Sanfilippo and Nigrini (1998) wherever possible. They also provide numerical ages of bioevents, which are tuned to the geomagnetic polarity timescale (GPTS) of Cande and Kent (1995).

Methods

Sample preparation for microscopic examination followed the standard techniques described by Sanfilippo et al. (1985). Samples were treated with hydrogen peroxide (20% H₂O₂) and sodium pyrophosphate (5% Na₄P₂O₇) and heated to boiling. Hydrochloric acid (HCl) may be added to dissolve

calcareous components. Disaggregated particles were wet-sieved through a 63 µm mesh. Remaining residues were removed and dried. Undisaggregated sediment was treated again. The clean particles were spread on glass slides and mounted with Entellan-New. Slides were examined with a transmitted light microscope at 100× to 400× magnification. The first 200 specimens encountered in one slide were counted, after which slides were scanned to determine whether other taxa were present.

Total radiolarian abundance in a slide was based on the following categories:

- A = abundant (>500 specimens in a slide).
- C = common (100–500 specimens in a slide).
- R = rare (10–99 specimens in a slide).
- VR = very rare (1–9 specimens in a slide).

Preservation of the radiolarian assemblage was based on the following categories:

- G = good (radiolarians show no sign of dissolution with only minor fragmentation).
- M = moderate (radiolarians show evidence of moderate dissolution with obvious fragmentation).
- P = poor (radiolarians show signs of a high degree of dissolution with very few intact specimens).

Planktonic foraminifers

The planktonic foraminifer zonation of Blow (1969) and astronomically calibrated biohorizons of Neogene planktonic foraminifers compiled by Wade et al. (2011) were applied for this expedition. In addition, useful biohorizons were employed from literature in the field and converted in age to the current GPTS (ATNTS2012; Hilgen et al., 2012).

The LO of pink-colored *Globigerinoides ruber* was located at 0.12 Ma in the Indian and Pacific Oceans by Thompson et al. (1979) and confirmed by others (i.e., Li et al. [2005] at ODP Site 1143 in the South China Sea). The LOs of *Neogloboquadrina asanoi* and *Globoquadrina dehiscens* and the FO of *Globoconella inflata* modern form were correlated with geomagnetic polarities at ODP Sites 1150 and 1151 off northeast Japan (Motoyama et al., 2004). The coiling direction change of *Pulleniatina* spp. from sinistral to dextral has been reported just above Chron C2n (Olduvai) in the Boso Peninsula of central Honshu, Japan (Oda, 1977). The first consistent occurrence of *Neogloboquadrina acostaensis* was compiled by Berggren et al. (1995) and converted in age to the current GPTS. These biozones and biohorizons are shown in Table T12 and Figure F15.

Methods

About 10 cm³ of sediment from core catcher sections was collected for foraminifer analyses. Soft sediment samples were disaggregated using hydrogen peroxide solution and naphtha. Indurated mudstone samples were treated by the sodium tetraphenylborate method (Hanken, 1979). After samples were macerated, each sample was wet-sieved through a screen (63 µm opening). Planktonic foraminiferal specimens >125 µm were observed using a binocular microscope from the dried residues. A total of 100–5000 specimens were observed in each sample.

The relative abundance of planktonic foraminifers in each sample is based on the following categories:

- VA = very abundant (foraminiferal tests are exclusively dominant of sand-size residues).
- A = abundant (foraminiferal tests occupy 10%–50% of sand-size residues).
- C = common (>1000 specimens are observed in the sample).
- R = rare (100–1000 specimens are observed in the sample).
- VR = very rare (<100 specimens in the sample).

Preservation of each sample was recorded by the following criteria:

- P = poor (dissolution of surface structure and fragmentation are observed; most individuals cannot be identified at the species level).
- M = moderate (dissolution and fragmentation are commonly evident; some individuals are hard to identify).
- G = good (no dissolution; fragmentation of individuals has slightly occurred).

Geochemistry

Interstitial water geochemistry for core samples

Squeezing method

When core recovery and quality allowed, 15–50 cm long whole-round core (WRC) samples were taken from the cored sections. Squeezed interstitial water (IW) was sampled from Holes C0002J, C0002K, C0002L, C0021B, and C0022B. IW was not obtained from Hole C0002H because of low core recovery. Because the chemical composition of IW changes rapidly, WRC samples must be cut from a homogeneous part of the core section soon after recovery on the core cutting deck. Samples are capped in the core cutting area and immediately scanned by X-ray CT to check for the presence of structurally and/or lithologically important features as well as for homogeneity. In the case of important features being identified

on X-ray CT images, the samples were preserved for further observation and another portion of the core was cut for IW analysis. Samples approved for IW analysis were placed into nitrogen-filled glove bags, removed from the core liner, and cleaned by scraping off sediment along the outer surface of the WRC that came in contact with seawater or drilling fluid or had experienced smearing or oxidation. When samples were hard, they were crushed into small fragments inside the glove bag. This procedure made IW extraction easier when compared with putting sample blocks directly into the squeezer. The portion of the cleaned WRC to be squeezed was placed in a Manheim-type titanium squeezer (Manheim, 1966).

Following the procedures of the Expedition 319 Scientists (2010b), the samples were presqueezed by a manually operated squeezer until a few drops of water came out. This allowed a maximum amount of IW to be collected. Then, a 25 mL acid-washed (12 N HCl) syringe was installed into the IW sample port of the squeezer, and the samples were subject to automatic squeezing, which comprised six different steps, each lasting for 5 or 10 min, where loads of (1) 15,000, (2) 17,000, (3) 20,000, (4) 21,500, (5) 23,000, and (6) 25,000 lb (pound-force) were applied until enough volume (commonly >80 mL) of IW was collected for analyses. Loads of 15,000 or 17,000 lb are commonly enough to obtain the amount of IW from sediment shallower than ~300 mbsf; however, samples from deeper than ~400 mbsf were loaded to 20,000–25,000 lb, not only because of low IW content but also because of sediment consolidation. High pressure was needed to collapse the network of grains and release the IW.

To avoid contamination by sediment, IW was passed through a paper filter fitted with 2–4 titanium 90 mesh screens at the base of the squeezer and a 0.45 µm disposable filter. The squeezed water was filtered again with a 0.45 µm disposable filter and stored in high-density polyethylene sample vials, previously prepared by immersion in 55°C 10% trace metal grade 12 N HCl for at least 24 h, rinsed with Millipore 18.2 MΩ·cm Type 1 ultrapure (i.e., Milli-Q) water, and dried in a class 100 laminar flow clean hood. An aliquot of the sample water was stored in a plastic bottle without further treatment for the analyses of pH, alkalinity, major anions, and nutrients (phosphate and ammonium ions). Another aliquot of the sample was stored in a plastic bottle acidified with HCl to be 0.4 vol% of 6 N HCl to stably dissolve cations and minor and trace metal ions.

GRIND method

In cases of small sample volumes of recovered sediment (Section 338-C0002J-2R-2) and of low concen-

tration of labile water from deep and lithified sediment (Section 338-C0002H-2R-2), the ground rock interstitial normative determination (GRIND) method was applied to extract IW. Additionally, in order to investigate the accuracy of the GRIND method, the GRIND method was applied to several samples together with the standard squeezing method (see Table T31 in the “Site C0002” chapter [Strasser et al., 2014b]) and improved to acquire reliable data (see “Appendix A” for details).

A 5–10 cm long sample was taken from every IW WRC sample and put inside a glove bag, in which the external surfaces were scraped clean. Afterward, the samples were fragmented down to <1 cm in size (Wheat et al., 1994; Expedition 315 Scientists, 2009a). About 40 or 80 g of the sample (depending on the availability of sample weight) was carefully weighed, placed inside an agate ball-mill cylinder together with five agate balls, and 5 or 10 g (for 40 or 80 g samples, respectively) of Milli-Q water or dilute HNO₃ solution with pH adjusted to 3 was added after accurate weighing. Diluted HNO₃ solution of pH 3 was used because certain compositions gave more consistent values with those of squeezed water rather than using Milli-Q water. In order to remove dissolved oxygen, the Milli-Q water was bubbled with nitrogen gas for >48 h before being added to the sample. In the original procedure, Milli-Q water was spiked with indium (In) as a standard (concentration of 500 ppb), although it was not added here because the recovery of In was very low and it did not work as a spike for calculating the dilution rate. The water content was determined based on the weight difference before and after drying the sample sediment at 105°C overnight. The concentration of dissolved components of IW was calculated by the dilution rate of (IW content + added solution)/(IW content). This calculation was performed using the weight of IW in the used sample and added solution; thus, the weight of that with added solution was measured before processing.

Grinding the mixture of fragmented sample and HNO₃ solution in the ball mill took place for 5 min at 400 rpm, long enough to adequately crush and homogenize the contents and at the same time minimize the risk of reactions between the sample and the solution. Afterward, the ground slurry was squeezed and the extracted water was collected in a syringe, in a similar manner as the squeezing method. Analytical results of the IW obtained by the GRIND method were evaluated based on the comparable methods (see “Appendix A”).

Interstitial water analyses

The standard IODP procedure for IW analysis was modified according to the availability and functionality of onboard instruments (Expedition 319 Scientists, 2010b). However, because of the limited amount of extracted pore water, not all of the standard IODP measurements were conducted.

Concentrations of numerous major and minor components in the IW were analyzed. Chlorinity was measured on a 100 µL aliquot by potentiometric titration using a Metrohm autotitrator and silver nitrate (AgNO₃) as a titrant in 30 mL of 0.2 M sodium nitrate (NaNO₃) solution. Relative standard deviation (RSD) for chlorinity was better than ±0.2%, based on repeated analyses of International Association for the Physical Sciences of the Oceans (IAPSO) standard seawater, which were conducted between the measurement of every 5 samples.

Bromide and sulfate concentrations were measured with a Dionex ICS-1500 ion chromatograph with an anion column. An aliquot was diluted to 1:100 (10 µL in 990 µL) with Milli-Q water. IAPSO standard seawater aliquots (2.5, 5, 7.5, and 10 µL in a total of 1000 µL) were analyzed at the beginning and end of each run for quality control and to monitor potential drift in sensitivity throughout a particular run. RSDs are ±3% for bromide and ±1% for sulfate.

An ion chromatograph was used to determine the concentrations of major cations such as Na⁺, K⁺, Mg²⁺, and Ca²⁺. Aliquots of IW samples acidified with 6 M HCl (Tamapure-AA-100 grade) were used for this measurement. These samples were diluted to 1:200. The diluted samples were placed in an auto-sampler together with five calibration solutions and two blank solutions (Milli-Q water). For quality checks, a 1:200 solution of diluted IAPSO standard seawater was measured between every eight samples. To determine the concentration of each element, standard solutions were analyzed to construct calibration curves from the measured peak area and the known concentration. For the calibration, an IAPSO standard seawater solution containing Na⁺ (480 mM), K⁺ (10.4 mM), Mg²⁺ (54 mM), and Ca²⁺ (10.6 mM) was diluted to four standard solutions (25%, 50%, 75%, and 100%). The resulting RSD for the measurements was less than ±0.5% for Na⁺, ±1% for K⁺, ±0.7% for Mg²⁺, and ±0.5% for Ca²⁺.

For nutrients (PO₄³⁻ and NH₄⁺), colorimetric methods were applied. Both compositions must be analyzed within 24 h because they are quickly degraded by biological activity. Ammonium adsorption of indophe-

nol blue at 640 nm wavelength was measured with a spectrophotometer (Shimadzu UV-2550PC), with an aliquot of 100 μL of sample IW used as the minimum volume. Standard, blank, 2, 4, 6, 8, and 10 mM NH_4^+ solutions were prepared in the same manner as the sample solutions and analyzed within 5 h. Phosphate (an aliquot of 100 μm IW) was analyzed using adsorption of molybdate blue at 885 nm wavelength with the spectrophotometer used for NH_4^+ . Standard, blank, 0.5, 1, 2.5, 5, and 7.5 mg/L solutions were prepared in the same manner as that of sample solutions. RSDs of repeated analyses of both components are <1%.

Minor element (B, Ba, Fe, Li, Mn, Si, and Sr) concentrations were determined on 500 μL aliquots using an inductively coupled plasma-atomic emission spectroscopy (ICP-AES) (Horiba Jobin Yvon Ultima2). Aliquots of IW acidified with 6 M HCl (Tampure-AA-100 grade) were diluted to 1:20 with 0.15 M HNO_3 . Ultrapure primary standards (SPC Science PlasmaCAL) were prepared with a matrix solution of sulfate-free artificial seawater to fit the sample matrix, and 10 ppm Y solution was added as an internal standard. A matrix solution that approximated IAPSO standard seawater major element concentrations was prepared by mixing the following salts in 1 L of Milli-Q water acidified with 4 μL of Tampure-AA-100 grade 6 M HCl: 26.9 g NaCl, 3.81 g MgCl_2 , 1.0 g CaCO_3 , and 0.75 g KCl. A stock standard solution was prepared from ultrapure primary standards (SPC Science PlasmaCAL) in the 1% HNO_3 solution and then diluted in the same 1% ultrapure HNO_3 solution used for IW samples to concentrations of 100%, 50%, 25%, 10%, 5%, and 1%. A 10 ppm Y solution diluted as 1% HNO_3 solution was prepared as a blank. A series of standards were made by adding 1.25 mL of each stock solution to 8.75 mL of matrix solution.

The matrix-matched 100% standard solution contained the following concentrations of elements: B = 145 μM , Ba = 11.4 μM , Fe = 2.80 μM , Li = 22.5 μM , Mn = 2.84 μM , Si = 55.7 μM , and Sr = 17.8 μM . Because values of many of these elements in IAPSO standard seawater are either below detection limits (e.g., Fe and Mn) or variable, a standard prepared in the 10% matrix-matching solution was repeatedly analyzed to calculate the precision of the method. RSDs determined by repeated analyses of the 10% matrix-matching solution were $\pm 2.5\%$ for B, $\pm 1.5\%$ for Ba, $\pm 3.5\%$ for Fe, $\pm 4.1\%$ for Li, $\pm 2.5\%$ for Mn, $\pm 2.5\%$ for Si, and $\pm 2.0\%$ for Sr.

V, Cu, Zn, Rb, Mo, Cs, Pb, and U were quantified on 500 μL IW samples using an inductively coupled

plasma-mass spectrometry (ICP-MS) (Agilent 7500ce) equipped with an octupole reaction system to reduce isobaric interferences from polyatomic and double-charged ions. We used the same aliquot after determining major and minor elements using an ion chromatograph and ICP-AES. To correct for interferences between some of the transition metals (V, Cu, and Zn) and some major element oxides, solutions containing the metals with concentrations similar to IAPSO standard seawater values were prepared. These solutions were then analyzed at the beginning of each measurement, and an interference correction was applied based on the average ion counts per second measured on the standard solutions divided by the abundance of the interfering elements.

A 500 μL aliquot of sample IW was diluted with 500 μL with 500 ppb In internal standard solution and 4 mL of 1% HNO_3 based on the previous determination of detection limits and low concentrations of the elements of interest. A primary standard solution was made to draw the calibration lines matching the maximum range of predicted concentrations based on published results of deep-sea pore fluid compositions in a variety of settings. The concentrations of the standard are as follows: V = 40 ppb; Cu, Mo, Pb, and U = 40 ppb; Zn = 140 ppb; Rb = 540 ppb; and Cs = 40 ppb. This primary standard was diluted with 1% HNO_3 solution to relative concentrations of 100%, 50%, 25%, 10%, 5%, 1%, and blank. A 500 μL split of these standards was then further diluted by addition of the In solution, 3.5 mL of 1% HNO_3 solution, and 500 μL of a 560 mM NaCl solution to account for matrix suppression of the plasma ionization efficiency. The 200% and 400% standard solutions were also prepared using 100% solution changing dilution rate (i.e., instead of combination of 500 μL 100% standard, 500 μL In, and 4 mL HNO_3 solutions, 1000 μL and 2000 μL of 100% standard solution were diluted with 500 μL In solution and 3.5 and 3.0 mL HNO_3 solutions, respectively). The 25% standard was diluted accordingly and analyzed together with eight samples throughout every analysis series for precision and to check the drift during measurements. Blanks were also analyzed between every eight samples, and detection limits were determined to be three times the standard deviation of a procedural blank of Milli-Q water acidified with 4 mL of Tampure-AA-100 grade 0.15 M HNO_3 . The average precision of multiple determinations of the 25% ICP-MS standard was $\pm 3.0\%$ for ^{51}V , $\pm 3.0\%$ for ^{65}Cu , $\pm 7\%$ for ^{65}Zn , $\pm 1\%$ for ^{85}Rb , $\pm 2\%$ for ^{95}Mo , $\pm 0.5\%$ for ^{133}Cs , $\pm 4\%$ for ^{208}Pb , and $\pm 1\%$ for ^{238}U .

Organic geochemistry

Total carbon (TC), inorganic carbon (IC), and total nitrogen (TN) were analyzed using samples from cuttings and core samples. Total sulfur (TS) was measured using core samples. Cuttings (~10 cm³) were washed with seawater, sieved, freeze-dried, and ground to powder before analysis. Core samples (~10 cm³) were freeze-dried and ground to powder before analysis.

TC, TN, and TS concentrations were determined using a Thermo Finnigan Flash elemental analysis (EA) 1112 carbon-hydrogen-nitrogen-sulfur analyzer. Calibration was based on the synthetic standard sulfanilamide, which contains 41.81 wt% C, 16.27 wt% N, and 18.62 wt% S. About 15–25 mg of sediment powder was weighed and placed in a tin container for carbon and nitrogen analyses. For sulfur analysis, the same amount of sediment powder was weighed and put into a Ti container with an equivalent mass of V₂O₅ catalyst. Sediment samples were combusted in an oxygen stream at 900°C for carbon and nitrogen and at 1000°C for sulfur. Nitrogen oxides were reduced to N₂, and the mixture of CO₂, N₂, and SO₂ was separated using a gas chromatograph (GC) equipped with a thermal conductivity detector (TCD). The accuracy of the analysis was confirmed using soil NCS reference material (Thermo Scientific, Milan, Italy), sulfanilamide standard (Thermo Scientific), and JMS-1 reference material.

With the same set of samples used for elemental analysis, we determined IC using a Coulometrics 5012 CO₂ coulometer. Approximately 15–25 mg of sediment powder was weighed and reacted with 2 M HCl. The released CO₂ was titrated, and the change in light transmittance was measured with a photodetection cell. The weight percentage of calcium carbonate was calculated from the IC content, assuming that all the evolved CO₂ was derived from dissolution of calcium carbonate, by the following equation:

$$\text{CaCO}_3 \text{ (wt\%)} = \text{IC (wt\%)} \times 100/12. \quad (4)$$

No correction was made for the presence of other carbonate minerals. Standard deviation for the samples was less than ±0.05 wt%. NIST-SRM 88b and JSD-2 (standard reference materials) were used to check accuracy. TOC contents were calculated by subtracting IC from TC contents as determined by EA.

Assessing drilling mud contamination

Very high TOC concentrations in cuttings raised the potential of samples being contaminated by drilling

mud. To assess any potential contamination, eight mud water (LMW) and mud pit (LMT) samples from the mud circulation tanks were analyzed for carbonate, organic carbon, and nitrogen concentrations during Expedition 338. Approximately 5 mL of mud water sample was placed in a petri dish and dried at 60°C. Dried samples were ground by an agate mortar and analyzed for IC, TC, and TN concentrations following the same analytical protocol used for cuttings. Background concentration data are listed in Table T13.

Because of high viscosity, mud water and mud pit water samples were diluted 10 times with Milli-Q water and placed in an ultrasonic bath for 1 h so that the solutions were well mixed. Supernatant drilling mud water was centrifuged at 9500 rpm at 4°C for 1 h. Samples were filtered and analyzed for major, minor, and trace elemental concentrations following the standard procedure adopted for cuttings. The results are listed in Table T32 in the “Site C0002” chapter (Strasser et al., 2014b).

Gas analysis

Sampling and analyzing mud gas

Onboard mud-gas monitoring system

Continuous mud-gas monitoring (CMGM) is a standard procedure in the oil and gas industry and is usually carried out to obtain real-time, qualitative information regarding a gas and/or oil reservoir and to assess the need (or advantage) of deeper drilling. In the framework of IODP, CMGM was first carried out during Expedition 319 (Expedition 319 Scientists, 2010a) using third-party tools and was successfully applied during IODP Expedition 337 with onboard instruments (Expedition 337 Scientists, 2013). The onboard set-up follows previous experience with scientific real-time CMGM and sampling in the context of continental drilling (e.g., Erzinger et al., 2006; Wiersberg and Erzinger, 2007, 2011).

Gases released by the drill bit crushing the source rocks were transported upward within the drilling mud. After passing the flow splitter (Fig. F16), the gases were extracted using a degasser, in which a vacuum is applied and which hosts an impeller ensuring fluid circulation. Some of the mud flowed directly into the bypass line for the degasser. The gas was sucked into PVC tubing and transported to the mud-gas monitoring laboratory, passing through a safety valve placed between the degasser and the monitoring laboratory to prevent overflow of drilling mud into the system. The safety valve consists of a 1 m long cylinder with a central tube that opens at both ends. The lower 40 cm of the cylinder and the tubing are covered with water. If the gas pressure is too low

or too high, air can be sucked in or blown out, respectively, which causes water either to flow from the central tube to the cylinder or vice versa to compensate the pressure difference. During Expedition 337, problems arose from mud sucked into the tubing. As an early countermeasure, a mud catcher was inserted between the degasser and the safety valve.

Gas extracted from the drilling mud traveled through a 50 m long tube with an inner diameter of 3 mm, taking ~6 min for gas to arrive at the mud-gas monitoring laboratory (Fig. F16E) (lag time was determined based on the time difference between the start of mud flow and the arrival of mud gas in the monitoring laboratory when drilling resumed after periods in which mud flow had been stopped). For such a short gas traveltime, particularly through PVC tubing, diffusion loss during transportation is negligible (Wiersberg and Erzinger, 2007). In the mud-gas monitoring laboratory, particles and water vapor were removed from the incoming gas by a dehydration module, after which the dry and clean gas was distributed to different instruments. Sampling for postcruise analysis on shore was taken from two sampling ports either before or after passing the mist and moisture remover.

On-line analysis of (non)hydrocarbon gases by gas chromatography

A fraction of the drilling mud gas flowed directly into a GC-natural gas analyzer (NGA) (Agilent Wasson ECE 6890N) that theoretically allows the analysis of hydrocarbon gases (methane, ethane, propane, *iso*-/*n*-butane, and pentane [i.e., C₁–C₅]), Ar, He, O₂, N₂, Xe, CO, and CO₂. The main component of the GC-NGA system is a GC equipped with a gas sampling port with a multiposition valve. Contrary to the procedures used during Expedition 337, hydrogen rather than helium was supposed to be used as the carrier gas. However, hydrogen caused baseline and concentration problems for several elements, including Ar and O₂; therefore, nitrogen was used as the carrier gas.

Analysis of hydrocarbon gases was conducted by passing the gas flow into a 50 cm capillary column that is able to retain hexane and heavier hydrocarbon components. Lighter hydrocarbon gases are then separated by another 49 cm capillary column that connects to a flame ionization detector (FID), with which measurements were conducted every 20 min. CH₄ was separated from the rest of the components by an 8 inch micropack column (Wasson ECE Instrumentation, column Code 2378), whereas CO₂ was separated by a 1.27 cm capillary column (Wasson ECE Instrumentation, column Code S036). Both

columns are connected to a TCD with a detection limit of 200 ppm for all permanent gases besides CO, which had a detection limit of 400 ppm. For the remaining hydrocarbons, the detection limit was <1 ppm. Unfortunately, because of nitrogen being used as the carrier gas and the absence of proper calibration gases, only H₂ could be determined with the TCD for the nonhydrocarbons.

Although the GC-NGA has good sensitivity, the temporal and spatial resolution of the mud-gas analysis with a GC-NGA is limited because of the rather long run time of 20 min.

The GC-NGA was calibrated on a daily basis in order to detect any sensitivity changes. Two standards were used. The standard mixture for calibration of permanent gases contained 1% of Ar, CO, Xe, O₂, H₂, CO₂, and He in a balance of N₂. The hydrocarbon standard mixture contained 1% C₁–C₅ in a balance of N₂.

Hydrocarbon concentration is obtained by FID analysis. However, care has to be taken in data interpretation because measured concentrations are influenced by drilling conditions such as ROP and mud flow. Consequently, drilling operations were monitored to allow comparison and interpretation of quantitative data.

Fortunately, in situ conditions can still be investigated by the ratio of hydrocarbon gases, which is only slightly affected by drilling parameters. In particular, the Bernard parameter (C₁/[C₂ + C₃]) is a valuable tool to distinguish between hydrocarbon gases from biogenic and thermogenic sources and allows a first estimation regarding the thermal maturity (see Fig. F17) (Pimmel and Claypool, 2001; Ocean Drilling Program, 1992).

On-line analysis of the stable carbon isotopic composition of methane

Another part of the incoming mud gas was directed to a methane carbon isotope analyzer (MCIA) (Los Gatos Research, Model: 909-0008-0000). The concentration and stable carbon isotopic composition of methane is determined on the basis of cavity ring-down spectroscopy technology. The instrument is composed of three parts: the main body of the MCIA, a gas dilution system (DCS-200), and an external pump. The stable carbon isotopic composition of methane is reported in the δ¹³C notation relative to the Vienna Peedee belemnite (VPDB) standard and expressed in parts per thousand (per mil):

$$\delta^{13}\text{C} = (R_{\text{sample}} - R_{\text{VPDB}})/R_{\text{VPDB}}, \quad (5)$$

where

$$R_{\text{sample}} = {}^{13}\text{C}/{}^{12}\text{C}, \quad (6)$$

and

$$R_{\text{VPDB}} = 0.0112372 \pm 2.9 \times 10^{-6}. \quad (7)$$

For CH_4 , the precision and accuracy are within 1‰ for concentrations >400 ppm but worsen to <4‰ for concentrations of 200–400 ppm. The MCIA comprises a gas dilution system that works with hydrocarbon or zero-free air and allows measurement of methane concentrations in the range of 500–10⁶ ppm (i.e., 100%). However, the dilution system did not function because of technical problems, and the concentration data from the MCIA were not utilized when >1 × 10⁴ ppm and <2 × 10⁵ ppm.

Besides the determination of $\delta^{13}\text{C}$, the MCIA also allows the determination of whole methane concentration. A disadvantage of the MCIA compared to the GC-FID is its lower sensitivity. However, the sampling frequency is much higher (a frequency of 1 measurement/s was chosen here), enabling 100–200 measurements per meter of drilled sediment, depending on the ROP and mud flow. The sensitivity of this instrument was checked daily with a standard gas with 2500 ppm CH_4 and a $\delta^{13}\text{C}$ value of –38.8‰.

The determination of $\delta^{13}\text{C}$ combined with the Bernard parameter is a powerful tool to distinguish between biogenic and thermogenic sources of hydrocarbon gases during mud-gas monitoring (for details, see Whiticar, 1999) (Fig. F18). It allows further detection of mixed and oxidized gases. However, for further investigations, it will be necessary to do onshore $\delta^{13}\text{C}$ analysis of the higher homologues and δD of all hydrocarbons.

On-line gas analysis by process gas mass spectrometer

Incoming mud gas was also transferred to a process gas mass spectrometer (PGMS) (Ametek ProLine process mass spectrometer), which allowed continuous monitoring of H_2 , He, O_2 , Ar, Xe, N_2 , CO, CO_2 , methane, ethane, propane, and butane (differentiation between *n*- and *iso*-butane not possible). One advantage of the PGMS is the presence of vacuum not requiring a carrier gas, which might alter the individual gas concentration. The PGMS uses a quadrupole mass filter and identifies gases based on the individual molecular masses of the desired compounds. A Faraday cup detector provides an optimal scanning range of mass-to-charge ratio (m/z) 1–100 and an optional scanning range of m/z 1–200 with the mass resolution of 0.5 at 10% peak height. Input gas flow rate is set to 50 mL/min. For quantification of individual gas species, the PGMS was calibrated on a daily basis using the same standards as for the GC-

NGA. Although the PGMS is less sensitive (within 1 ppm) than the GC-NGA, full-range measurements (i.e., m/z 1–200) are possible every 20 s, resulting in better depth resolution. However, during Expedition 338, because of the limitations of the dedicated laptop PC, full-range measurement was not possible. Instead, the system was changed to the “trend mode,” where only selected masses were determined. The dwell time was changed to 120 ms, which decreased the sampling period to 5 s.

For regular quality assurance, three different calibrations had to be carried out:

1. Binary calibration. This calibration was necessary to establish peak ratios of ion fragments and was usually carried out using a mixture of two gases (a noninterfering balance gas like Ar mixed with a gas that was expected in the sample stream with an appropriate concentration). By contrast, here, only CH_4 with a concentration of 100% was used.
2. Blend calibration. This calibration was used to compensate for ionization variations. Two different standard gases were used: one containing 1% of Ar, CO, Xe, O_2 , H_2 , CO_2 , and He in a balance of N_2 , and the other containing 1% of C_1 – C_5 in a balance of N_2 . Pure N_2 and Ar were used for daily background checks. Unfortunately, the concentrations were far too high for the expected concentrations, which led to overestimation of some noble gases.
3. Background calibration. This calibration was used to determine the atmospheric values of gases in the vacuum chamber. For this purpose, Ar and N_2 calibration gases were used, each having a concentration of 100%.

Ar, N_2 , and O_2 concentrations can serve as proxies for air contamination during drilling operations or from the mud-gas monitoring system. Air can be introduced into the borehole when the pipe is broken to recover core, when mud flow is stopped while new pipe connections are made (every 38 m for one stand of four joints of drill pipe), when pressure drops in the gas separator, when mud gas is flowing from the bypass line into the flow splitter, or when leaks in the degasser or in the mist and moisture remover occur. Very high N_2 values might further indicate humid source rocks (Whiticar, 1994). Note that CO_2 can be analyzed by the GC-NGA, but the resulting concentrations are not meaningful because drilling mud is highly alkaline.

On-line radon analysis

Radon analysis was carried out using a stand-alone radon monitor (Alpha GUARD PQ2000 PRO) provided by the JAMSTEC Institute for Research on Earth Evolution (IFREE). The apparatus was attached to the

auxiliary port of the scientific gas monitoring line parallel to other instruments. Rn itself is radioactive with a half-life time of 3.8 days; thus, the Rn decay can be counted within an ion-counting chamber with a volume of 650 mL (effective volume is ~500 mL). Measurements took place every 10 min with 5 counts per minute (cpm) and a sensitivity of 100 Bq/m³ in the concentration range of 2 to 2 × 10⁶ Bq/m³. Synchronous with Rn measurements, internal temperature, pressure, and relative humidity are monitored and, together with Rn data, can be exported in CSV format.

Sampling for shore-based analysis

Unlike during Expedition 337 (Expedition 337 Scientists, 2013), discrete samples were not only collected in IsoTube samplers (Isotech Laboratories, Inc.) but also in copper tubes for noble gas studies and in glass flasks for stable isotope studies. A sample interval of 500, 200, and 50–100 m was chosen for samples stored in the IsoTubes, copper tubes, and glass flasks, respectively.

The configuration was from a sampling port at the main gas flow line, where PVC tubing was suspended and connected to the glass flasks. The glass flasks had valves at both ends to control the gas flow and allow passing of gas through the glass flask again into PVC tubing, which connected the glass flask and the copper tubes. The copper tubes were placed in a guide rail and allowed the passage of gas through the next section of PVC tubing, which ended in a sampling port connected to the main gas flow line (Fig. F16).

After a certain time, depending on the flow rate, sampling was done by closing the valves at both ends of the glass flasks and placing clamps at both ends of the copper tubes. Afterward, the glass flasks and copper tubes were replaced with empty ones. Additional samples were taken after pipe tripping (trip gas) or when mud-gas monitoring indicated enhanced inflow of formation fluid.

Recording on-line gas analysis and monitoring drilling operations, time, and depth

As mentioned above, the recovery and concentration of gases can be affected by drilling operations. Drilling parameters were monitored and recorded in the SSX database together with gas data and the lag depth determined by technicians from Geoservices (Schlumberger). The results of the on-line measurements were made available in the mud-gas monitoring laboratory and on the onboard server. To correlate the results of the gas analysis with variations in the drilling procedure as well as lag depth determination, ship time (UTC + 9 h) was used. As an excep-

tion, the stand-alone Rn monitor used an internal clock set to the time zone UTC + 1 h. Adjusting the internal clock of the MCIA to ship time failed; consequently, it was 90 s ahead during Expedition 338.

Regarding the lag depth (i.e., the difference between the depth of arriving mud gas and actual depth of the borehole), Lag Depth L (as recorded in real time in the SSX database and provided by Geoservices) was used to assign data and samples from mud-gas monitoring to the correct seafloor depth. Lag Depth L was calculated based on the ROP and borehole volume and was recorded in meters below rig floor (rotary table) (DRF). It further considered the transfer time between the degasser and the different laboratory instruments, which was 6 min to the MCIA and the IsoTube sampling unit and almost 9.5 min for the other instruments. Unfortunately, only one Lag Depth L could be recorded. Consequently, only the transfer time of 6 min was taken into account. Data obtained from the Rn instrument, GC-NGA, and PGMS were corrected after the data were exported and evaluated. Conversion to mbsf was done by subtracting water depth (1939 m) and distance between sea level and rotary table (28.5 m).

All data gathered during mud-gas monitoring by the GC-FID, MCIA, and PGMS were transferred together with the drilling parameters to the SSX database, where all data were synchronized. Unfortunately, the resolution of the PGMS data included in the SSX database was far too low for on-line monitoring purposes, and therefore, raw PGMS data were used. Data were recorded at all times, including periods where no drilling was conducted and/or mud-gas flow was absent. During data processing, time periods where Lag Depth L did not change were removed. In addition, for hydrocarbon gases, concentrations ≤0.0001% were not considered during data evaluation.

Background control, quality checks, and comparison of different sampling techniques

Following the Expedition 337 Scientists (Expedition 337 Scientists, 2013), several potential problems can arise in mud-gas monitoring, which made it necessary to conduct different tests during geochemical mud-gas monitoring.

Background control. In the drilling mud, formation gases usually mix with atmospheric gases already present in drilling mud as well as with remaining gases from previous gas extraction. Consequently, drilling mud was sampled from the tank regularly, and the hydrocarbon gas component was measured on board the ship. The mud samples were taken with 50 mL plastic vials, which were completely filled and sealed with a plastic cap. After the sample was trans-

ferred to the laboratory, a subsample was taken and placed into a 20 mL glass vial and immediately sealed with a silicon septum and metal crimp cap.

The headspace analysis was carried out using an Agilent Technologies G1888 Network Headspace Sampler, where the sample was heated at 70°C for 30 min before an aliquot of the headspace gas was automatically injected into the GC-FID. Unfortunately, background concentrations of nonhydrocarbon gases could not be determined with the available instrumentation. The results of the background checks are displayed in Figure F19. Although the variations in the data follow the ones found in the sampled gas (see “Geochemistry” in the “Site C0002” chapter [Strasser et al., 2014b]), the overall background concentrations of hydrocarbon gases were, with up to 1152.92 and 2.72 ppm for methane and ethane, respectively, too low to have a significant effect on the sample gas measurements in the upper part of the borehole. For the lower part of the borehole, however, an effect cannot be excluded because of the overall low gas concentration (see “Geochemistry” in the “Site C0002” chapter [Strasser et al., 2014b]). Although propane was absent during the background checks, concentrations of up to 17.00 ppm of *iso*-butane were found, which is relatively high and might have influenced the *iso*-butane concentrations in the sampled gas.

Dehydrator. The dust remover and dehydrator module (CFP-8000, Shimadzu Corp., Japan) is a possible source for air contamination and could cause fractionation, both with respect to gas contents and their isotopic composition (Expedition 337 Scientists, 2013). During Expedition 337, gas standards were measured with and without passing through the gas dehydrator, and consequently, no further analysis was applied here. According to the Expedition 337 Scientists (2013), for methane the effect of the dehydrator was within the analytical uncertainty. The methane content of the dried gas was 3% lower and the $\delta^{13}\text{C}$ values were 0.4% more positive when compared to the unfiltered gas. By contrast, for the PGMS, mist and moisture affected H_2 , O_2 , He, and CO_2 concentration calculations. H_2 and O_2 concentrations in the wet gas were both 2% higher than those in the dried gas, whereas He and CO_2 concentrations in the dried gas were 67% and 84% higher than in the wet gas.

Verifying results obtained from the MCIA. The MCIA for on-line mud-gas monitoring was used for the first time in the history of scientific ocean drilling during the Expedition 337. In order to confirm its accuracy, the Expedition 337 Scientists took samples of gas and will analyze them on shore by isotope ratio monitoring gas chromatography–mass spec-

trometry (Expedition 337 Scientists, 2013). Consequently, no further subsampling was done during Expedition 338.

Check for air contamination. A check for possible leaks and consequent air contamination was carried out (see “Appendix B” for details). For this purpose, the mud trap between the degasser and the safety valve was removed from the degasser. The standard hydrocarbon gas used for this experiment was the same as the one used for calibration of the PGMS and GC-NGA and was introduced in the mud trap and transferred to the field laboratory. The test showed that no leakage was present between the mud trap (first feature after the degasser) and the PGMS (last feature after the degasser). Consequently, the source of air contamination might be found in the configuration of the degasser itself, and thus, all samples that were taken during this expedition might be affected. When looking at the test results more closely, it further seems that the concentrations were also influenced by pump rate and pressure (the best results were obtained at 1.0–1.5 mL/min and 0.1 MPa). This was probably also related to the minimum flow rates necessary for the different instruments. Future expeditions need to carefully address this issue.

Sampling and analyzing gas samples from core

During riserless drilling, gas samples were obtained from cores. When a core came into the core cutting area, the temperature of the core liner was measured using a handheld infrared camera (FLIR Systems ThermoCAM SC640) in order to check the presence of gas hydrates in sediment inside the core liner. If sediments contain gas hydrates, their endothermic dissociation leads to low-temperature anomalies in the core liner. When such anomalies were detected, sediment in the core liner was immediately separated into a section and stored in a deep-freezer at -80°C for shore-based analyses.

When a void space was observed in a core liner, a void gas sample was collected from the void space by inserting a gas-tight syringe into the core liner. A 5 mL aliquot of the void gas in the gas-tight syringe was transferred to a 20 mL glass vial.

For headspace gas sampling, after a section of sediment for IW analyses was cut from undisturbed sediment in the core cutting area, sediment for headspace gas analysis was taken from a freshly exposed end of the section. About 5 cm³ or about a half the volume of a 20 mL glass vial of sediment was taken using a cut-off plastic syringe or a cork borer in the case of consolidated sediment. The sediment sample was put into two 20 mL vials that had been weighed prior to sampling. During this expedition, in addi-

tion to the conventional headspace gas sampling, a method using alkaline solution was also carried out using the following procedures (Expedition 316 Scientists, 2009a). For conventional headspace analysis, the vial was capped with a silicon septum and metal crimp cap as soon as possible after its recovery. For the additional analysis using the sample mixed with alkaline solution, 5 mL of 1 M NaOH was added to the vial, and it was immediately sealed with a septum and crimp cap. The vial containing NaOH solution was shaken for 2 min using a tube mixer and was left to stand for at least 24 h at room temperature prior to measurement of isotopic composition of methane. Analysis of isotopic composition of methane using MCIA was subjected to the interference of carbon dioxide so that carbon dioxide in a sample bottle was absorbed into an alkaline solution for a precise determination of isotopic composition of methane.

Offline hydrocarbon gas analysis using a GC-FID

Gas analysis was carried out using an Agilent 6890N GC equipped with an FID. Calibration of the GC was conducted using a standard gas containing low-molecular hydrocarbons (methane, ethane, propane, *iso*-butane, and *n*-butane). The measurement scheme was preprogrammed as follows: a sample bottle was set on an autosampler attached to the GC and was heated at 70°C for 30 min in the autosampler oven. Subsequently, helium carrier gas was introduced into the bottle and the sample was transferred to a sample loop in the autosampler. The gas in the sample loop was injected into the GC. Hydrocarbon concentrations in IW were calculated using the following equation:

$$CH_4 = \frac{[\chi_M \times P_{atm} \times (V_E - W_S / \rho_{Bulk})]}{(R \times T \times W_c \times W_S)}, \quad (8)$$

where

χ_M = molar fraction of methane in the headspace gas (obtained from GC analysis),

P_{atm} = pressure in the vial headspace (assumed to be the measured atmospheric pressure when the vials were sealed),

V_E = volume of the empty vial,

W_S = weight of the whole sediment sample (after sampling, weight of the vial containing sediment was measured, and the weight of the empty vial measured prior to sampling was subtracted to calculate the weight of the sediment sample),

ρ_{Bulk} = bulk density of the sediment sample (determined from MAD measurements on nearby samples),

R = universal gas constant,

T = temperature of the vial headspace in Kelvin, and

W_c = water content of sediment (determined from MAD measurements on nearby samples).

Offline analysis of the stable carbon isotopic composition of methane

After the measurement of hydrocarbon content in the headspace gas, the carbon isotope ratio of methane in headspace gas was determined using the MCIA. For MCIA analysis, methane content must be <1 ppm (see “[On-line analysis of the stable carbon isotopic composition of methane](#)”). Therefore, a portion of the headspace gas was diluted with zero-air (free from hydrocarbons) prior to introducing the sample gas into the MCIA. The needle attached to the syringe was penetrated and 15–20 mL zero-air was transferred into the vial. Then, the headspace gas was sucked into the gas-tight syringe up to 25 mL volume and the diluted gas was injected into the MCIA to measure the isotopic composition of methane. The resulting isotope ratio is given in the same manner as described in “[On-line analysis of the stable carbon isotopic composition of methane.](#)”

Physical properties

Physical properties measurements provide crucial parameters for characterization of consolidation state and deformation of rock formations and are an important tool for integrating cores, cuttings materials, and LWD data. In addition, physical properties are indicators of composition and environmental conditions and are essential for stratigraphic correlation (Blum, 1997), flow properties evaluation, and formation evaluation.

Whole-round sections from cored intervals were first scanned by X-ray CT and then thermally equilibrated at room temperature for ~3 h before any physical properties measurements were conducted. Nondestructive measurements on the whole-round sections included gamma ray attenuation (GRA) density, magnetic susceptibility, NGR, ultrasonic *P*-wave velocity, and noncontact electrical resistivity (NCR) using the MSCL-W (Geotek Ltd., London, United Kingdom). For soft-sediment cores, thermal conductivity was measured on whole-round sections using a full-space needle probe before cores were split into archive and working halves. For cores with highly consolidated or lithified sediment, nondestructive thermal conductivity was measured using a half-space line source. Electrical resistivity was measured using a Wenner array of electrodes on working

halves of soft sediment, and both electrical resistivity and *P*-wave velocity measurements were conducted on discrete samples of consolidated sediment from working halves. MAD measurements were performed on discrete samples from working halves and cuttings. High-resolution digital image photography and color reflectance measurements were performed on archive halves using the MSCL-I and MSCL-C.

For cuttings recovered from Hole C0002F (875.5–2004.5 mbsf), limited measurements were conducted because of the amount of the available material. Unwashed cuttings were analyzed for NGR using the MSCL-W to determine variations in the radioactive counts of the samples and for correlation with LWD gamma ray measurements. Cuttings were rinsed with seawater to remove contamination from drilling mud and sieved into 0.25–1 mm, 1–4 mm, and >4 mm size fractions (see also “[Lithology](#)”). Washed cuttings samples (~40 cm³ total volume) were taken from the 1–4 mm size fraction and samples smaller than 8 mm were hand-picked from the >4 mm fraction for physical properties measurements, including MAD, magnetic susceptibility measurements, and di-electrics and electrical conductivity.

MSCL-W (cores and cuttings)

WRCs were scanned as the core section passed through the MSCL-W. Unwashed bulk cuttings for NGR analysis were packed into a 12 cm long core liner, producing a volume of 400 cm³, and measured by the MSCL-W NGR unit.

Gamma ray attenuation density

A well-collimated gamma ray beam (primary photon energy of 662 keV) is produced by a small (370 MBq) ¹³⁷Cs source. The gamma ray intensity of the beam is measured across the core with a scintillation detector that is composed of a scintillation crystal and an integrated photomultiplier tube. The first-order mechanism for GRA is inelastic scattering by electrons, resulting in a partial energy loss (Compton effect). Because it is directly related to electron density, bulk density (ρ_b) can be determined from the amount of attenuation by

$$\rho_b = (1/\mu d) \times \ln(I_0/I), \quad (9)$$

where

- μ = Compton attenuation coefficient,
- d = sample thickness or outer liner diameter,
- I_0 = gamma source intensity, and
- I = measured intensity through the sample.

Accordingly, the GRA method can provide information about bulk rock density by measuring the attenuation of a gamma ray beam that passes through a core. Here, an empirical approach is used to relate bulk density and GRA. The system is calibrated with a special sealed calibration “core section,” composed of a set of aligned aluminum cylinders of various diameters surrounded by distilled water in a sealed core liner. Density (ρ) depends on the diameter of the aluminum cylinder and spans from $\rho = 1$ g/cm³ (water only) to 2.71 g/cm³ (aluminum only). For the calibration measurement, gamma ray counts were taken for each aluminum cylinder for a count time of 60 s. The resulting $\ln(I)$ was plotted against the product of the known parameters ρ and d of the calibration core section and fitted with a regression line of the following type:

$$\ln(I) = A(\rho \times d)^2 + B(\rho \times d) + C, \quad (10)$$

where d is the internal diameter of the liner and A , B , and C are coefficients determined from the polynomial equation fit. Density measurements on core samples were conducted perpendicular to the core axis every 4 cm. The gamma source collimator is 5 mm in diameter, so each data point reflects the properties of the surrounding 5 mm interval, corresponding to a maximum volume of investigation of ~15.6 cm³.

P-wave velocity

Ultrasonic *P*-wave velocity (V_p) was measured for WRCs by measuring distance between sondes or outer liner diameter (d) and traveltime (t_0):

$$V_p = d/t_0. \quad (11)$$

A linear variable differential transformer, used to measure the outer liner diameter, is integrated with a 500 kHz *P*-wave transmitter/receiver system. The system is mounted horizontally on the MSCL-W and measures d and t_0 perpendicular to core axis at a 4 cm interval. The measured traveltime (t_0) between the transducers is delayed by the pulse traveltime through the liner, the threshold peak detection procedure, and the pulse travel between transducers and the electronic circuitry. Traveltime is corrected for these parameters by calibrating the system using a core liner filled with pure water, which has a known *P*-wave velocity (1480 m/s at 20°C). The corrected *P*-wave velocity through the core (V_{core}) (m/s) is

$$V_{core} = (d - W)/[t_0 - t_w - (d - W)/V_w], \quad (12)$$

where

- W = total wall thickness of the core liner,
- t_w = measured traveltime through the water-filled calibration liner, and
- V_w = known P -wave velocity of pure water at room temperature.

Noncontact electrical resistivity

Bulk electrical resistivity is controlled by solid grain and interstitial water resistivity. Therefore, it provides information about other sediment physical properties such as porosity, tortuosity, permeability, and thermal conductivity. The bulk electrical resistivity (R_e) is defined by the electrical resistance (R) and the geometry of the core measured:

$$R_e = R(A/L), \quad (13)$$

where

- L = distance between the electrodes, and
- A = cross-sectional area of the core.

The ratio between the bulk electrical resistivity and the resistivity of the pore fluid (R_f) alone gives the apparent formation factor (F_a) (Archie, 1947):

$$F_a = R_e/R_f. \quad (14)$$

Whereas the true formation factor ($F = \tau^2/\phi_c$) is a function of the true tortuosity (τ) of the fluid flow path and the connected porosity (ϕ_c), F_a includes the effect of grain-surface conductivity.

For bulk resistivity measurements, the MSCL-W is equipped with a noncontact resistivity sensor that operates by inducing a high-frequency magnetic field in the core using a transmitter coil. The magnetic field induces electrical currents in the core that are inversely proportional to the resistivity. Very small magnetic fields are created in the core by the induced electrical currents and are measured by a receiver coil. To measure these magnetic fields accurately, readings generated from the measuring coils are compared to readings from an identical set of coils operating in air. Calibration is achieved by filling short lengths of core liner with water of known NaCl concentrations to provide a series of calibration samples with known resistivities that are logged on the MSCL-W. A power law calibration equation is found by fitting averaged values of NCR output and corresponding resistivities of the known standards. Electrical resistivity data were obtained at 4 cm intervals along each core section.

Magnetic susceptibility

Magnetic susceptibility is the degree to which a material can be magnetized by an external magnetic field. Magnetic susceptibility was measured with a Bartington Instrument MS2C system with an 8 cm diameter loop sensor on the MSCL-W. A nonsaturating, low-intensity alternating magnetic field (8.0×10^{-4} mA/m root mean square at 0.565 kHz) is produced by an oscillator circuit in the sensor. Any material near the sensor that has a magnetic susceptibility causes a change in the oscillator frequency. This pulse frequency is then converted into a magnetic susceptibility value. With a reference piece of known magnetic susceptibility, the long-term consistency of the calibration is checked regularly. The spatial resolution of the loop sensor is ~ 4 cm, with an accuracy of 5%. Magnetic susceptibility data were obtained at 4 cm intervals with an acquisition time of 1 s.

Natural gamma radiation

NGR emissions were measured on all core sections and unwashed cuttings samples to determine variations in the radioactive counts. The NGR system records radioactive decays of long-period isotopes ^{40}K , ^{232}Th , and ^{238}U in a lead-shielded detector unit. The unit is composed of a scintillator, which is coupled to a photomultiplier tube and connected to a bias base that supplies high-voltage power and a signal preamplifier. Two horizontal and two vertical detection units were mounted in a lead cube-shaped housing around the core. NGR was measured every 16 cm for 30 s on core sections with a resolution of ~ 16 cm.

We also measured the NGR of unwashed cuttings packed in a 12 cm long core liner. Background radiation noise was determined as 34.0 cps by measuring the same size liner filled with distilled water. Two standard radioactive isotopes with known gamma ray emission energies (^{133}Ba and ^{60}Co) were used for the energy calibration and adjustment of the spectral detection windows.

P -wave velocity measurements on MSCL-S (cores)

Ultrasonic P -wave velocity was measured on working-half core sections with the split core multisensor core logger (MSCL-S) in addition to the MSCL-W measurements. V_p measurements were conducted every 4 cm on selected sections from Site C0022 (see “Physical properties” in the “Site C0022” chapter [Strasser et al., 2014c]). The measurement procedures are the same as the MSCL-W V_p measurements discussed above.

Magnetic susceptibility (washed cuttings)

For magnetic susceptibility analysis, $\sim 10 \text{ cm}^3$ of sea-water-rinsed cuttings was taken from vacuum-dried cuttings from the 1–4 mm and the $>4 \text{ mm}$ size fractions and placed into a preweighed paleomagnetic (pmag) cube. The prepared cube, with a volume of 7 cm^3 , was then analyzed with the Kappabridge KLY 3S system (AGICO, Inc.). Sensitivity for the measurement is $3 \times 10^{-8} \text{ SI}$, and intensity and frequency of the field applied are 300 mA/m and 875 Hz , respectively. A standard was measured once a day to ensure long-term quality of the system calibration. A blank empty cube was measured for each continuous series of experiments to determine background impact. Samples were then measured using standard test procedures.

Thermal conductivity (cores)

Thermal conductivity was measured on the working halves at a spacing of at least 1 measurement per core using either a half-space line source probe (HLQ probe; for consolidated cores from Holes C0002H and C0002J and below 337 mbsf in Hole C0022B) or a full-space needle probe (for soft-sediment cores from Holes C0002K, C0002L, and C0021B and above 368 mbsf in Hole C0022B) and a high-precision thermal conductivity meter (TeKa TK04 unit) (Von Herzen and Maxwell, 1959; Vacquier, 1985). For consolidated cores, a representative $\sim 10 \text{ cm}$ long piece from the working half was soaked in a seawater bath at ambient temperature (20°C) for at least 15 min before measurement. The HLQ probe was placed on the flat surface of the specimen with the line probe oriented parallel to the core axis. For soft-sediment cores, the full-space probe was inserted into whole-round sections through a hole drilled through the working-half side of the core liner.

For all thermal conductivity measurements, the measurement started automatically when the monitored temperature in the sample ensured that thermal drift was $<0.4 \text{ mK/min}$ (typically within 1–2 min). During measurement, a calibrated heat source was applied and the rise in temperature was recorded for $\sim 80 \text{ s}$. Thermal conductivity values were based on the observed rise in temperature for a given quantity of heat supplied. Long-term quality of tools and data was validated by a daily calibration on standard Macor samples with known thermal conductivity ($1.652 \text{ W/[m}\cdot\text{K]} \pm 2\%$ for consolidated cores, $1.623 \text{ W/[m}\cdot\text{K]} \pm 2\%$ for soft cores).

Moisture and density measurements (cores and cuttings)

The purpose of MAD measurements is to obtain general physical properties of sediment or rock specimens such as bulk wet density, bulk dry density, grain density, water content, porosity, and void ratio. All the properties can be calculated using phase relations based on direct measurements of wet sample mass (M_{wet}), dry sample mass (M_{dry}), and dry sample volume (V_{dry}) (Noorany, 1984). Standard seawater density ($\rho_f = 1.024 \text{ g/cm}^3$) and salinity ($s = 3.5\%$) are assumed for the phase relations. All the phase relations are based on the assumption that interstitial water fills the pores. For calculation of each physical property, IODP Method C (Blum, 1997) was used for both core samples and cuttings. There is no difference in measurements and calculations between the two sample types, only in sample preparation.

Sample preparation

Core samples

Two MAD samples ($\sim 5 \text{ cm}^3$ each) were taken per core section from either the working half or the “cluster” samples adjacent to whole-round samples. Disturbed parts of core were avoided for sample location. Special care was taken to avoid drilling mud in MAD samples.

Cuttings

Cuttings samples were taken at 5–10 m depth intervals of drilling progress for MAD measurement. After rinsing with seawater, the cuttings of the working portion were segregated into three size fractions (0.25–1 mm, 1–4 mm, and $>4 \text{ mm}$) by sieving. A volume of $\sim 20 \text{ cm}^3$ taken from the 1–4 mm size fraction was used for MAD measurements. Hand-picked pieces from the $>4 \text{ mm}$ size fraction were also used to examine the effect of fraction size on MAD results. Wet cuttings were prepared after sieving by removing excess water by gently wiping cuttings with a Kimwipe until no visible water films were observed on the cuttings surfaces. The samples were then placed into a weighed glass jar.

MAD measurements

M_{wet} was measured using a paired electronic balance system designed to compensate for the ship’s heave. After measurement, the wet samples were placed in a convection oven for $>24 \text{ h}$ at $105^\circ \pm 5^\circ\text{C}$ to dry. The

dry samples were then cooled in a desiccator for at least 1 h before dry mass and volume measurement. M_{dry} was determined using the paired electronic balance system. V_{dry} was measured using a helium-displacement Quantachrome penta-pycnometer with a nominal precision of $\pm 0.04 \text{ cm}^3$. An average of five measurements was reported for each sample.

Phase relations in marine sediment

From the direct measurements of M_{wet} , M_{dry} , and V_{dry} pore fluid mass (M_f), salt mass (M_{salt}), mass of solids excluding salt (M_s), pore fluid volume (V_f), salt volume (V_{salt}), and volume of solids excluding salt (V_s) can be obtained by

$$M_f = (M_{\text{wet}} - M_{\text{dry}})/(1 - s), \quad (15)$$

$$M_{\text{salt}} = M_f - (M_{\text{wet}} - M_{\text{dry}}) = (M_{\text{wet}} - M_{\text{dry}})s/(1 - s), \quad (16)$$

$$M_s = M_{\text{wet}} - M_f = [(M_{\text{dry}} - s \times M_{\text{wet}})]/(1 - s), \quad (17)$$

$$V_f = M_f/\rho_f = (M_{\text{wet}} - M_{\text{dry}})/[(1 - s)\rho_f], \quad (18)$$

$$V_{\text{salt}} = M_{\text{salt}}/\rho_{\text{salt}} = (M_{\text{wet}} - M_{\text{dry}})s/[(1 - s)\rho_{\text{salt}}], \quad (19)$$

and

$$V_s = V_{\text{dry}}/V_{\text{salt}} = V_{\text{dry}} - (M_{\text{wet}} - M_{\text{dry}})s/[(1 - s)\rho_{\text{salt}}], \quad (20)$$

where

- M_{wet} = total mass of the wet sample,
- M_{dry} = mass of the dried sample,
- s = salinity (3.5%),
- ρ_f = density of pore fluid (1.024 g/cm³), and
- ρ_{salt} = density of salt (2.220 g/cm³).

Calculations of physical properties

Water content (W_c) was determined following the methods of the American Society for Testing and Materials (ASTM) designation D2216 (ASTM International, 1990). Corrections are required for salt when measuring the water content of marine samples. In addition to the recommended water content calculation in ASTM D2216 (i.e., the ratio of pore fluid mass to dry sediment mass as percent dry weight), we also calculated the ratio of pore fluid mass to total sample mass (percent wet weight). The equations for water content are

$$W_c (\% \text{ dry wt}) = (M_{\text{wet}} - M_{\text{dry}})/(M_{\text{dry}} - sM_{\text{wet}}), \quad (21)$$

and

$$W_c (\% \text{ wet wt}) = (M_{\text{wet}} - M_{\text{dry}})/[M_{\text{wet}}(1 - s)]. \quad (22)$$

Bulk density (ρ_b), dry density (ρ_d), and grain density (ρ_g) are defined as

$$\rho_b = M_{\text{wet}}/V_{\text{wet}} = M_{\text{wet}}/(V_{\text{dry}} + V_f - V_{\text{salt}}), \quad (23)$$

$$\rho_d = M_{\text{dry}}/V_{\text{wet}} = M_{\text{dry}}/(V_{\text{dry}} + V_f - V_{\text{salt}}), \quad (24)$$

and

$$\rho_g = M_s/V_s = M_s/(V_{\text{dry}} - V_{\text{salt}}), \quad (25)$$

where V_{wet} is the bulk volume of wet sample determined from V_{dry} , V_f , and V_{salt} .

Porosity (ϕ) is given by

$$\phi = V_f/V_{\text{wet}} = V_f/(V_{\text{dry}} + V_f - V_{\text{salt}}), \quad (26)$$

and reported as percentage here ($\phi[\%] = \phi \times 100$). Void ratio (e) is obtained by

$$e = V_f/V_s = (V_{\text{dry}} - V_s)/V_s, \quad (27)$$

Void ratio can also be obtained from ϕ :

$$e = \phi/(1 - \phi). \quad (28)$$

Dielectrics and electrical conductivity (washed cuttings)

Dielectric constant (ϵ_r), which is also called relative permittivity, is a measure of the electrical polarizability of a material (Von Hippel, 1954), whereas the electrical conductivity (σ) is the inverse of electrical resistivity. When a sample is placed in an electric field, the charge carriers within the sample may undergo a translational path through the sample (electrical conduction, in S/m) or undergo temporary displacement and/or reorientation, resulting in an induced field within the sample (electrical polarization, dimensionless).

The complete dielectric versus frequency responses are governed by multiple processes that occur within the rock, from the electron scale to the pore scale (Fig. F20A), and each process (absorption and/or dissipation of energy) is characterized by the speed at which it occurs (Guéguen and Palciauskas, 1994). Resolving these multiple first-order responses over certain frequency ranges is based on the most commonly used model in dielectric spectroscopy: the Cole-Cole model (Cole and Cole, 1941), which is a modified model of the Debye approach (Debye, 1913):

$$\epsilon_r^*(S) = [(\epsilon_s - \epsilon_\infty)/(1 + i\omega\tau)] + \epsilon_\infty, \quad (29)$$

where

- ε_r^* = model (*) of the static permittivity or dielectric constant,
- ε_∞ = optical relative permittivity at “infinite” frequency,
- ε_s = static (S) relative permittivity,
- ω = angular frequency,
- τ = electrical relaxation time, and
- i = imaginary unit of the mathematical complex number.

In the Fourier domain, S becomes a mathematical complex number ($j\omega$) that splits the function into two members: the real ($\varepsilon'_r[\omega]$, also described as the dispersion) and imaginary ($\varepsilon''_r[\omega]$, also described as the absorption) parts that can be written in the form of

$$\varepsilon_r(\omega) = \varepsilon'_r(\omega) - j\varepsilon''_r(\omega). \quad (30)$$

The Cole-Cole model added a smoothing parameter ($\alpha[0 - 1]$) to broaden the low–high frequency transition that was often failing with the Debye model to fit to experimental data.

The Cole-Cole dielectric constant model becomes

$$\varepsilon_r^*(\omega) = \{(\varepsilon_s - \varepsilon_\infty)/(1 + [i\omega\tau]^{1-\alpha})\} + \varepsilon_\infty. \quad (31)$$

Note that if $\alpha = 0$, the Cole-Cole equation (Equation 31) is reduced to the Debye equation (Equation 29). Typical dielectric constants of water are 81 at low frequency and 1.8 at high frequency (Fig. F20B).

Sample preparation and measurement

The experimental flow is based on powdering of cuttings to manufacture a paste by adding some micro-filtered Milli-Q water and using an end-load probe coaxial transmission line in contact with the prepared paste to record the dielectric and electrical conductivity over a frequency range of 30 kHz to 6 GHz.

The end-load probe coaxial transmission line dielectric measurement from the Agilent 85070E instrument is based on an inversion algorithm for the scattering parameters measured for a section of coaxial transmission line terminated against the surface of the sample (Burdette et al., 1980; Stuchly and Stuchly, 1980). It is attached to an Agilent Electronic Calibration (ECal) module (85092-60010) that is connected to a Network Analyzer 8753D from Hewlett Packard (Agilent) using a coaxial cable. A computer controls the network analyzer to start/stop measurement and records the data using an ethernet-to-USB cable attached to the ECal module. The end-load probe is a rapid measurement system, which makes it optimal for large batches of cuttings (Leung and Steig, 1992). Recent work (Josh et al.,

2007, 2012) showed correlations of dielectric properties from sedimentary samples at particular frequency ranges with fluid types (movable and irreducible water), elastic properties (*P*-wave velocity), and some mineralogical characteristics such as specific surface area and cationic exchange capacity. These dielectric relationships indirectly evaluate the occurrence of specific clay minerals that control most of the physical properties of the samples.

The paste preparation consists of grinding the cuttings following the XRD protocol (see “**X-ray diffraction**”) on the seawater-washed 1–4 mm size fraction. A total of 110 samples were analyzed from Hole C0002F. An amount of 20 g of dried powder was mixed with an addition of organic particles filtered in Milli-Q water of exactly 20 mL in a centrifuge NUNC bottle. After shaking by hand for ~5 min to assure that all the salts and agglomerates were dissolved, the mixture was centrifuged at 5000 rpm for 1 h. The decanted water was transferred into a separate plastic jar to measure its salt content using the interstitial water analysis procedure (see “**Geochemistry**”).

The remaining cuttings paste inside the centrifuge bottle was extruded into a separate acrylic jar with known mass, kneaded gently to ensure uniformity (without excess water or trapping air bubbles), and pressed against the end-load coaxial transmission line. Four dielectric measurements were conducted at different locations on each paste sample for quality control. After measurement, the sample was weighed before and after oven drying at 65°C until mass stabilization (± 24 h) to determine bulk density, grain density, and moisture content of the paste corrected for residual salt. For each cuttings sample, we therefore obtain a number of physical attributes of the paste and the pore water salinity estimated from the salt content of the decanted water and porosity results of the cuttings (see the grain/bulk density and porosity results in “**Density and porosity**” in the “Site C0002” chapter [Strasser et al., 2014b]) to complement the permittivity and loss spectrum.

The end-load probe equipment was calibrated and tested against standard material daily prior to sample measurements. Fixture components were measured to remove their electrical responses from the sample data set. It consisted of a measurement of nondielectric material (silicone), followed by measurement of air surrounding the probe, and then measurement of pure water at room temperature. The ECal module calibration was then tested using standard materials from known basic dielectric response (i.e., no charge dispersion with frequency) such as air ($\varepsilon' = 80$), Milli-Q water ($\varepsilon' = 1$), and Teflon ($\varepsilon' = 2$). If the dielectric response of each standard material was flat over the

range of 30 kHz–6 GHz and at the expected dielectric values, the ECal module was calibrated and ready for measurement.

Electrical resistivity (cores)

An Agilent 4294A precision impedance analyzer was employed to determine electrical resistivity from measured impedance. The electrochemical impedance spectrum was acquired from 40 kHz to 10 MHz, and the corresponding magnitude $|Z|$ and phase (θ) of the complex impedance were computed at 2 kHz across the sample in the x -, y -, and z -directions for consolidated cores and only in the x -direction for soft-sediment cores. The 2 kHz frequency was chosen because it is an optimum frequency where no inductance or capacitance occur in the rock (i.e., phase close to 0) and is close to the LWD resistivity frequency for further calibration and comparison. For consolidated cores, electrical resistivity was measured on discrete, cubic samples taken from working halves. The complex impedance was measured by holding the cube between two electrodes, and then electrical resistivity for each direction was computed from measured values and face lengths (L_x , L_y , and L_z). For example, the electrical resistivity in the x -direction (R_x) is

$$R_x = |Z_x| \cos \theta_x (L_y L_z) / L_x. \quad (32)$$

In general, the same cube was used for P -wave and electrical resistivity measurements with a cubic sample (2 cm \times 2 cm \times 2 cm) cut from the working half. Filter papers were soaked before the test in 35 g/L NaCl solution and placed on the sample faces to ensure coupling between the sample and the stainless steel electrodes. As for the P -wave measurements, the cube was rotated to measure impedance in the x -, y -, and z -directions. The vertical anisotropy (α_T) and horizontal anisotropy (α_l) of electrical resistivity were calculated and expressed as a percentage of the mean (e.g., Shipboard Scientific Party, 2001):

$$\alpha_l = 2(\alpha_x - \alpha_y) / (\alpha_x + \alpha_y), \quad (33)$$

and

$$\alpha_T = 2[(\alpha_x + \alpha_y) / 2 - \alpha_z] / [(\alpha_x + \alpha_y) / 2 + \alpha_z], \quad (34)$$

where α_x , α_y , and α_z are electrical resistivity in each axial direction.

For soft-sediment cores, the complex impedance (i.e., equivalent resistivity) was measured using the Agilent 4294A analyzer and a four-pin array consisting of four electrodes spaced 7.5 mm apart. The array was inserted into the working half and measured the

complex impedance, from which the electrical resistivity is calculated:

$$\alpha_y = |Z_y| \cos \theta_y / d_r, \quad (35)$$

where d_r is a constant dependent on the geometry of the electrode array. d_r was determined every 24 h by comparing the measured impedance with an IAPSO standard seawater solution (35 g/L NaCl) of a known electrical impedance.

Ultrasonic P -wave velocity and anisotropy (cores)

P -wave measurements on cubic core samples were conducted along three orthogonal directions for analysis of anisotropy. We took approximately one sample per core section near MAD samples. Cubic samples (~ 2 cm \times 2 cm \times 2 cm) were extracted from working halves. Using a diamond blade saw, cubes were cut with faces orthogonal to the x -, y -, and z -axes of the core reference, respectively (Fig. F21). The orientation of the axes is defined as z pointing downward along the core axis, x pointing into the working half normal to the split-core surface, and y left along the split-core face. Faces were ground with sandpaper to improve contact with sonic sensors. The cubes were soaked in 35 g/L NaCl solution for at least 24 h before P -wave measurement.

P -wave velocity was measured on the cube along each axis using a P -wave logger for discrete samples (Geotek LTD London, United Kingdom), which is composed of a sample holder and an electronic console. The sample holder is equipped with P -wave transducers, a laser distance sensor, and a temperature sensor. The electronic console mounts with the operation PC and the electronic units used for generating an electric pulse and amplifying received signals. The transmitter and receiver are a type of piezocomposite transducers for compressional waves (P -wave) with a frequency of 230 kHz.

The wet sample is set between the two piezoelectric transducers and held by two 1.5 kg weights with a force of ~ 30 N (equivalent to a pressure of 75 kPa) on the contact surfaces. An electric pulse generated by a pulse generator is transformed to the compressional wave by the piezoelectric transducer. The wave propagates through the sample to another piezoelectric transducer which transforms the signal into an output electric pulse. The output signal is amplified, processed through an analog-to-digital converter, and displayed on a PC monitor. Traveltime is picked and logged automatically based on a threshold set by the operators. The length of the P -wave path along the sample is automatically measured at the same

time by a laser distance sensor mounted in the apparatus.

Calibrations of traveltime offset and laser distance sensor were conducted daily. The traveltime offset was determined by placing the two piezoelectric transducers in direct contact and measuring traveltime. This setup provided a time offset of $\sim 9.8 \mu\text{s}$, which was subtracted from the total traveltime to obtain the real traveltime through each sample. Laser distance calibration was conducted by placing the two electric transducers in direct contact and then separating them using a reference box with a height of 2.5 cm.

P -wave velocities along three directions (V_{px} , V_{py} , and V_{pz}) were simply obtained by dividing the sample length by the real traveltime. Horizontal anisotropy (α_1) and vertical anisotropy (α_T) were calculated by

$$\alpha_1 = 2[(V_{px} - V_{py})/(V_{px} + V_{py})], \quad (36)$$

and

$$\alpha_T = 2[(V_{px} + V_{py})/2 - V_{pz}]/[(V_{px} + V_{py})/2 + V_{pz}]. \quad (37)$$

Unconfined compressive strength

For stiffer, more indurated sediment, UCS tests were performed on discrete cuboid samples cut from working-half sections, with approximate dimensional ratios of $1 \times 1 \times 2$, oriented with the x -, y -, and z -axes of the cores. The longer dimension was aligned with the z -axis. These tests provide valuable strength data on samples that are too stiff for analyses with the vane shear or the penetrometer. Care was taken to ensure that the cores were free of defects and the end surfaces of cores were parallel and planar. The samples were placed in a manual hydraulic press (Carver Inc., model 30-12) with a load capacity of 30 tons and aligned so that the load was applied vertically along the cuboid sample axis. In order to measure force, a load cell with a capacity of 300 kN (TEAC Corp., model KR300KN) was placed directly beneath the sample. The sample was manually loaded to failure at a slow rate, and the maximum value registered by the load cell (F_{max}) was recorded. The UCS of the sample was calculated as

$$\text{UCS} = F_{max}/A, \quad (38)$$

where A is the cross-sectional area of the sample. The reading resolution of the load cell is 10 N.

Shear strength measurements

The shear strength of soft-sediment core working halves was measured with an analog vane shear de-

vice (Wkyeham Farrance, model WF23544) and a pocket penetrometer (Geotest E-284B). One measurement per core was taken, with care to avoid disturbed or heterogeneous sediment. Measurements were made with the vane rotation axis and the penetrometer penetration direction aligned with the x -axis of the core.

Undrained shear stress ($S_{u[\text{vane}]}$) was determined by the torque (T) at failure and a constant (K_v) dependent on the geometry of the vane:

$$S_{u[\text{vane}]} = T/K_v. \quad (39)$$

All measurements were made using a vane with a height of 12.7 mm and a blade width of 6.35 mm. Pocket penetrometer measurements provide an estimate of unconfined compressive strength (q_u), which is related to the undrained shear stress ($S_{u[\text{penetrometer}]}$) by

$$S_{u[\text{penetrometer}]} = gq_u/2, \quad (40)$$

where g is the acceleration due to gravity. Penetrometer measurements are taken by pushing a 6.5 mm diameter cylindrical probe into the working half and recording the penetration resistance.

MSCL-I: photo image logger (archive halves)

Digital images of archive-half cores were acquired by a line-scan camera equipped with three charge-coupled devices. Each charge-coupled device has 2048 arrays. The reflected light from the core surface is split into three channels (red, green, and blue [RGB]) by a beam splitter inside the line-scan camera and detected by the corresponding charge-coupled device. The signals are combined and the digital image is reconstructed. A correction is made for any minor mechanical differences among the charge-coupled device responses. A calibration is conducted before scanning each core to compensate for pixel-to-pixel response variation, uneven lighting, and lens effects. After colors of black (RGB = 0) and white (RGB = 255) are calibrated with an f-stop of $f/16$, the light is adjusted to have an adequate gray scale of RGB = 137 at an f-stop of $f/11$. Optical distortion is avoided by precise movement of the camera. Spatial resolution is 100 pixels/cm.

For archive halves from Hole C0021B, image scanning was carried out using the MSCL-S, a GEOTEK product, at KCC. The scanner was calibrated with aperture setting at $F6.7$ and scanned sections in the same aperture condition. A white chart and grayscale card were scanned as quality control measurements while scanning each section. An image file of this in-

strument was stored at approximately every 20 cm interval so that a scanned section image was consistent with several image files. After section scanning, each piece was merged into a whole section image. Resolution of the images taken at KCC was 96 dpi, whereas images obtained on the *Chikyu* were 300 dpi. Merged images were processed by gamma correction at the value of 1.4 using a batch file to change the brightness. This gamma correction value of 1.4 was the same value applied to Expedition 314, 315, 316, 319, 322, 331, and 333 core images in the core descriptions. The images were processed by Adobe Photoshop to adjust RGB values of the grayscale to around 100, 100, and 100, respectively.

MSCL-C: color spectroscopy (archive halves)

A diffuse-reflected spectrophotometer is used to measure core color. The MSCL-C system is an xyz-type aluminum frame equipped with a color spectrophotometer (Konica-Minolta, CM-2600d). Seven core sections can be scanned simultaneously by the sensor unit (including the spectrophotometer and small distance measuring system using a laser sensor). The sensor moves over each section and down at each measurement point to measure the split archive core surface. The reflected light is collected in the color spectrophotometer's integration sphere and divided into wavelengths at a 10 nm pitch (400–700 nm). The color spectrum is then normalized by the source light of the reflectance and calibrated with the measurement of a pure white standard. The measured color spectrum is normally converted to lightness (L^*) and chromaticity variables a^* and b^* (see Blum [1997] for details). These parameters can provide information on relative changes in bulk material composition that are useful to analyze stratigraphic correlation and lithologic characteristics and cyclicity.

Leak-off test

A leak-off test (LOT) is designed to determine the maximum mud weight to prevent well damage by hydraulic fractures, the least principal stress of the formation, and the faulting modes when vertical stress is known (White et al., 2002; Zoback, 2007). In an LOT, the well is first pressurized by pumping drilling mud into the drill string. Once the pressure reaches a peak, pumping is terminated (shut in). In general, the minimum horizontal stress can be inferred from different points on the pressure record as a function of either time or volume (i.e., leak-off pressure [LOP], instantaneous shut in pressure [ISIP], and fracture closure pressure [FCP]) (White et al., 2002).

Injection of mud into an elastically responding borehole leads to a linear relationship between the injected mud volume and borehole pressure. LOP corresponds to the first deviation of the pressure from the linear increase as a result of fracture initiation. Beyond this point, the gradient of pressure versus injected mud volume (dP/dV) decreases because mud escapes into rock formation (Engelder, 1993). ISIP is defined as the point where the steep pressure decrease after shut in deviates from a straight line, and FCP corresponds to the intersection of two tangents to the instantaneous reduction of pressure and the slow reduction in pressure until bleed off. In general, ISIP is visually easier to determine than FCP and is considered to be the best approximation of least principal stress (Zoback, 2007).

The LOT in Hole C0002F was carried out at the base of the 26 inch hole (872.5 mbsf; 2840 m DRF) after the drill-out cement process below the 20 inch casing shoe, which was set during Expedition 326 (Expedition 326 Scientists, 2011). A 3 m long, 17 inch diameter open hole was drilled into the formation below the cement plug. Two cycles of pressurization were conducted because a large amount of drilling mud was lost and LOP was not clearly defined during the first cycle.

Paleomagnetism

Paleomagnetic and rock magnetic investigations on board the *Chikyu* during Expedition 338 were primarily designed to determine the characteristic remanence directions for use in magnetostratigraphic and structural studies of cores. Routine measurements on archive halves were conducted with the SRM.

Laboratory instruments

The paleomagnetism laboratory on board the *Chikyu* houses a large (7.3 m × 2.8 m × 1.9 m) magnetically shielded room with its long axis parallel to the ship transverse. The total magnetic field inside the room is ~1% of Earth's magnetic field. The room is large enough to comfortably handle standard IODP core sections (~150 cm). The shielded room houses the equipment and instruments described in this section.

Superconducting rock magnetometer

The long-core SRM (2G Enterprises, model 760) unit was upgraded from the liquid helium cooled system to the liquid helium-free cooling system "4 K SRM" in June 2011. The 4 K SRM uses a Cryomech pulse tube cryocooler to achieve the required 4 K operating

temperature without the use of liquid helium. The differences between the pulse tube cooled system and the liquid helium cooled magnetometers have significant impact on the system ease of use, convenience, safety, and long-term reliability. The other parts of the SRM were not changed from the previous version. The SRM system is ~6 m long with an 8.1 cm diameter access bore. A 1.5 m split core liner can pass through a magnetometer, an alternating field (AF) demagnetizer, and an anhysteretic remanent magnetizer. The system includes three sets of superconducting pickup coils: two for transverse moment measurements (x - and y -axes) and one for axial moment measurement (z -axis). The noise level of the magnetometer is $<10^{-7}$ A/m for a 10 cm³ volume rock. The magnetometer includes an automated sample handling system (2G804) consisting of aluminum and fiberglass channels designated to support and guide long-core movement. The core itself is positioned in a nonmagnetic fiberglass carriage that is pulled through the channels by a rope attached to a geared high-torque stepper motor. A 2G600 sample degaussing system is coupled to the SRM to allow automatic demagnetization of samples up to 100 mT. The system is controlled by an external computer and enables programming of a complete sequence of measurements and degauss cycles without removing the long core from the holder.

Because Hole C0021B core sampling was conducted at KCC, magnetic measurements were performed using a magnetometer (2G Enterprises, model 760-3.0) at JAMSTEC, Yokosuka. The system specifications are the same as those of the system on the *Chikyu*, but the cooling system on the JAMSTEC magnetometer requires liquid helium.

Spinner magnetometer

A spinner magnetometer, model SMD-88 (Natsuhara Giken Co., Ltd.), was utilized during Expedition 338 for remanent magnetization measurement. The noise level was $\sim 5 \times 10^{-7}$ mA/m², and the measurable range was from 5×10^{-6} to 3×10^{-1} mA/m². Two holders are prepared for the measurements: one (small or short) for the weak samples and the other (large or tall) for the strong samples. Five standard samples with different intensities were prepared to calibrate the magnetometer. Standard 2.5 cm diameter \times 2.2 cm long samples taken with a minicore drill or 7 cm³ cubes could be measured in three or six positions with a typical stacking of 10 spins. The whole sequence took ~1 or 2 min, for three or six positions, respectively.

Alternating field demagnetizer

The DEM-95 AF demagnetizer (Natsuhara Giken Co., Ltd.) is set for demagnetization of standard discrete samples of rock or sediment. The unit is equipped with a sample tumbling system to uniformly demagnetize up to a peak AF of 180 mT.

Thermal demagnetizer

The TDS-1 thermal demagnetizer (Natsuhara Giken Co., Ltd.) has a single chamber for thermal demagnetization of dry samples over a temperature range of room temperature to 800°C. The chamber holds up to 8 or 10 cubic or cylindrical samples, depending on the exact size. The oven requires a closed system of cooling water, which is conveniently placed next to the shielded room. A fan next to the μ -metal cylinder that houses the heating system is used to cool samples to room temperature. The measured magnetic field inside the chamber is <20 nT.

Pulse magnetizer

The MMPM10 pulse magnetizer (Magnetic Measurement, Ltd., United Kingdom; www.magnetic-measurements.com/) can produce a high magnetic field pulse in a sample. The magnetic field pulse is generated by discharging a bank of capacitors through a coil. A maximum field of 9 T with 7 ms pulse duration can be produced by the 1.25 cm diameter coil. The other coil (3.8 cm diameter) generates a maximum field of 2.9 T.

Anisotropy of magnetic susceptibility

The Kappabridge KLY 3S (AGICO, Inc.), which is designed for anisotropy of magnetic susceptibility (AMS) measurement, is also available on the *Chikyu*. Data are acquired from spinning measurements around three axes perpendicular to each other. The deviatoric susceptibility tensor can then be computed. An additional measurement for bulk susceptibility completes the sequence. Sensitivity for AMS measurement is 2×10^{-8} SI. Intensity and frequency of the applied field are 300 mA/m and 875 Hz, respectively. This system also includes the temperature control unit (CS-3/CS-L) for temperature variation of low-field magnetic susceptibility of samples.

Discrete samples and sampling coordinates

Two discrete cubic samples (~ 7 cm³) or minicores (~ 11 cm³) were taken per section from working halves in order to determine paleomagnetic direction, primarily for magnetostratigraphy. The relation

between the orientation of the archive section and that of a discrete sample is shown in Figure F22.

Magnetic reversal stratigraphy

Whenever possible, we offer an interpretation of the magnetic polarity, with the naming convention following that of correlative anomaly numbers prefaced by the letter C (Tauxe et al., 1984). Normal polarity subchrons are referred to by adding suffixes (e.g., n1, n2, etc.) that increase with age. For the younger part of the timescale (Pliocene–Pleistocene), we often use traditional names to refer to the various chrons and subchrons (e.g., Brunhes, Jaramillo, Olduvai, etc.). In general, polarity reversals occurring at core ends have been treated with extreme caution. The ages of polarity intervals used during Expedition 338 are a composite of four previous magnetic polarity timescales (magnetostratigraphic timescale for Neogene by Lourens et al. [2004]) (Table T14).

Cuttings-core-log-seismic integration

During Expedition 338, results from cuttings, cores, and mud-gas analyses and trends in LWD data were used to establish accurate ties to the 2006 Kumano 3-D and 2006 IFREE multichannel seismic (MCS) reflection data sets (e.g., Moore et al., 2007, 2009; Park et al., 2008).

At Site C0002, LWD data and cuttings acquired during riser drilling from 860 to 2005.5 mbsf and core samples within the depth ranges 0–204, 200–500, 475–1057, 900–1040, and 1100–1120 mbsf were available to define logging and lithologic units. At Sites C0012, C0018, and C0021, LWD data were correlated to core samples collected during Expeditions 322 and 333. At Site C0022, LWD data were correlated to cores collected during this expedition. The LWD BHA always included the arcVISION, geoVISION, and TeleScope tools. In addition, the sonicVISION tool was used for Holes C0002F and C0012H. For details regarding the analysis techniques of the independent cuttings, cores, and log data sets, refer to “Logging while drilling,” “Lithology,” “Geochemistry,” and “Physical properties.”

Seismic reflection data

Seismic reflection data acquisition along the NanTroSEIZE transect consisted of two phases. The Kumano 3-D data set acquisition was contracted with Petroleum Geo-Services (PGS) in 2006, covering an area ~12 km × 56 km that extends seaward (in the dip direction) from the Kumano Basin to the frontal thrust

and extends from ~4 km northeast to ~8 km southwest perpendicular to the NanTroSEIZE drilling transect (Moore et al., 2009). The IFREE 3-D data set was acquired by the JAMSTEC vessel R/V *Kairei* also in 2006, covering an area 3.5 km × 52 km that extends seaward from the frontal thrust region to the southern edge of Kashinosaki Knoll (Fig. F1 in the “Expedition 338 summary” chapter [Strasser et al., 2014a]; Park et al., 2008; Expedition 322 Scientists, 2010b).

Seismic processing of the Kumano 3-D data set consisted of three stages (Moore et al., 2009). In the first stage, PGS provided 3-D stack and poststack migration to better understand the regional seismic reflection characteristics for choosing parameters for more detailed processing. During the second stage, Compagnie Générale de Géophysique (CGG) in Kuala Lumpur, Malaysia, processed the data set through 3-D prestack time migration (PSTM). Variable streamer feathering and strong seafloor multiples required several processing steps to fill and regularize all of the bins and provide quality imaging. The third stage consisted of 3-D prestack depth migration (PSDM) performed at JAMSTEC IFREE. The 3-D PSDM clearly images details of faults and small-scale structures but lacks velocity resolution deeper than ~4500–5000 m, near the oceanic basement. Vertical resolution (i.e., $\lambda/4$) is ~5–7 m for the shallowest sub-seabed sediment, ~10–20 m for the deepest sediment drilled so far in NanTroSEIZE, and ~90–125 m at the top basement surface. The IFREE 3-D data volume was also processed through PSTM and then PSDM at IFREE (Park et al., 2008).

Integration with cuttings, core, and log data

Specific intervals in the 3-D seismic data sets were examined where complementary cuttings, cores, or log data were available. For Expedition 338, this meant, explicitly,

- Relating prominent seismic reflections and packages of distinct seismic reflectivity to variations in lithology, unit boundaries, unconformities, or layers with distinct physical and/or geochemical properties;
- Correlating zones of low *P*-wave velocity in the seismic data with mud gas occurrence (riser Hole C0002F) or variations in resistivity and other parameters from LWD data; and
- Linking prominent fault zone reflections (where present) to areas of broken formation in cores, high conductivity in image logs, high density/low porosity in cores and cuttings, and/or age reversals or age gaps defined by biostratigraphy.

Direct comparisons were made between all of the available data using Paradigm's SeisEarth, Schlumberger's Petrel, and the Generic Mapping Tools (GMT) (Wessel and Smith, 1998) to enable an overall assessment and integration of the unit boundaries and internal features determined during the analysis of each independent data set.

X-ray computed tomography

X-ray CT imaging provided information about structures and sedimentological features in cores and helped to assess sample locations and quality for whole-round samples. Our methods followed those in the measurement manual prepared by CDEX/JAMSTEC (3-D X-ray CT Scanning, Version 2.10, 3 July 2012) and used during previous expeditions (e.g., Expedition 337). The manual is based on GE Healthcare (2007), Mees et al. (2003), and Nakano et al. (2000).

The X-ray CT instrument on the *Chikyu* is a GE Yokogawa Medical Systems LightSpeed Ultra 16 capable of scanning a 1.5 m core sample in 5 min, generating 0.625 mm thick slice images. Data generated for each core consist of core-axis-normal planes of X-ray attenuation values with dimensions of 512 × 512 pixels. Data were stored as Digital Imaging and Communication in Medicine (DICOM) formatted files.

Background

The theory behind X-ray CT has been well established through medical research and is very briefly outlined here. X-ray intensity varies as a function of X-ray path length and the linear attenuation coefficient (LAC) of the target material as

$$I = I_0 \times e^{-\eta L}, \quad (41)$$

where

- I = transmitted X-ray intensity,
- I_0 = initial X-ray intensity,
- η = LAC of the target material, and
- L = X-ray path length through the material.

LAC is a function of the chemical composition and density of the target material. The basic measure of attenuation, or radiodensity, is the CT number given in Hounsfield units (HU) and is defined as

$$\text{CT number} = [(\eta_t - \eta_w)/\eta_w] \times 1000, \quad (42)$$

where

- η_t = LAC for the target material, and
- η_w = LAC for water.

The distribution of attenuation values mapped to an individual slice comprises the raw data that are used for subsequent image processing. Successive 2-D slices yield a representation of attenuation values in 3-D pixels referred to as voxels.

Calibration standards used during Expedition 338 were air (CT number = -1000), water (CT number = 0), and aluminum (2477 < CT number < 2487) in an acrylic core mock-up. All three standards were run once daily after air calibration. For each standard analysis, the CT number was determined for a 24.85 mm² area at fixed coordinates near the center of the cylinder. A reference "core sample" for quality control was a three-layer sample: one section was filled with air and one section was filled with both water and a stepped piece of aluminum. This reference standard was used to calibrate CT numbers of air, water, and aluminum when the "Fast Calibration" CT numbers of these three references fell out of normal range.

X-ray CT scan data usage

X-ray CT scans were used during Expedition 338 to

- Examine 3-D features of deformation structures, bioturbation, and so on;
- Distinguish "natural" fracture/faults from drilling-induced fractures;
- Measure strike and dip angles of planar structures such as faults, bedding, veins, and so on;
- Provide an assessment of core and core liner integrity;
- Determine locations for whole-round samples; and
- Identify important structural or sedimentological features to be avoided by whole-round sampling.

X-ray CT scanning was performed immediately after core cutting for time-sensitive (e.g., anelastic strain and interstitial water) whole-round samples to finalize selection of the samples. All whole-round core sections were screened to avoid destructive testing of core samples that might contain critical structural features. This also ensured minimal drilling disturbance of whole-round samples and an assessment of heterogeneity (essential for postexpedition physical and mechanical property studies).

References

- Archie, G.E., 1947. Electrical resistivity—an aid in core analysis interpretation. *AAPG Bull.*, 31(2):350–366.
- Ashi, J., Lallemand, S., Masago, H., and the Expedition 315 Scientists, 2008. NanTroSEIZE Stage 1A: NanTroSEIZE

- megasplay riser pilot. *IODP Prel. Rept.*, 315. doi:10.2204/iodp.pr.315.2008
- ASTM International, 1990. Standard method for laboratory determination of water (moisture) content of soil and rock (Standard D2216–90). In *Annual Book of ASTM Standards for Soil and Rock* (Vol. 04.08): Philadelphia (Am. Soc. Testing Mater.). [revision of D2216-63, D2216-80]
- Berggren, W.A., Hilgen, F.J., Langereis, C.G., Kent, D.V., Obradovich, J.D., Raffi, I., Raymo, M.E., and Shackleton, N.J., 1995. Late Neogene chronology: new perspectives in high-resolution stratigraphy. *Geol. Soc. Am. Bull.*, 107(11):1272–1287. doi:10.1130/0016-7606(1995)107<1272:LNCNPI>2.3.CO;2
- Bernard, B.B., Brooks, J.M., and Sackett, W.M., 1978. Light hydrocarbons in recent Texas continental shelf and slope sediments. *J. Geophys. Res.: Oceans*, 83(C8):4053–4061. doi:10.1029/JC083iC08p04053
- Blow, W.H., 1969. Late middle Eocene to Recent planktonic foraminiferal biostratigraphy. *Proc. Int. Conf. Planktonic Microfossils*, 1:199–422.
- Blum, P., 1997. Physical properties handbook: a guide to the shipboard measurement of physical properties of deep-sea cores. *ODP Tech. Note*, 26. doi:10.2973/odp.tn.26.1997
- Brothers, R.J., Kemp, A.E.S., and Maltman, A.J., 1996. Mechanical development of vein structures due to the passage of earthquake waves through poorly consolidated sediments. *Tectonophysics*, 260(4):227–244. doi:10.1016/0040-1951(96)00088-1
- Burdette, E.C., Cain, F.L., and Seals, J., 1980. In vivo probe measurement technique for determining dielectric properties at VHF through microwave frequencies. *IEEE Trans. Microwave Theory Tech.*, 28(4):414–427. doi:10.1109/TMTT.1980.1130087
- Cande, S.C., and Kent, D.V., 1995. Revised calibration of the geomagnetic polarity timescale for the Late Cretaceous and Cenozoic. *J. Geophys. Res.: Solid Earth*, 100(B4):6093–6095. doi:10.1029/94JB03098
- Cole, K.S., and Cole, R.H., 1941. Dispersion and absorption in dielectrics, 1. Alternating current characteristics. *J. Chem. Phys.*, 9(4):341. doi:10.1063/1.1750906
- Cowan, D.S., 1982. Origin of “vein structure” in slope sediments on the inner slope of the Middle America Trench off Guatemala. In Aubouin, J., von Huene, R., et al., *Init. Repts. DSDP*, 67: Washington, DC (U.S. Govt. Printing Office), 645–650. doi:10.2973/dsdp.proc.67.132.1982
- Cranston, R.E., 1991. Testing a higher resolution interstitial-water method for the Ocean Drilling Program. In Barron, J., Larsen, B., et al., *Proc. ODP, Sci. Results*, 119: College Station, TX (Ocean Drilling Program), 393–399. doi:10.2973/odp.proc.sr.119.173.1991
- Debye, P., 1913. Zur Theorie der anomalen dispersion im Gebiete der langwelligen elektrischen Strahlung. *Ber. Dtsch. Phys. Ges.*, 15:777–793. [reprinted in 1954 in *The Collected Papers of Peter J.W. Debye*: New York (Interscience).]
- Droser, M.L., and Bottjer, D.J., 1986. A semiquantitative field classification of ichnofabric. *J. Sediment. Res.*, 56(4):558–559. doi:10.1306/212F89C2-2B24-11D7-8648000102C1865D
- Droser, M.L., and Bottjer, D.J., 1991. Trace fossils and ichnofabric in Leg 119 cores. In Barron, J., Larsen, B., et al., *Proc. ODP, Sci. Results*, 119: College Station, TX (Ocean Drilling Program), 635–641. doi:10.2973/odp.proc.sr.119.206.1991
- Engelder, T., 1993. *Stress Regimes in the Lithosphere*: Princeton, New Jersey (Princeton Univ. Press).
- Erzinger, J., Wiersberg, T., and Zimmer, M., 2006. Real-time mud gas logging and sampling during drilling. *Geofluids*, 6(3):225–233. doi:10.1111/j.1468-8123.2006.00152.x
- Expedition 314 Scientists, 2009a. Expedition 314 Site C0002. In Kinoshita, M., Tobin, H., Ashi, J., Kimura, G., Lallemand, S., Screatton, E.J., Curewitz, D., Masago, H., Moe, K.T., and the Expedition 314/315/316 Scientists, *Proc. IODP*, 314/315/316: Washington, DC (Integrated Ocean Drilling Program Management International, Inc.). doi:10.2204/iodp.proc.314315316.114.2009
- Expedition 314 Scientists, 2009b. Expedition 314 Site C0004. In Kinoshita, M., Tobin, H., Ashi, J., Kimura, G., Lallemand, S., Screatton, E.J., Curewitz, D., Masago, H., Moe, K.T., and the Expedition 314/315/316 Scientists, *Proc. IODP*, 314/315/316: Washington, DC (Integrated Ocean Drilling Program Management International, Inc.). doi:10.2204/iodp.proc.314315316.116.2009
- Expedition 315 Scientists, 2009a. Expedition 315 methods. In Kinoshita, M., Tobin, H., Ashi, J., Kimura, G., Lallemand, S., Screatton, E.J., Curewitz, D., Masago, H., Moe, K.T., and the Expedition 314/315/316 Scientists, *Proc. IODP*, 314/315/316: Washington, DC (Integrated Ocean Drilling Program Management International, Inc.). doi:10.2204/iodp.proc.314315316.122.2009
- Expedition 315 Scientists, 2009b. Expedition 315 Site C0002. In Kinoshita, M., Tobin, H., Ashi, J., Kimura, G., Lallemand, S., Screatton, E.J., Curewitz, D., Masago, H., Moe, K.T., and the Expedition 314/315/316 Scientists, *Proc. IODP*, 314/315/316: Washington, DC (Integrated Ocean Drilling Program Management International, Inc.). doi:10.2204/iodp.proc.314315316.124.2009
- Expedition 316 Scientists, 2009a. Expedition 316 methods. In Kinoshita, M., Tobin, H., Ashi, J., Kimura, G., Lallemand, S., Screatton, E.J., Curewitz, D., Masago, H., Moe, K.T., and the Expedition 314/315/316 Scientists, *Proc. IODP*, 314/315/316: Washington, DC (Integrated Ocean Drilling Program Management International, Inc.). doi:10.2204/iodp.proc.314315316.132.2009
- Expedition 316 Scientists, 2009b. Expedition 316 Site C0004. In Kinoshita, M., Tobin, H., Ashi, J., Kimura, G., Lallemand, S., Screatton, E.J., Curewitz, D., Masago, H., Moe, K.T., and the Expedition 314/315/316 Scientists, *Proc. IODP*, 314/315/316: Washington, DC (Integrated Ocean Drilling Program Management International, Inc.). doi:10.2204/iodp.proc.314315316.133.2009
- Expedition 316 Scientists, 2009c. Expedition 316 Site C0008. In Kinoshita, M., Tobin, H., Ashi, J., Kimura, G., Lallemand, S., Screatton, E.J., Curewitz, D., Masago, H., Moe, K.T., and the Expedition 314/315/316 Scientists, *Proc. IODP*, 314/315/316: Washington, DC (Integrated

- Ocean Drilling Program Management International, Inc.). doi:10.2204/iodp.proc.314315316.136.2009
- Expedition 319 Scientists, 2010a. Expedition 319 summary. In Saffer, D., McNeill, L., Byrne, T., Araki, E., Toczko, S., Eguchi, N., Takahashi, K., and the Expedition 319 Scientists, *Proc. IODP*, 319: Tokyo (Integrated Ocean Drilling Program Management International, Inc.). doi:10.2204/iodp.proc.319.101.2010
- Expedition 319 Scientists, 2010b. Methods. In Saffer, D., McNeill, L., Byrne, T., Araki, E., Toczko, S., Eguchi, N., Takahashi, K., and the Expedition 319 Scientists, *Proc. IODP*, 319: Tokyo (Integrated Ocean Drilling Program Management International, Inc.). doi:10.2204/iodp.proc.319.102.2010
- Expedition 319 Scientists, 2010c. Site C0009. In Saffer, D., McNeill, L., Byrne, T., Araki, E., Toczko, S., Eguchi, N., Takahashi, K., and the Expedition 319 Scientists, *Proc. IODP*, 319: Tokyo (Integrated Ocean Drilling Program Management International, Inc.). doi:10.2204/iodp.proc.319.103.2010
- Expedition 322 Scientists, 2010a. Methods. In Saito, S., Underwood, M.B., Kubo, Y., and the Expedition 322 Scientists, *Proc. IODP*, 322: Tokyo (Integrated Ocean Drilling Program Management International, Inc.). doi:10.2204/iodp.proc.322.102.2010
- Expedition 322 Scientists, 2010b. Site C0011. In Saito, S., Underwood, M.B., Kubo, Y., and the Expedition 322 Scientists, *Proc. IODP*, 322: Tokyo (Integrated Ocean Drilling Program Management International, Inc.). doi:10.2204/iodp.proc.322.103.2010
- Expedition 322 Scientists, 2010c. Site C0012. In Saito, S., Underwood, M.B., Kubo, Y., and the Expedition 322 Scientists, *Proc. IODP*, 322: Tokyo (Integrated Ocean Drilling Program Management International, Inc.). doi:10.2204/iodp.proc.322.104.2010
- Expedition 326 Scientists, 2011. NanTroSEIZE Stage 3: plate boundary deep riser: top hole engineering. *IODP Prel. Rept.*, 326. doi:10.2204/iodp.pr.326.2011
- Expedition 332 Scientists, 2011. Site C0002. In Kopf, A., Araki, E., Toczko, S., and the Expedition 332 Scientists, *Proc. IODP*, 332: Tokyo (Integrated Ocean Drilling Program Management International, Inc.). doi:10.2204/iodp.proc.332.104.2011
- Expedition 333 Scientists, 2012a. Methods. In Henry, P., Kanamatsu, T., Moe, K., and the Expedition 333 Scientists, *Proc. IODP*, 333: Tokyo (Integrated Ocean Drilling Program Management International, Inc.). doi:10.2204/iodp.proc.333.102.2012
- Expedition 333 Scientists, 2012b. Site C0012. In Henry, P., Kanamatsu, T., Moe, K., and the Expedition 333 Scientists, *Proc. IODP*, 333: Tokyo (Integrated Ocean Drilling Program Management International, Inc.). doi:10.2204/iodp.proc.333.105.2012
- Expedition 333 Scientists, 2012c. Site C0018. In Henry, P., Kanamatsu, T., Moe, K., and the Expedition 333 Scientists, *Proc. IODP*, 333: Tokyo (Integrated Ocean Drilling Program Management International, Inc.). doi:10.2204/iodp.proc.333.103.2012
- Expedition 337 Scientists, 2013. Methods. In Inagaki, F., Hinrichs, K.-U., Kubo, Y., and the Expedition 337 Scientists, *Proc. IODP*, 337: Tokyo (Integrated Ocean Drilling Program Management International, Inc.). doi:10.2204/iodp.proc.337.102.2013
- Fisher, A.T., and Underwood, M.B., 1995. Calibration of an X-ray diffraction method to determine relative mineral abundances in bulk powders using matrix singular value decomposition: a test from the Barbados accretionary complex. In Shipley, T.H., Ogawa, Y., Blum, P., et al., *Proc. ODP, Init. Repts.*, 156: College Station, TX (Ocean Drilling Program), 29–37. doi:10.2973/iodp.proc.ir.156.103.1995
- Fisher, R.V., and Schmincke, H.-U., 1984. *Pyroclastic Rocks*: New York (Springer-Verlag).
- GE Healthcare, 2007. *LightSpeed Series Learning and Reference Guide* (revision 9): Waukesha, Wisconsin (GE Healthcare).
- Glover, P.W.J., Hole, M.J., and Pous, J., 2000. A modified Archie's law for two conducting phases. *Earth Planet. Sci. Lett.*, 180(3–4):369–383. doi:10.1016/S0012-821X(00)00168-0
- Guéguen, Y., and Palciauskas, V., 1994. *Introduction to the Physics of Rocks*: Princeton (Princeton Univ. Press).
- Hanken, N.-M., 1979. The use of sodium tetraphenylborate and sodium chloride in the extraction of fossils from shales. *J. Paleontol.*, 53(3):738–741. <http://www.jstor.org/stable/1304012>
- Heard, T.G., and Pickering, K.T., 2008. Trace fossils as diagnostic indicators of deep-marine environments, middle Eocene Ainsa-Jaca Basin, Spanish Pyrenees. *Sedimentology*, 55(4):809–844. doi:10.1111/j.1365-3091.2007.00922.x
- Hilgen, F.J., Lourens, L.J., and Van Dam, J.A., 2012. The Neogene period. In Gradstein, F.M., Ogg, J.G., Schmitz, M.D., and Ogg, G.M. (Eds.), *The Geologic Time Scale*: Oxford (Elsevier), 923–978. doi:10.1016/B978-0-444-59425-9.00029-9
- Josh, M., Clennell, B., Siggins, T., and Banks, R., 2007. Wideband electrical/dielectric measurements from millihertz to gigahertz frequencies. *SEG Tech. Program Expanded Abstr.*, 1701–1705. doi:10.1190/1.2792821
- Josh, M., Esteban, L., Delle Piane, C., Sarout, J., Dewhurst, D.N., and Clennell, M.B., 2012. Laboratory characterisation of shale properties. *J. Pet. Sci. Eng.*, 88–89:107–124. doi:10.1016/j.petrol.2012.01.023
- Kamikuri, S., Nishi, H., and Motoyama, I., 2007. Effects of late Neogene climatic cooling on North Pacific radiolarian assemblages and oceanographic conditions. *Palaeogeogr., Palaeoclimatol., Palaeoecol.*, 249(3–4):370–392. doi:10.1016/j.palaeo.2007.02.008
- Kamikuri, S., Nishi, H., Motoyama, I., and Saito, S., 2004. Middle Miocene to Pleistocene radiolarian biostratigraphy in the Northwest Pacific Ocean, ODP Leg 186. *Isl. Arc*, 13(1):191–226. doi:10.1111/j.1440-1738.2003.00421.x
- Kirsch, E.G., 1898. Die Theorie der Elastizität und die Bedürfnisse der Festigkeitslehre. *Z. Ver. Dtsch. Ing.*, 42:797–807.
- Leung, P.K., and Steig, R.P., 1992. Dielectric constant measurements: a new, rapid method to characterize shale at

- the wellsite (23887-MS). *SPE/IADC Drill. Conf. Proc.*, 401–408. doi:10.2118/23887-MS
- Li, B., Jian, Z., Li, Q., Tian, J., and Wang, P., 2005. Paleooceanography of the South China Sea since the middle Miocene: evidence from planktonic foraminifera. In Wang, P., and Lipps, J. (Eds.), *Marine Micropaleontology of the South China Sea*. Mar. Micropaleontol., 54(1–2):49–62. doi:10.1016/j.marmicro.2004.09.003
- Lourens, L.J., Hilgen, F.J., Laskar, J., Shackleton, N.J., and Wilson, D., 2004. The Neogene period. In Gradstein, F.M., Ogg, J., et al. (Eds.), *A Geologic Time Scale 2004*: Cambridge (Cambridge Univ. Press), 409–440.
- Manheim, F.T., 1966. A hydraulic squeezer for obtaining interstitial water from consolidated and unconsolidated sediments. *Geol. Surv. Prof. Pap. (U.S.)*, 550-C:256–261.
- Marsaglia, K., Milliken, K., and Doran, L., 2013. IODP smear slides digital reference for sediment analysis, Part 1: Methodology and atlas of siliciclastic and volcanogenic components. *IODP Tech. Note*, 1. doi:10.2204/iodp.tn.1.2013
- Martini, E., 1971. Standard Tertiary and Quaternary calcareous nannoplankton zonation. In Farinacci, A. (Ed.), *Proc. Second Planktonic Conf. Roma 1970*: Rome (Ed. Tecnosci.), 2:739–785.
- Mazzullo, J., and Graham, A.G. (Eds.), 1988. Handbook for shipboard sedimentologists. *ODP Tech. Note*, 8. doi:10.2973/odp.tn.8.1988
- Mazzullo, J.M., Meyer, A., and Kidd, R.B., 1988. New sediment classification scheme for the Ocean Drilling Program. In Mazzullo, J., and Graham, A.G. (Eds.), *Handbook for shipboard sedimentologists*. ODP Tech. Note, 8:44–67. doi:10.2973/odp.tn.8.1988
- Mees, F., Swennen, R., Van Geet, M., and Jacobs, P., 2003. Applications of X-ray computed tomography in the geosciences. *Geol. Soc. Spec. Publ.*, 215(1):1–6. doi:10.1144/GSL.SP.2003.215.01.01
- Moore, G.F., Bangs, N.L., Taira, A., Kuramoto, S., Pangborn, E., and Tobin, H.J., 2007. Three-dimensional splay fault geometry and implications for tsunami generation. *Science*, 318(5853):1128–1131. doi:10.1126/science.1147195
- Moore, G.F., Park, J.-O., Bangs, N.L., Gulick, S.P., Tobin, H.J., Nakamura, Y., Sato, S., Tsuji, T., Yoro, T., Tanaka, H., Uraki, S., Kido, Y., Sanada, Y., Kuramoto, S., and Taira, A., 2009. Structural and seismic stratigraphic framework of the NanTroSEIZE Stage 1 transect. In Kinoshita, M., Tobin, H., Ashi, J., Kimura, G., Lallemand, S., Sreaton, E.J., Curewitz, D., Masago, H., Moe, K.T., and the Expedition 314/315/316 Scientists, *Proc. IODP*, 314/315/316: Washington, DC (Integrated Ocean Drilling Program Management International, Inc.). doi:10.2204/iodp.proc.314315316.102.2009
- Motoyama, I., Niitsuma, N., Maruyama, T., Hayashi, H., Kamikuri, S., Shiono, M., Kanamatsu, T., Aoki, K., Morishita, C., Hagino, K., Nishi, H., and Oda, M., 2004. Middle Miocene to Pleistocene magneto-biostratigraphy of ODP Sites 1150 and 1151, northwest Pacific: sedimentation rate and updated regional geological time-scale. *Isl. Arc*, 13(1):289–305. doi:10.1111/j.1440-1738.2003.00426.x
- Nakano, T., Nakashima, Y., Nakamura, K., and Ikeda, S., 2000. Observation and analysis of internal structure of rock using X-ray CT. *Chishitsugaku Zasshi*, 106(5):363–378.
- Noorany, I., 1984. Phase relations in marine soils. *J. Geotech. Eng.*, 110(4):539–543. doi:10.1061/(ASCE)0733-9410(1984)110:4(539)
- Ocean Drilling Program, 1992. Guidelines for pollution prevention and safety. *JOIDES J.*, 18 (Spec. Iss. 7). http://odplegacy.org/PDF/Admin/JOIDES_Journal/JJ_1992_V18_No7.pdf
- Oda, M., 1977. Planktonic foraminiferal biostratigraphy of the late Cenozoic sedimentary sequence, central Honshu, Japan. *Sci. Repts. Tohoku Univ., 2nd Ser. (Geol.)*, 48:1–76.
- Ogawa, Y., 1980. Beard-like veinlet structure as fracture cleavage in the Neogene siltstone in the Miura and Boso peninsulas, central Japan. *Sci. Rep. Dept. Geol., Kyushu Univ.*, 13:321–327.
- Ohsumi, T., and Ogawa, Y., 2008. Vein structures, like ripple marks, are formed by short-wavelength shear waves. *J. Struct. Geol.*, 30(6):719–724. doi:10.1016/j.jsg.2008.02.002
- Okada, H., and Bukry, D., 1980. Supplementary modification and introduction of code numbers to the low-latitude coccolith biostratigraphic zonation (Bukry, 1973; 1975). *Mar. Micropaleontol.*, 5:321–325. doi:10.1016/0377-8398(80)90016-X
- Park, J.-O., Tsuru, T., No, T., Takizawa, K., Sato, S., and Kaneda, Y., 2008. High-resolution 3D seismic reflection survey and prestack depth imaging in the Nankai Trough off southeast Kii Peninsula. *Butsuri Tansa*, 61:231–241. (in Japanese, with abstract in English)
- Perch-Nielsen, K., 1985. Cenozoic calcareous nannofossils. In Bolli, H.M., Saunders, J.B., and Perch-Nielsen, K. (Eds.), *Plankton Stratigraphy*: Cambridge (Cambridge Univ. Press), 427–554.
- Pimmel, A., and Claypool, G., 2001. Introduction to shipboard organic geochemistry on the *JOIDES Resolution*. *ODP Tech. Note*, 30. doi:10.2973/odp.tn.30.2001
- Raffi, I., 2002. Revision of the early-middle Pleistocene calcareous nannofossil biochronology (1.75–0.85 Ma). *Mar. Micropaleontol.*, 45(1):25–55. doi:10.1016/S0377-8398(01)00044-5
- Raffi, I., Backman, J., Fornaciari, E., Pälike, H., Rio, D., Lourens, L., and Hilgen, F., 2006. A review of calcareous nannofossil astrobiochronology encompassing the past 25 million years. *Quat. Sci. Rev.*, 25(23–24):3113–3137. doi:10.1016/j.quascirev.2006.07.007
- Raffi, I., Backman, J., Rio, D., and Shackleton, N.J., 1993. Plio-Pleistocene nannofossil biostratigraphy and calibration to oxygen isotope stratigraphies from Deep Sea Drilling Project Site 607 and Ocean Drilling Program Site 677. *Paleoceanography*, 8(3):387–408. doi:10.1029/93PA00755
- Richter, C., Acton, G., Endris, C., and Radsted, M., 2007. Handbook for shipboard paleomagnetists. *ODP Tech. Note*, 34. doi:10.2973/odp.tn.34.2007
- Rio, D., 1982. The fossil distribution of coccolithophore genus *Gephyrocapsa* Kamptner and related Plio-Pleisto-

- cene chronostratigraphic problems. *In* Prell, W.L., Gardner, J.V., et al., *Init. Repts. DSDP*, 68: Washington, DC (U.S. Govt. Printing Office), 325–343. doi:10.2973/dsdp.proc.68.109.1982
- Rothwell, R.G., 1989. *Minerals and Mineraloids in Marine Sediments: An Optical Identification Guide*: London (Elsevier).
- Saffer, D., McNeill, L., Byrne, T., Araki, E., Toczko, S., Eguichi, N., Takahashi, K., and the Expedition 319 Scientists, 2010. *Proc. IODP*, 319: Tokyo (Integrated Ocean Drilling Program management International, Inc.). doi:10.2204/iodp.proc.319.2010
- Sakamoto, T., Kuroki, K., Sugawara, T., Aoike, K., Iijima, K., and Sugisaki, S., 2006. Non-destructive X-ray fluorescence (XRF) core-imaging scanner, TATSCAN-F2. *Sci. Drill.*, 2:37–39. http://www.iodp.org/iodp_journals/9_Non_Destructive_X_Ray_SD2.pdf
- Sanfilippo, A., and Nigrini, C., 1998. Code numbers for Cenozoic low latitude radiolarian biostratigraphic zones and GPTS conversion tables. *Mar. Micropaleontol.*, 33(1–2):109–117, 121–156. doi:10.1016/S0377-8398(97)00030-3
- Sanfilippo, A., Westberg-Smith, M.J., and Riedel, W.R., 1985. Cenozoic Radiolaria. *In* Bolli, H.M., Saunders, J.B., and Perch-Nielsen, K. (Eds.), *Plankton Stratigraphy* (Vol. 2): *Radiolaria, Diatoms, Silicoflagellates, Dinoflagellates, and Ichthyoliths*: Cambridge (Cambridge Univ. Press), 631–712.
- Schlumberger, 2007. *geoVISION: Resistivity Imaging for Productive Drilling*: Houston (Schlumberger). <http://www.slb.com/~media/Files/drilling/brochures/lwd/vision/geovision.pdf>
- Schlumberger, 2010a. *Drilling Dynamics Sensors and Optimization*: Houston (Schlumberger). http://www.slb.com/~media/Files/drilling/brochures/mwd/drilling_dynamics_sensors_opt_br.pdf
- Schlumberger 2010b. *sonicVISION*: Houston (Schlumberger). <http://www.slb.com/~media/Files/drilling/brochures/lwd/vision/sonicvision.pdf>
- Schlumberger, 2011. *Drilling Tools: Quick Reference Guide*: Houston (Schlumberger). http://www.slb.com/~media/Files/drilling/specs/ht_quick_ref_guide.pdf
- Shepard, F.P., 1954. Nomenclature based on sand-silt-clay ratios. *J. Sediment. Petrol.*, 24(3):151–158. <http://jse-dres.sepmonline.org/cgi/reprint/24/3/151.pdf>
- Shipboard Scientific Party, 1991. Explanatory notes. *In* Taira, A., Hill, I., Firth, J.V., et al., *Proc. ODP, Init. Repts.*, 131: College Station, TX (Ocean Drilling Program), 25–60. doi:10.2973/odp.proc.ir.131.104.1991
- Shipboard Scientific Party, 2001. Explanatory notes. *In* Moore, G.F., Taira, A., Klaus, A., et al., *Proc. ODP, Init. Repts.*, 190: College Station, TX (Ocean Drilling Program), 1–51. doi:10.2973/odp.proc.ir.190.103.2001
- Shipley, T.H., Ogawa, Y., Blum, P., et al., 1995. *Proc. ODP, Init. Repts.*, 156: College Station, TX (Ocean Drilling Program). doi:10.2973/odp.proc.ir.156.1995
- Strasser, M., Dugan, B., Kanagawa, K., Moore, G.F., Toczko, S., Maeda, L., Kido, Y., Moe, K.T., Sanada, Y., Esteban, L., Fabbri, O., Geersen, J., Hammerschmidt, S., Hayashi, H., Heirman, K., Hüpers, A., Jurado Rodriguez, M.J., Kameo, K., Kanamatsu, T., Kitajima, H., Masuda, H., Milliken, K., Mishra, R., Motoyama, I., Olcott, K., Oohashi, K., Pickering, K.T., Ramirez, S.G., Rashid, H., Sawyer, D., Schleicher, A., Shan, Y., Skarbak, R., Song, I., Takeshita, T., Toki, T., Tudge, J., Webb, S., Wilson, D.J., Wu, H.-Y., and Yamaguchi, A., 2014a. Expedition 338 summary. *In* Strasser, M., Dugan, B., Kanagawa, K., Moore, G.F., Toczko, S., Maeda, L., and the Expedition 338 Scientists, *Proc. IODP*, 338: Yokohama (Integrated Ocean Drilling Program). doi:10.2204/iodp.proc.338.101.2014
- Strasser, M., Dugan, B., Kanagawa, K., Moore, G.F., Toczko, S., Maeda, L., Kido, Y., Moe, K.T., Sanada, Y., Esteban, L., Fabbri, O., Geersen, J., Hammerschmidt, S., Hayashi, H., Heirman, K., Hüpers, A., Jurado Rodriguez, M.J., Kameo, K., Kanamatsu, T., Kitajima, H., Masuda, H., Milliken, K., Mishra, R., Motoyama, I., Olcott, K., Oohashi, K., Pickering, K.T., Ramirez, S.G., Rashid, H., Sawyer, D., Schleicher, A., Shan, Y., Skarbak, R., Song, I., Takeshita, T., Toki, T., Tudge, J., Webb, S., Wilson, D.J., Wu, H.-Y., and Yamaguchi, A., 2014b. Site C0002. *In* Strasser, M., Dugan, B., Kanagawa, K., Moore, G.F., Toczko, S., Maeda, L., and the Expedition 338 Scientists, *Proc. IODP*, 338: Yokohama (Integrated Ocean Drilling Program). doi:10.2204/iodp.proc.338.103.2014
- Strasser, M., Dugan, B., Kanagawa, K., Moore, G.F., Toczko, S., Maeda, L., Kido, Y., Moe, K.T., Sanada, Y., Esteban, L., Fabbri, O., Geersen, J., Hammerschmidt, S., Hayashi, H., Heirman, K., Hüpers, A., Jurado Rodriguez, M.J., Kameo, K., Kanamatsu, T., Kitajima, H., Masuda, H., Milliken, K., Mishra, R., Motoyama, I., Olcott, K., Oohashi, K., Pickering, K.T., Ramirez, S.G., Rashid, H., Sawyer, D., Schleicher, A., Shan, Y., Skarbak, R., Song, I., Takeshita, T., Toki, T., Tudge, J., Webb, S., Wilson, D.J., Wu, H.-Y., and Yamaguchi, A., 2014c. Site C0022. *In* Strasser, M., Dugan, B., Kanagawa, K., Moore, G.F., Toczko, S., Maeda, L., and the Expedition 338 Scientists, *Proc. IODP*, 338: Yokohama (Integrated Ocean Drilling Program). doi:10.2204/iodp.proc.338.107.2014
- Stuchly, M.A., and Stuchly, S.S., 1980. Coaxial line reflection methods for measuring dielectric properties of biological substances at radio and microwave frequencies—a review. *IEEE Trans. Instrum. Meas.*, 29(3):176–183. doi:10.1109/TIM.1980.4314902
- Tauxe, L., Tucker, P., Peterson, N.P., and LaBrecque, J.L., 1984. Magnetostratigraphy of Leg 73 sediments. *In* Hsü, K.J., LaBrecque, J.L., et al., *Init. Repts. DSDP*, 73: Washington, DC (U.S. Govt. Printing Office), 609–621. doi:10.2973/dsdp.proc.73.123.1984
- Thompson, P.R., Bé, A.W.H., Duplessy, J.-C., and Shackleton, N.J., 1979. Disappearance of pink-pigmented *Globigerinoides ruber* at 120,000 yr BP in the Indian and Pacific oceans. *Nature (London, U. K.)*, 280(5723):554–558. doi:10.1038/280554a0
- Underwood, M.B., Basu, N., Steurer, J., and Udas, S., 2003. Data report: normalization factors for semiquantitative X-ray diffraction analysis, with application to DSDP Site 297, Shikoku Basin. *In* Mikada, H., Moore, G.F., Taira, A., Becker, K., Moore, J.C., and Klaus, A. (Eds.), *Proc. ODP, Sci. Results*, 190/196: College Station, TX (Ocean Drilling Program), 1–28. doi:10.2973/iodp.proc.sr.190196.203.2003

- Vacquier, V., 1985. The measurement of thermal conductivity of solids with a transient linear heat source on the plane surface of a poorly conducting body. *Earth Planet. Sci. Lett.*, 74(2–3):275–279. doi:10.1016/0012-821X(85)90027-5
- Von Herzen, R., and Maxwell, A.E., 1959. The measurement of thermal conductivity of deep-sea sediments by a needle-probe method. *J. Geophys. Res.*, 64(10):1557–1563. doi:10.1029/JZ064i010p01557
- Von Hippel, A.R., 1954. *Dielectric Materials and their Applications*: Cambridge (MIT Press).
- Wade, B.S., Pearson, P.N., Berggren, W.A., and Pälike, H., 2011. Review and revision of Cenozoic tropical planktonic foraminiferal biostratigraphy and calibration to the geomagnetic polarity and astronomical time scale. *Earth-Sci. Rev.*, 104(1–3):111–142. doi:10.1016/j.earsci-rev.2010.09.003
- Wessel, P., and Smith, W.H.F., 1998. New, improved version of Generic Mapping Tools released. *Eos, Trans. Am. Geophys. Union*, 79(47):579. doi:10.1029/98EO00426
- Wheat, C.G., Boulègue, J., and Mottl, M.J., 1994. A technique for obtaining pore water chemical composition from indurated and hydrothermally altered sediment and basalt: the ground rock interstitial normative determination (grind). In Mottl, M.J., Davis, E.E., Fisher, A.T., and Slack, J.F. (Eds.), *Proc. ODP, Sci. Results*, 139: College Station, TX (Ocean Drilling Program), 429–437. doi:10.2973/odp.proc.sr.139.234.1994
- White, A.J., Traugott, M.O., and Swarbrick, R.E., 2002. The use of leak-off tests as means of predicting minimum in-situ stress. *Pet. Geosci.*, 8(2):189–193. doi:10.1144/pet-geo.8.2.189
- Whiticar, M.J., 1994. Correlation of natural gases with their source. In Magoon, L.B., and Dow, W.G. (Eds.), *The Petroleum System—From Source to Trap*. AAPG Mem., 60:261–283.
- Whiticar, M.J., 1999. Carbon and hydrogen isotope systematics of bacterial formation and oxidation of methane. *Chem. Geol.*, 161(1–3):291–314. doi:10.1016/S0009-2541(99)00092-3
- Wiersberg, T., and Erzinger, J., 2007. A helium isotope cross-section study through the San Andreas Fault at seismogenic depths. *Geochem., Geophys., Geosyst.*, 8(1):Q01002. doi:10.1029/2006GC001388
- Wiersberg, T., and Erzinger, J., 2011. Chemical and isotope compositions of drilling mud gas from the San Andreas Fault Observatory at Depth (SAFOD) boreholes: implications on gas migration and the permeability structure of the San Andreas Fault. *Chem. Geol.*, 284(1–2):148–159. doi:10.1016/j.chemgeo.2011.02.016
- Young, J.R., 1998. Neogene. In Bown, P.R. (Ed.), *Calcareous Nannofossil Biostratigraphy*: Dordrecht, The Netherlands (Kluwer Academic Publ.), 225–265.
- Zoback, M.D., 2007. *Reservoir Geomechanics*: Cambridge (Cambridge Univ. Press).

Publication: 13 January 2014
MS 338-102

Figure F1. Concentric string tool used during reaming while drilling, Hole C0002F.

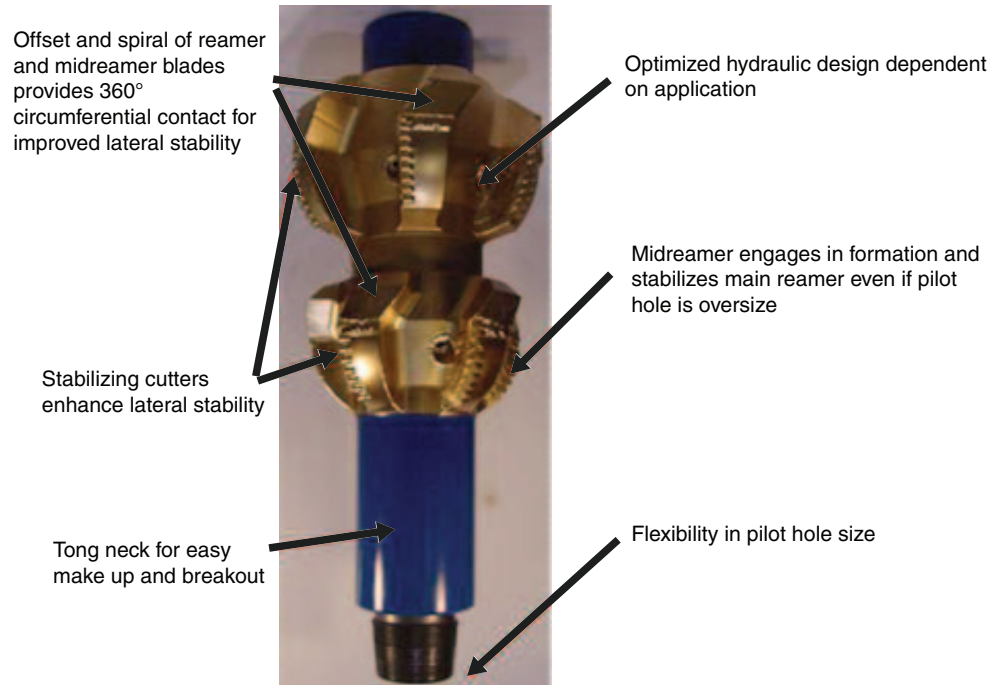


Figure F2. Hydromechanical Anderreamer supplied by National Oilwell Varco used for reaming while drilling, Hole C0002F.



Figure F3. Drawings of bottom-hole assembly configurations used during Expedition 338. **A.** Riser configuration, Hole C0002F. **B.** Riserless configuration, Hole C0012H. **C.** Riserless configuration, Holes C0018B, C0021A, and C0022A. Total length from tool zero to each measurement point is shown next to the tools. BHA diameter dimensions are 12.25 inches (31.1 cm) for the bit; 21 cm for geoVISION, arcVISION, TeleScope, and sonicVISION; and a maximum of 20 inches (50 cm) for the underreamer. MWD = measurement while drilling, PDC = polycrystalline diamond compact.

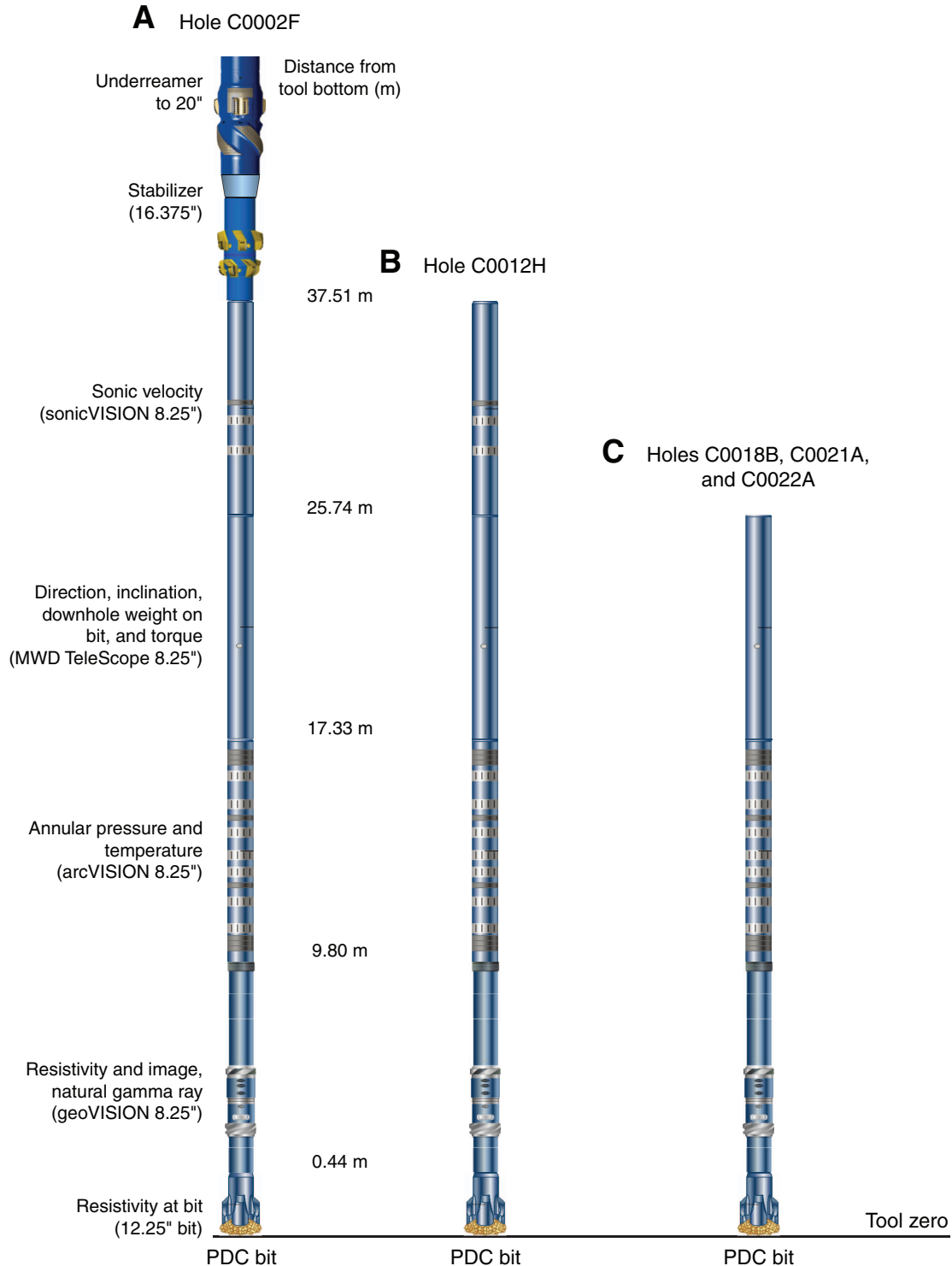




Figure F4. In each pair, the left panel is an example of a silty claystone (gray) and sandstone (yellow) formation, and the right panel is the theoretical fraction of silty claystone (gray) and sandstone (yellow) from cuttings for the same formation, assuming cuttings are produced only by the 12¼ inch bit and the 20 inch underreamer. **A.** Silty claystone and sandstone. **B.** Sandstone bed (50 m thick) bounded by silty claystone. **C.** Sandstone bed (15 m thick) bounded by silty claystone.

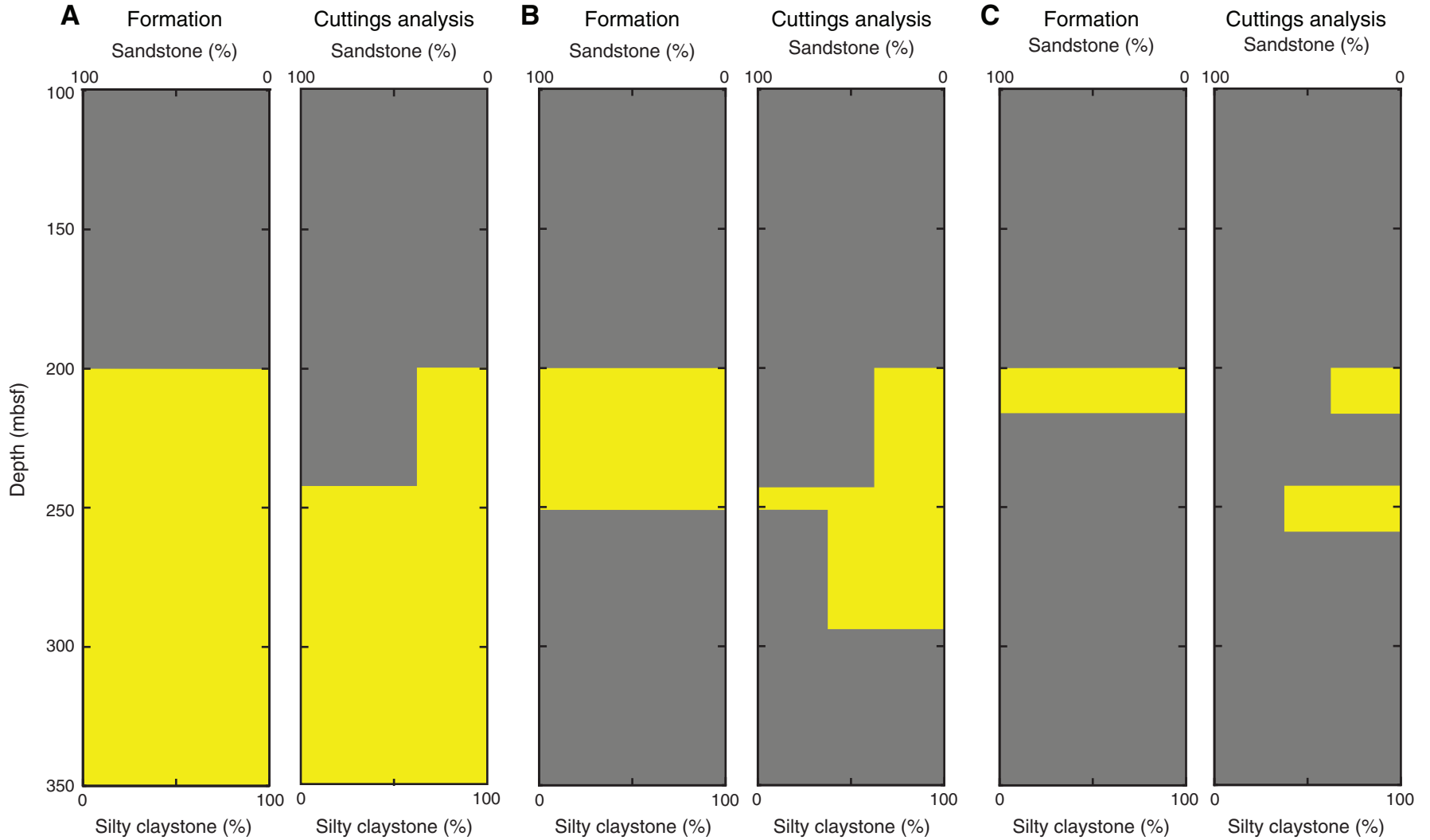


Figure F5. Diagram of cuttings analysis flow, Expedition 338. NGR = natural gamma radiation, S.W. = seawater, QA/QC = quality assurance/quality control, MAD = moisture and density, XRF = X-ray fluorescence, XRD = X-ray diffraction, CA = carbonate analyzer, EA = elemental analyzer.

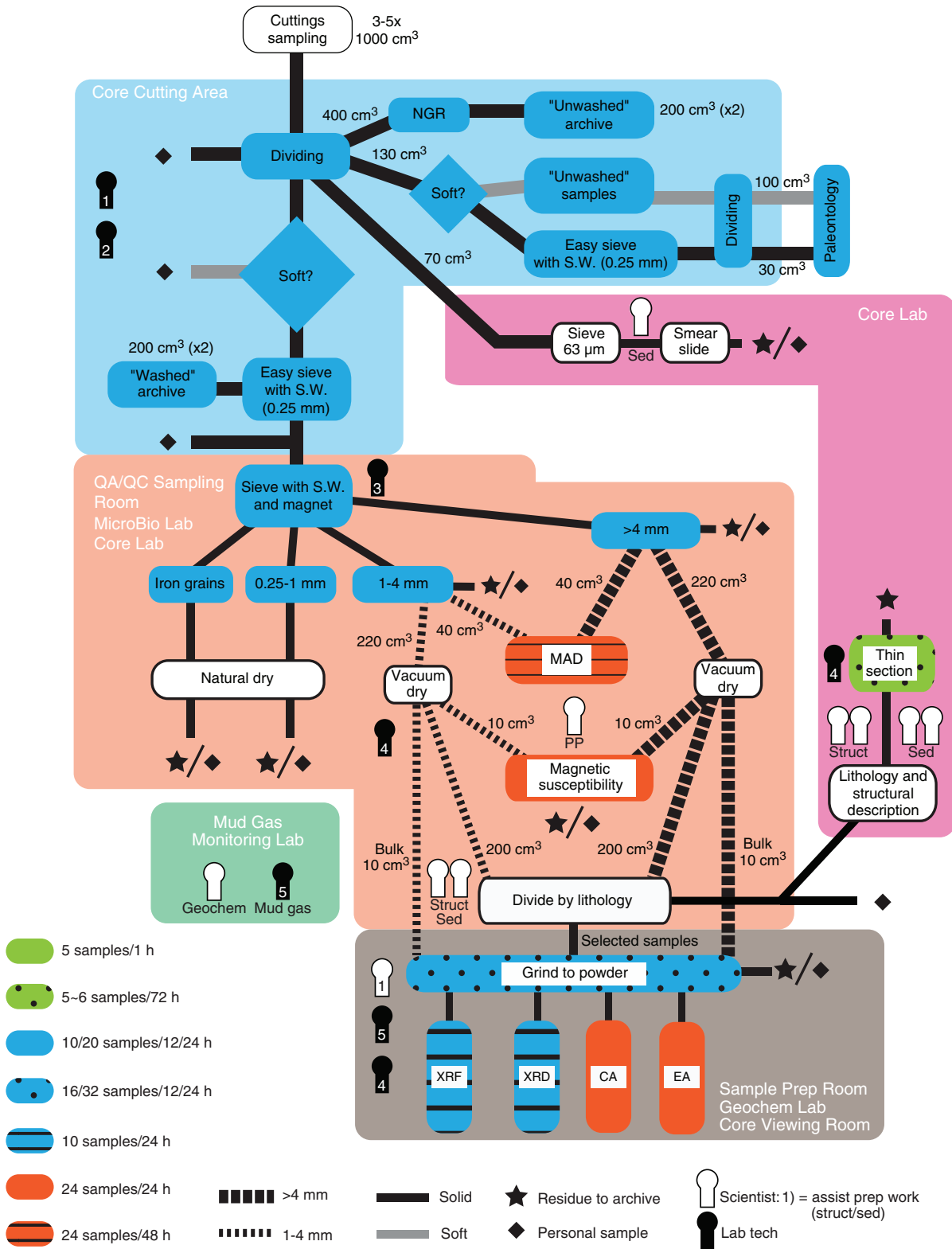


Figure F6. Diagram of core analysis flow, Expedition 338. PPE = personal protective equipment, HS = headspace sample, GC-FID = gas chromatograph–flame ionization detector, HC = hydrocarbon. IW = interstitial water, MBIO = microbiology, ASR = anelastic strain recovery, RMS = routine microbiology sample, KEWR = Katrina Edwards whole round. CT = computed tomography. WR = whole round. MSCL-W = whole-round multisensor core logger, GRA = gamma ray attenuation, MS = magnetic susceptibility, PWV = *P*-wave velocity, NCR = non-contact electrical resistivity, NGR = natural gamma radiation. MSCL-I = photo image logger, VCD = visual core description, MSCL-C = color spectroscopy logger, SRM = superconducting rock magnetometer. MAD = moisture and density, UCS = unconfined compressive strength, P-mag = paleomagnetic measurement for discrete samples with SRM, SEM-EDS = scanning electron microscope–energy dispersive spectrometry. GRIND = ground rock interstitial normative determination. ICP-AES = inductively coupled plasma–atomic emission spectroscopy, ICP-MS = inductively coupled plasma–mass spectrometry, IC = ion chromatography, UV = ultraviolet visible spectrophotometry. XRD = X-ray diffraction, XRF = X-ray fluorescence, CA = carbonate analyzer, EA = elemental analyzer.

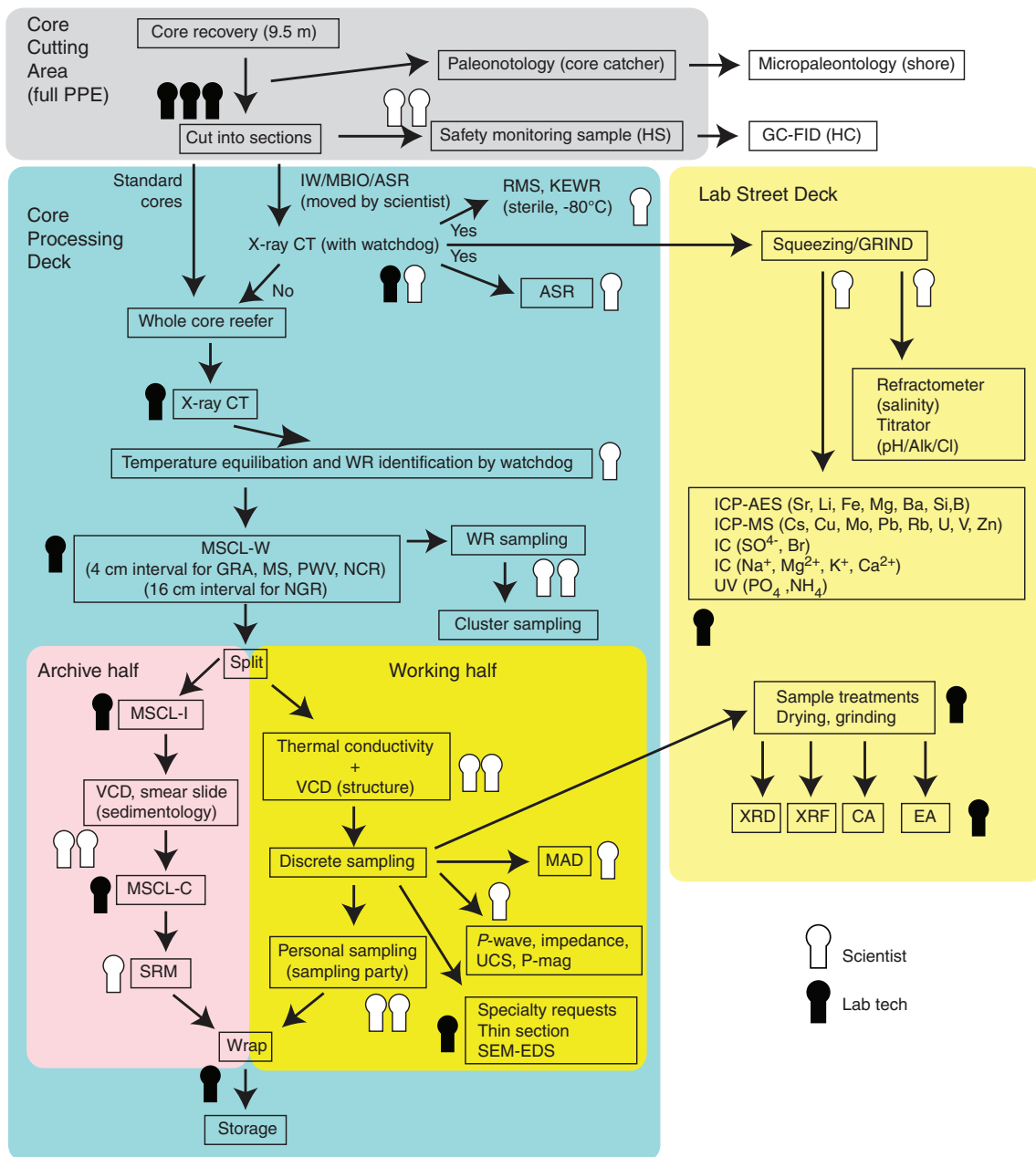


Figure F7. A. Graphic patterns and symbols used on visual core descriptions, Expedition 338.



Figure F7 (continued). B. Macroscopic cuttings patterns and symbols.

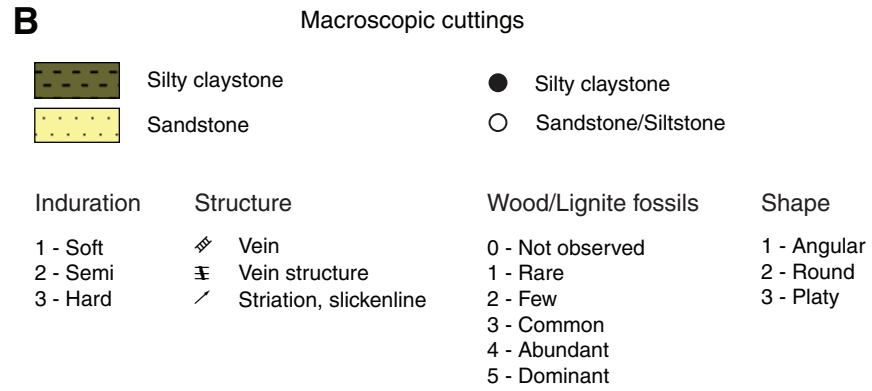


Figure F8. Examples of X-ray diffractograms for mixtures of standard minerals showing the positions of diagnostic peaks used to calculate relative mineral abundance. Green line = baseline subtraction.

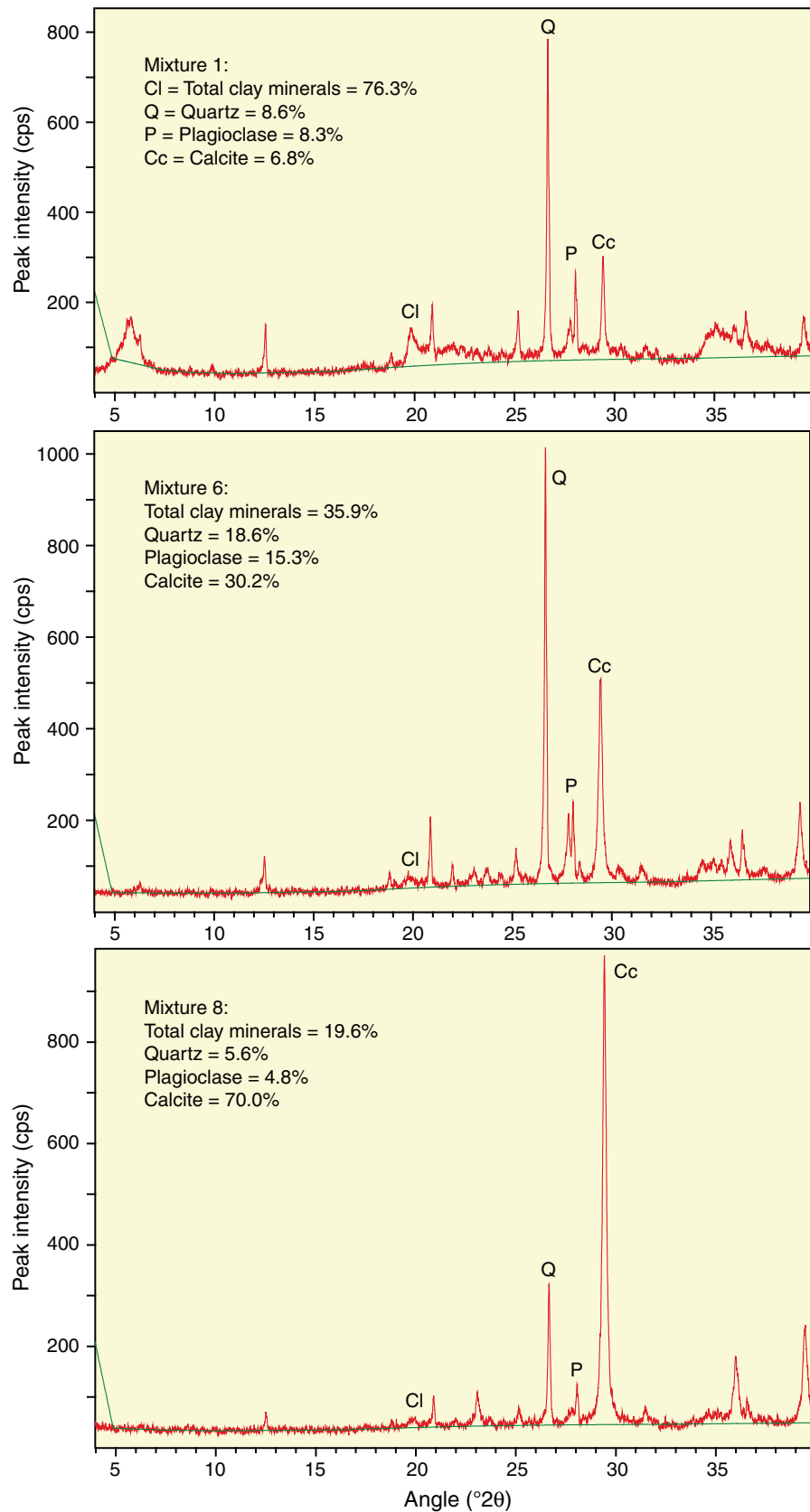




Figure F9. Log sheet (structural geology observation sheet) used to record structural observations and measurements from working half of split cores.

CHIKYU Operation

Last Update 3/June/2011

Structural Geology Observation Sheet

No. _____

Exp. : Site : Hole : Core : Observer : Summary:

Section No.	Structure ID	Top of Struct	Bottom of Struct	ave. depth	Thickness of Struct	Core face app. Dip		2nd app. Dip		Striation on surface		Coherent interval (for P-mag)		P-mag pole		Notes
						az.	dip	az.	dip	rake (5-90)	from (= 1, 90 or 270) * Top → "1" Bottom → "-1"	top	bottom	az./trend	dip	
Grid area for data entry																

Figure F10. Modified protractor used to measure apparent dip angles, bearings, plunge angles, and rakes of planar and linear features observed in working halves of split cores.

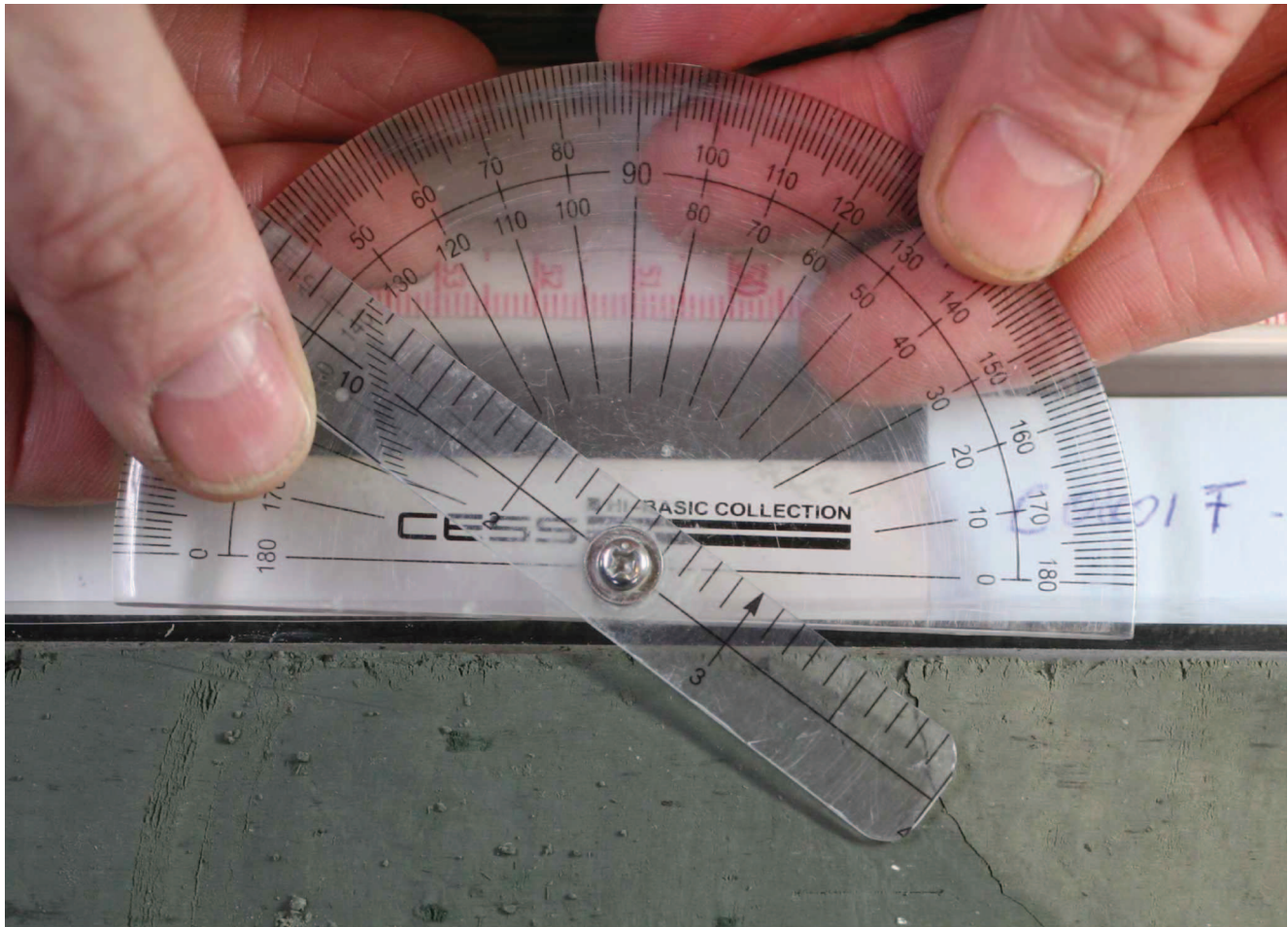


Figure F11. Core coordinate system with x -, y -, and z -axes used in orientation data measurements.

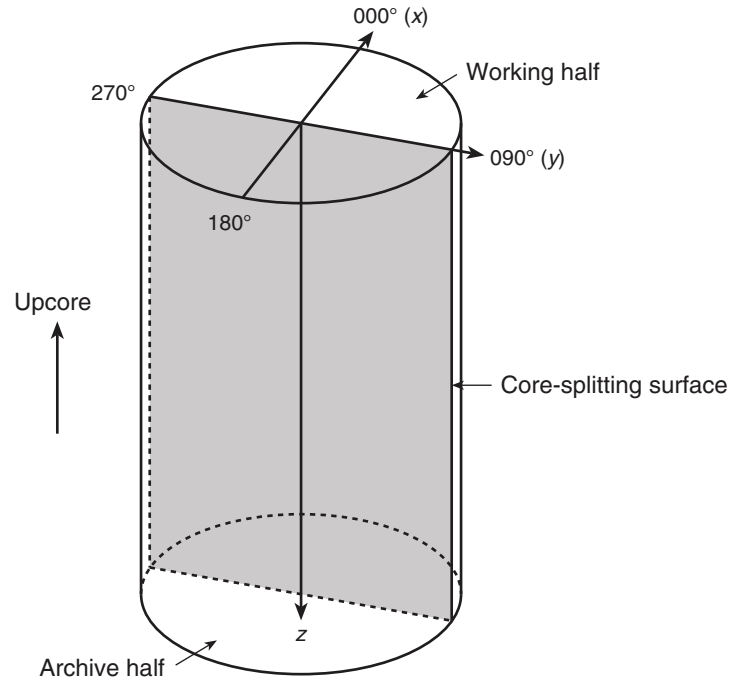


Figure F12. Determination of the orientation of a geological plane (shaded) from two auxiliary measurements. The first auxiliary measurement is taken on flat-lying split core surface and consists of measuring the bearing (α_1) and the plunge angle (β_1) of the trace of the plane on the split surface. The second auxiliary measurement is taken on a surface perpendicular to the flat-lying split core surface and containing the core axis. It consists of measuring the bearing (α_2) and the plunge angle (β_2) of the trace of the plane on the surface.

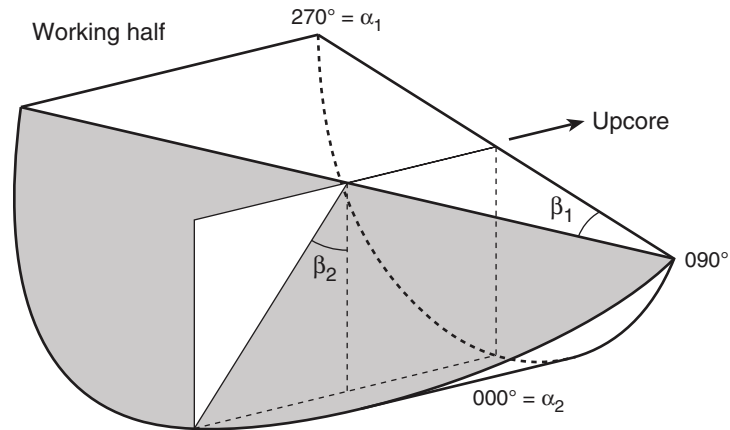


Figure F13. Rake (ϕ_a) measurement of slickenlines on a fault surface. In this example, the slickenlines rake from the azimuth of the plane that points in the western (270°) quadrant in the core reference frame.

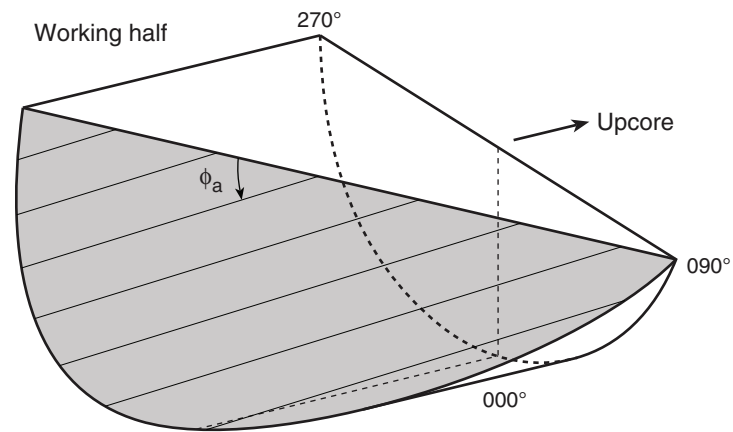


Figure F16. Diagram of mud extraction system, third-party sampling tools, mud-gas monitoring laboratory (modified from Expedition 319 Scientists, 2010b, and Expedition 337 Scientists, 2013), Expedition 338. **A.** Drilling mud is directed into a flow splitter, where mud flow is split into either the Gumbo separators or the degasser. Afterward, mud and cuttings are divided by a shaker screen. **B.** The remaining mud is transferred to mud tanks via sand traps and can be pumped down again. **C.** The degasser that separates drilling mud and dissolved gas is installed directly behind the flow splitter, where drilling mud is exposed to air for the first time. Extracted gas is transferred to the mud-gas monitoring laboratory. **D.** A safety valve regulates gas pressure and protects the gas monitoring system from overflowing mud. **E.** Gas is directed through an IsoTube sampling system to the dehydration module or first to a **(F)** third-party sampling line, which consisted here of glass flasks and copper tubes. After the gas is dried and cleaned, another IsoTube sampling system can collect gas samples for later analyses; a GC with flame ionization detector (FID), quadruple mass spectrometer, radon detector, and MCIA are connected to the pipeline to allow real-time monitoring of gas and methane carbon isotope composition.

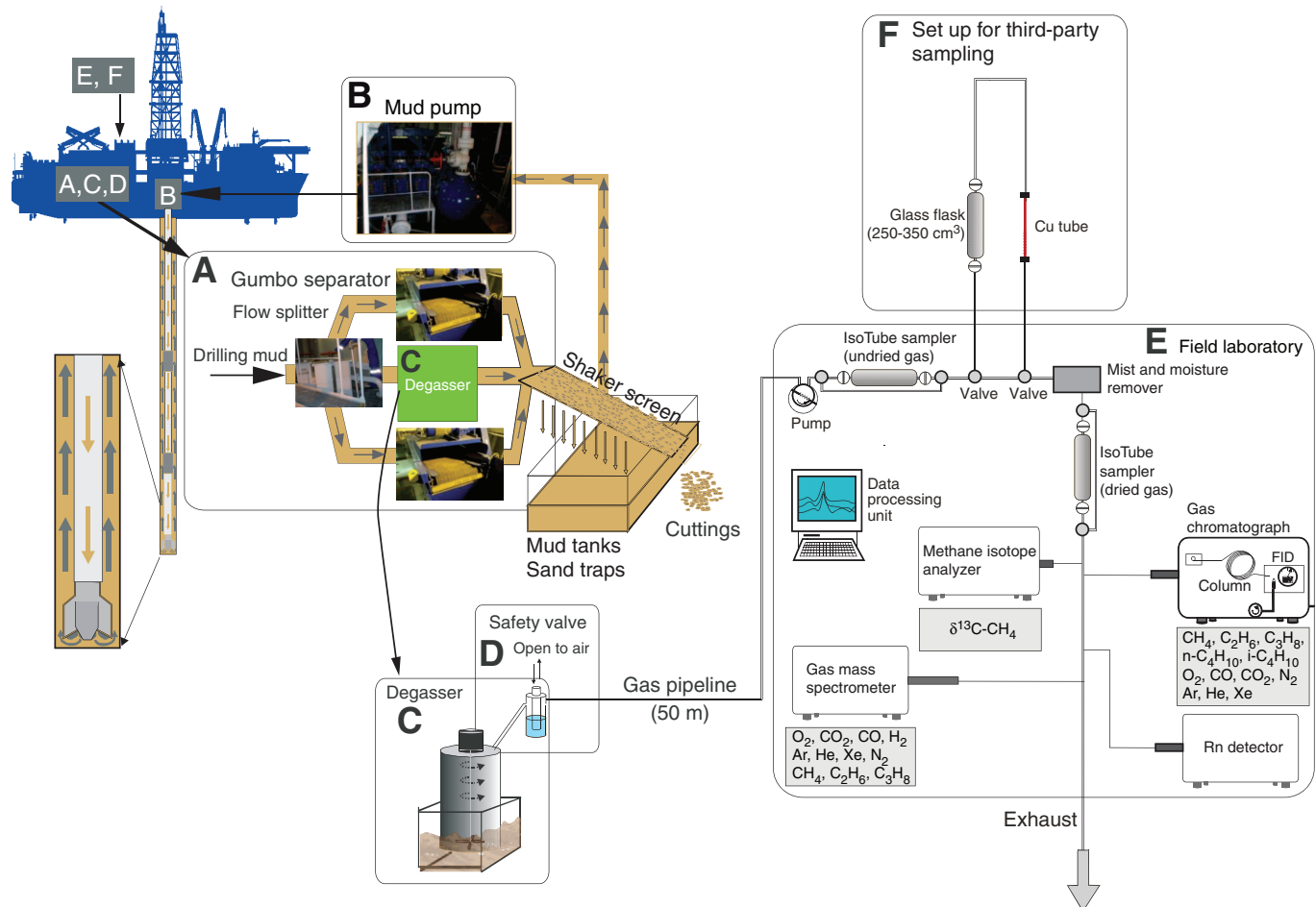


Figure F17. Diagram for classification of biogenic and thermogenic methane sources based on C_1/C_2 ratios and sediment temperature (from Pimmel and Claypool, 2001). Low C_1/C_2 ratios indicate the presence of thermogenic methane. TOC = total organic carbon.

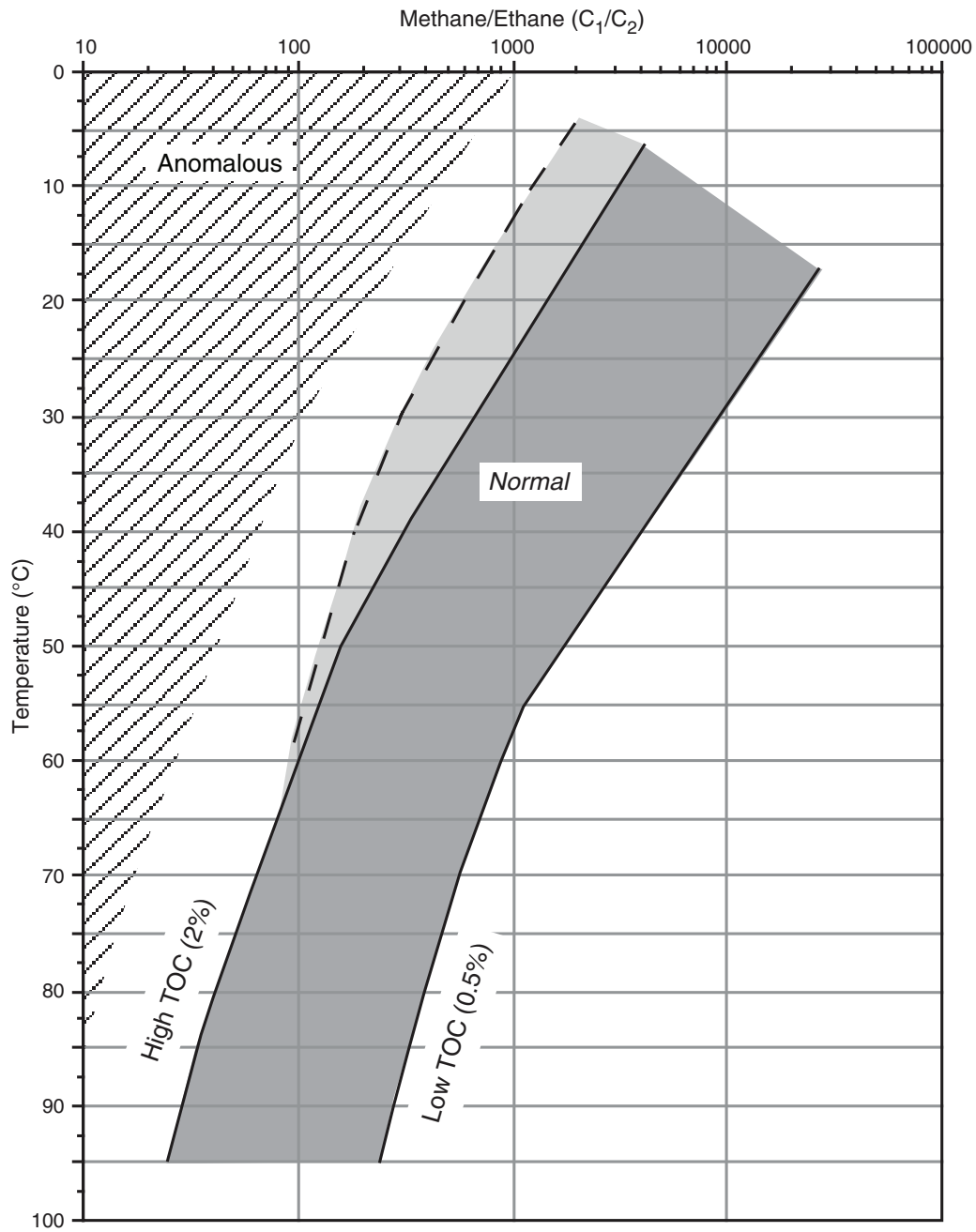


Figure F18. Bernard diagram after Bernard et al. (1978) for classification of hydrocarbon gas sources based on $\delta^{13}\text{C}$ values and the Bernard parameter (from Whiticar, 1999). Calculated Lines A and B show examples for end-members of mixed gas. VPDB = Vienna Pee Dee belemnite.

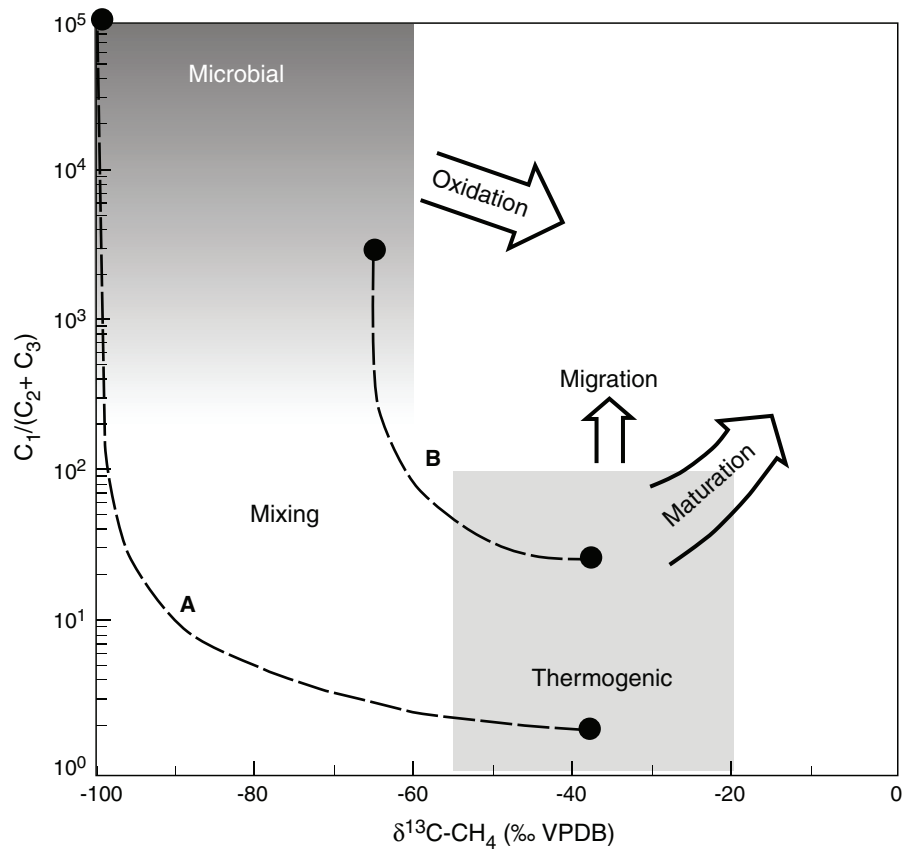


Figure F19. Results of background checks for hydrocarbon gases in drilling mud. The y-axis indicates bit and underreamer depths when the samples were taken from the mud tanks. No background concentrations of propane were detected in the drilling mud.

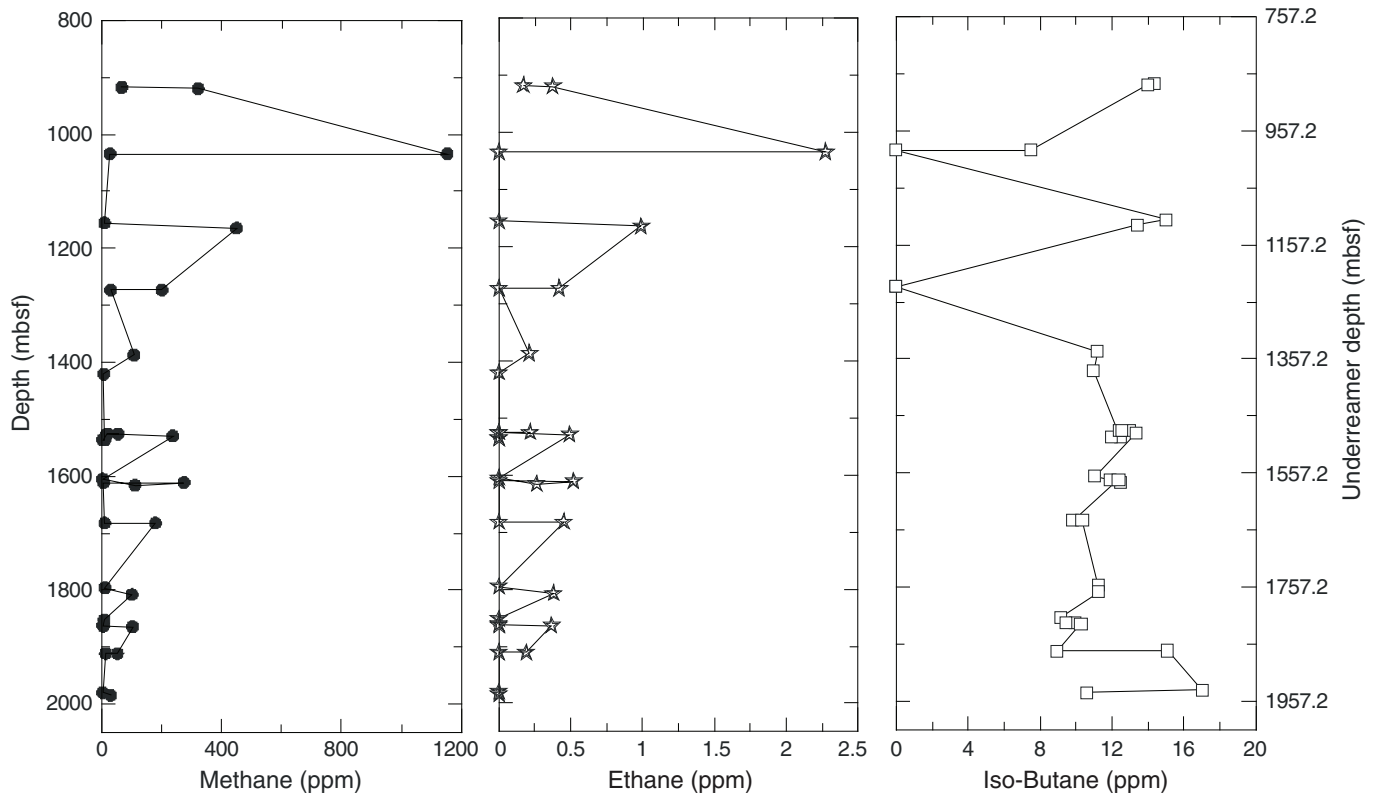


Figure F20. A. Idealized frequency response of dielectric mechanisms with the scale aspects. VHF = very high frequency. B. Water dielectric response and its Cole-Cole plot.

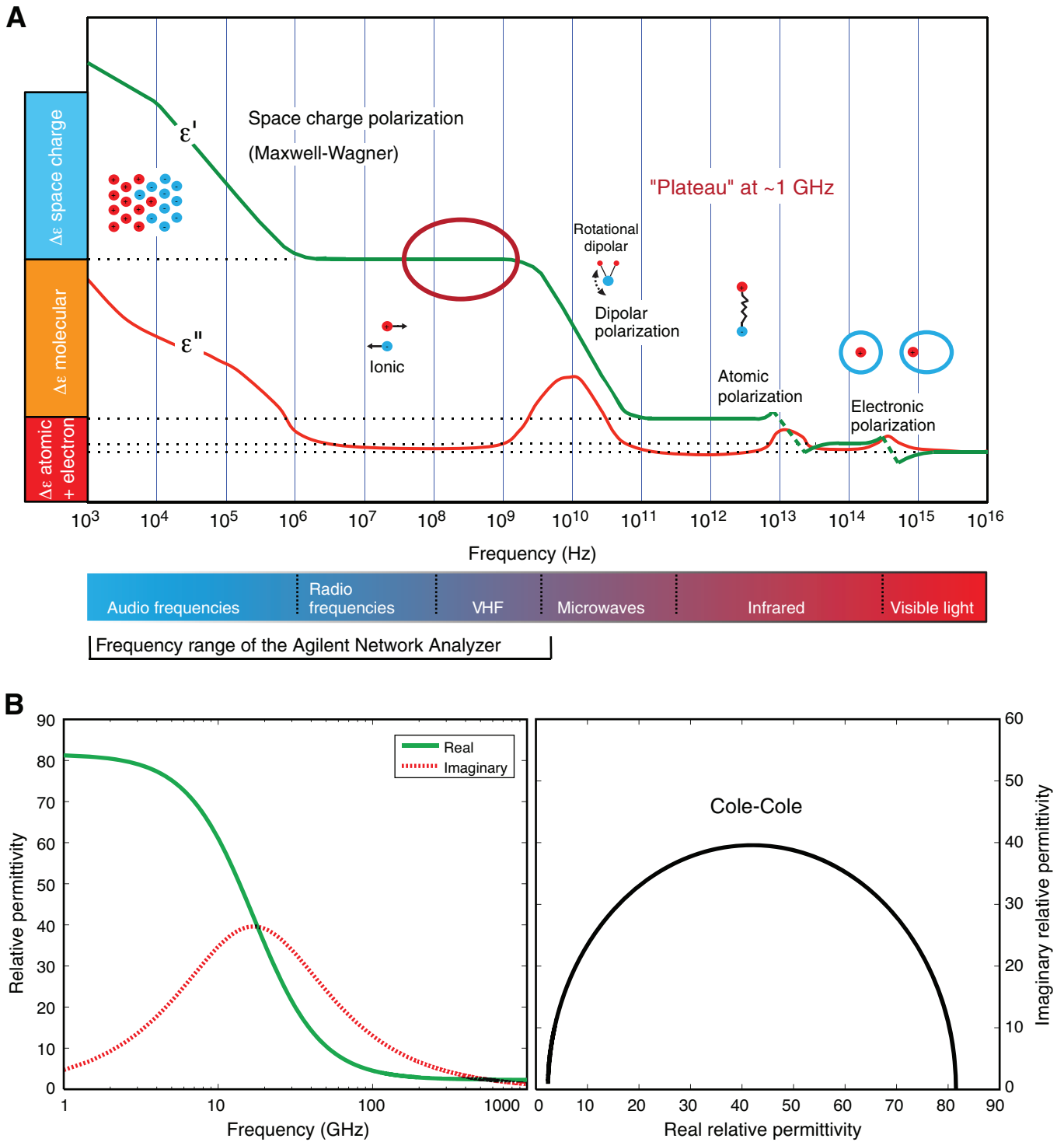


Figure F21. Definition of axis orientation on working-half sections. The z-axis points in the downhole direction of the core and the x-axis is perpendicular to the cuttings surface.

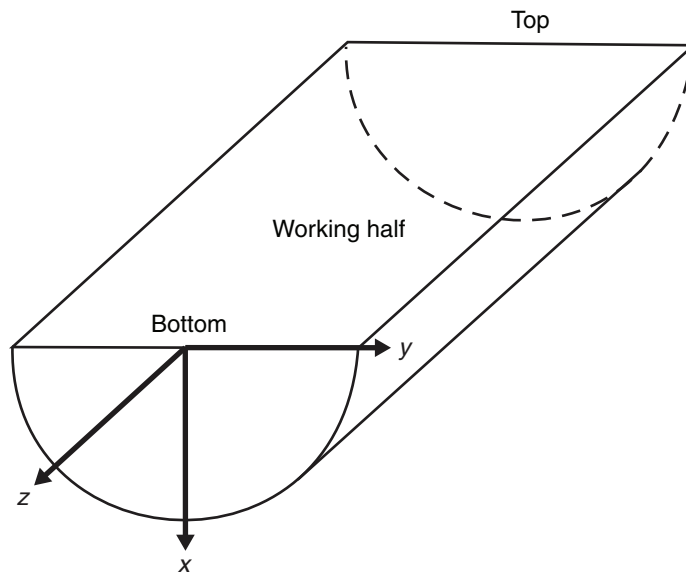


Figure F22. Orientation system used during Expedition 338 and coordinates for superconducting rock magnetometer (modified from Richter et al., 2007). SQUID = superconducting quantum interference device.

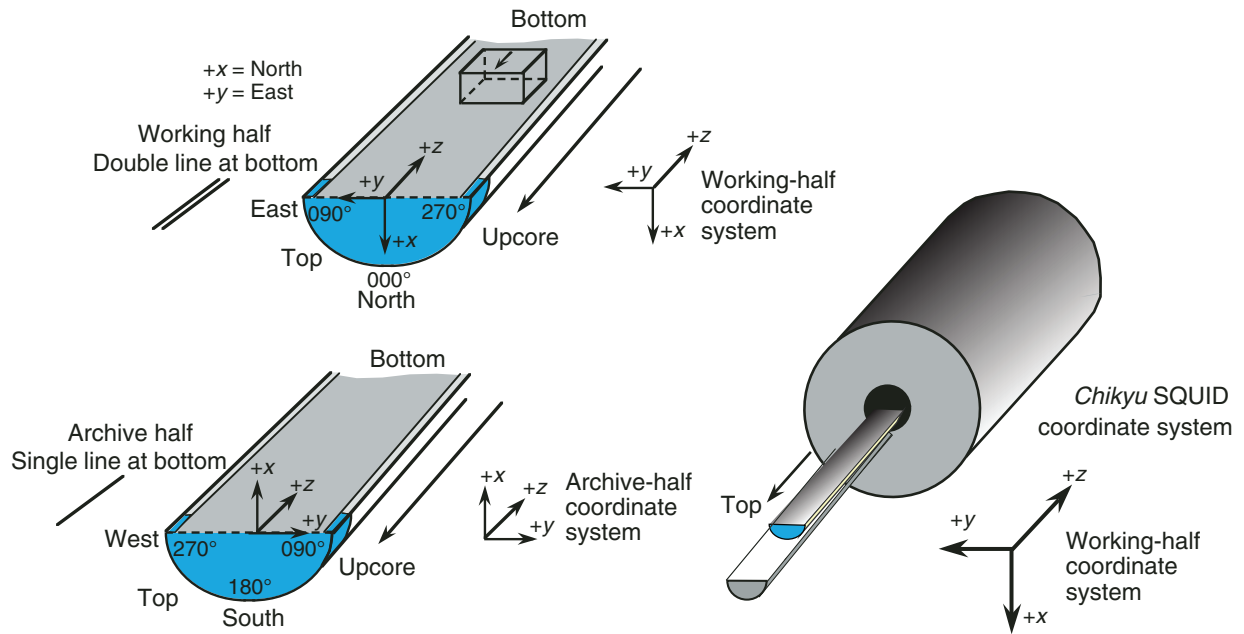


Table T1. Summary of all BHAs from Expedition 338 holes.

Hole	Drilling Type	Water depth (mbsl)	Total depth (mbsf)	Bottom-hole assembly
338-				
C0002F	LWD/MWD	1939.0	2005.5	12-1/4 inch bit × GVR × ARC-8 × TeleScope × 12-1/8 inch ILS × sonicVISION × 12-1/8 inch stab × 8-1/2 inch DC(1) × CST × Anderreamer × float sub × 9-1/2 inch DC(2) × 17 inch stab × 9-1/2 inch DC(1) × XO
C0002H	RCB	1936.5	1120.5	10-5/8 inch RCB core bit × bit sub with 10-5/8 inch stab × RCB core barrel × top sub × head sub × 10-5/8 inch stab × 8-1/2 inch core DC(11) × 8-1/2 inch coring jar × 8-1/2 inch core DC(6) × XO × 5.68 inch HWDP(12) × XO
C0002I	RCB	1936.0	1360.3	10-5/8 inch RCB core bit × bit sub with 10-5/8 inch stab × RCB core barrel × top sub × head sub × 10-5/8 inch stab × 8-1/2 inch core DC(11) × 8-1/2 inch coring jar × 8-1/2 inch DC(6) × XO × 5.68 HWDP(12) × XO × 5 inch DP S-140(42 stds) × 5-1/2 inch DP S-150
C0002J	RCB	1937.5	940.0	10-5/8 inch RCB core bit × bit sub with 10-5/8 inch stab × RCB core barrel × top sub × head sub × 10-5/8 inch coring stab × 8-1/2 inch core DC(11) × XO × 5-1/2 inch DP S-150(12) × XO × 5 inch DP S-140(42 stds) × 5-1/2 inch DP S-150
C0002K	HPCS/EPCS/ ESCS	1937.5	286.5	11-7/16 inch core bit × bit sub × core barrel × landing sub × top sub × head sub × 8-1/2 inch core DC(11) × XO × 5-1/2 inch DP S-150(3 stds) × XO × 5 inch DP S-140(42 stds) × 5-1/2 inch DP S-150
C0002L	ESCS	1937.5	505.0	11-7/16 inch core bit × bit sub × core barrel × landing sub × top sub × head sub × 8-1/2 inch core DC(11) × XO × 5-1/2 inch DP S-150(3 stds) × XO × 5 inch DP S-140(41 stds) × 5-1/2 inch DP S-150
C0012H	LWD/MWD	3509.5	710.0	12-1/4 inch bit × GVR × ARC-8 × TeleScope × 12-1/8 inch ILS × sonicVISION × 12-1/8 inch stab × 8-1/2 inch DC(9) × 7-3/4 inch jar × 8-1/2 inch DC(3) × 5.68 HWDP(12) × 5 inch DP S-140(46 stds) × 5-1/2 inch DP S-150
C0018B	LWD/MWD	3084.5	350.0	12-1/4 inch bit × GVR-8 with 12-1/8 inch stab (with float valve) × ARC-8 × TeleScope 825HF × NM XO sub × NMDC × 12-1/8 inch stab × 8-1/2 inch DC(9) × 7-3/4 inch LI jar × 8-1/2 inch DC(3) × XO × 5-1/2 inch DP S-150(12) × XO × 5 inch DP S-140(42 stds) × XO × 5-1/2 inch DP S-150
C0021A	LWD/MWD	2940.5	294.0	12-1/4 inch bit × GVR-8 with 12-1/8 inch stab (with float valve) × ARC-8 × TeleScope 825HF × NM XO sub × NMDC × 12-1/8 inch stab × 8-1/2 inch DC(9) × 7-3/4 inch LI jar × 8-1/2 inch DC(3) × XO × 5-1/2 inch DP S-150(12) × XO × 5 inch DP S-140(42 stds) × XO × 5-1/2 inch DP S-150
C0021B	HPCS/EPCS	2940.5	194.5	11-7/16 inch core bit × bit sub × core barrel × landing sub × top sub × head sub × 8-1/2 inch DC(11) × XO × 5-1/2 inch DP S-150(12) × 5 inch DP S-140(27 stds) × 5-1/2 inch DP S-150
C0022A	LWD/MWD	2675.5	420.5	12-1/4 inch bit × GVR-8 with 12-1/8 inch stab (with float valve) × ARC-8 × TeleScope 825HF × NM XO sub × NMDC × 12-1/8 inch stab × 8-1/2 inch DC(9) × 7-3/4 inch LI jar × 8-1/2 inch DC(3) × XO × 5-1/2 inch DP S-150(12) × XO × 5 inch DP S-140(42 stds) × XO × 5-1/2 inch DP S-150
C0022B	HPCS/EPCS/ ESCS	2674.0	419.5	11-7/16 inch core bit × bit sub × core barrel × landing sub × top sub × head sub × 7 inch DC(15) × XO × 5-1/2 inch DP S-150(12) × 5 inch DP S-140(42 stds) × 5-1/2 inch DP S-150

LWD = logging while drilling, MWD = measurement while drilling. RCB = rotary core barrel, HPCS = hydraulic piston coring system, EPCS = extended punch coring system, ESCS = extended shoe coring system. GVR = geoVISION resistivity tool, ILS = instrument landing system, CST = concentric string tool. Stab = stabilizer, XO = crossover. DC = drill collar, NMDC = nonmagnetic drill collar. HWDP = heavy weight drill pipe, DP = drill pipe.



Table T2. IODP depth scales summary table.

	Depth scale name	Acronym	Datum	Description	Previous unit	Type depth
Drillers depth scales	Drilling depth below rig floor	DRF	Rig floor	The sum of lengths of all drill string components deployed beneath the rig floor. Includes length of all components and the portions thereof below rig floor.	mbrf	Measured
	Drilling depth below seafloor	DSF	Seafloor	The length of all drill string components between seafloor and target.	mbsf	Processed
LWD and MWD depth scales	LWD depth below rig floor	LRF	Rig floor	The sum of lengths of all drill string components deployed beneath the rig floor reference.	mbrf	Measured
	LWD depth below seafloor	LSF	Seafloor	The length of all drill string components between seafloor and target.	mbsf	Processed
Mud depth scales	Mud depth below rig floor	MRF	Rig floor	The length of all drill string components between where cuttings and gas originate and the rig floor based on lag time of arrival at rig floor and mud pump rate.	NA	Processed
	Mud depth below seafloor	MSF	Seafloor	MRF with seafloor depth below rig floor subtracted.	NA	Processed
Core depth scales	Core depth below seafloor	CSF-A	Seafloor	Distance from seafloor to target within recovered core. Combines DSF to top of cored interval with curated section length to target within cored material. This method allows overlap at cored interval and section boundaries.	mbsf	Processed
	Core depth below seafloor	CSF-B	Seafloor	Distance from seafloor to target within recovered core. Combines DSF to top of cored interval with curated length to target within cored material. This method applies compression algorithm (i.e., scaling) if recovery is >100%.		Processed
Composite depth scales	Core composite depth below seafloor	CCSF	Seafloor	Distance from seafloor to target within recovered core using a scale of adjusted depths constructed to resolve gaps in the core recovery and depth inconsistencies.	mcd	Composite
Seismic depth scales	Seismic depth below seafloor	SSF	Seafloor	Distance below seafloor and target derived from seismic traveltime, velocity, and water depth.	m	Processed
	Seismic depth below sea level	SSL	Sea level	Distance below sea level derived from seismic traveltime and velocity.	m	Processed

LWD = logging while drilling, MWD = measurement while drilling. NA = not applicable. See IODP Depth Scale Terminology at www.iodp.org/program-policies/procedures/guidelines/.

Table T3. LWD/MWD tool acronyms, descriptions, and units. (Continued on next page.)

Tool	Output	Description	Unit
Surface		Drilling parameters	
	BD	Bit depth	m
	TD	Total depth	m
	HKLD	Hook load	kkgf
	SPPA	Surface pump pressure	kkgf
	ROP*5	5 ft averaged rate of penetration	m/h
	SWOB	Surface weight on bit	kkgf
	GRM1	LWD natural gamma radiation	gAPI
	CRPM_RT	Collar rotation	rpm
TRPM_RT	Fluid pulse turbine rotation	rpm	
MWD		Measurement while drilling	
	RGX	Rotating axial accelerometer	rpm
	RHX	Rotating axial magnetometer	rpm
	A_JAM	Antijam counter	
	TUR_RPM	Turbine rotation	rpm
	SHOCK	Shock counter	
	CRPMS	Average MWD collar rotation	rpm
	STICKNSLIP	Peak-to-peak collar rotation	rpm
	MTF/GTF	Magnetic/gravity toolface	
	LTBRT	LTB retries counter	
	MWDSTAT	Tool status word	
	DL_TEMP	Direction and inclination sensor temperature	°C
	TOTALSHOCK	Total shocks	
	CUREDRT	Current equivalent drilling time	
arcVISION real time/APWD		Annular pressure while drilling/Array resistivity tool	
	APRS_c	Annular pressure	kPa
	ATEMP_c	Annular temperature	°C
	SHKLV_c	Shock level	
	ARC6STAT	Tool status word	
	PESD_c	Hydrostatic pressure during pump off	
	ESDT_c	Time stamp for PESD	
	PMIN_c	Minimum pressure during pump off	
	PMIT_c	Time stamp for PMIN	
	PMAX_c	Maximum pressure during pump off	
PMAT_c	Time stamp for PMAX		
arcVISION memory		Array resistivity tool	
	DHAP	Downhole annular pressure	kPa
	DHAT	Downhole annular temperature	°C
	ECD	Equivalent circulating density	g/cm ³
sonicVISION real time		Sonic while drilling tool	
	DTCO_s	Δt compressional slowness	$\mu\text{s}/\text{ft}$
	CHCO_s	Sonic compressional semblance	
	C_PEAK3_s	First 3 peak array with Δt , coherence, and traveltimes	
	SONSK_s	Shock risk	
sonicVISION memory		Sonic while drilling tool	
	SPWi	Receiver_i spectrum array	—
	Wfi	Filtered waveform_i, 1/2 ft averaged	
	WfiT	Filtered waveform_i, 2 inch averaged	
	DTTA	Δt compressional from transmitter array	$\mu\text{s}/\text{ft}$
	DTBC	Δt compressional borehole compensated	$\mu\text{s}/\text{ft}$
	DTDF	Δt compressional difference between DTRA and DTTA	$\mu\text{s}/\text{ft}$
	CHRA	Coherence at compressional peak; receiver array	—
	CHTA	Coherence at compressional peak; transmitter array	—
	TTRA	Transit time at compressional peak; receiver array	μs
	TTTA	Transit time at compressional peak; transmitter array	μs
	ITTI	Integrated transit time	ms
	DTCO	Δt compressional after processing	$\mu\text{s}/\text{ft}$
geoVISION real time		geoVISION resistivity tool	
	GRRA_r	Natural gamma radiation average	gAPI
	RING_r	Ring resistivity	
	RBIT_r	Resistivity at bit	Ωm
	RSBA_r	Shallow button resistivity average	Ωm
	RMBA_r	Medium button resistivity average	Ωm
	RDBA_r	Deep button resistivity average	Ωm
	SHKT_r	Transverse shock	
	SHKA_r	Axial shocks	
RABSTAT	Tool status word		

Table T3 (continued).

Tool	Output	Description	Unit
geoVISION memory		geoVISION resistivity tool	
	GR	Total natural gamma radiation	gAPI
	GR_IMG	Total natural gamma radiation image	gAPI
	RES_RING	Ring resistivity	Ωm
	RES_BIT	Bit resistivity	Ωm
	RES_BS	Shallow button resistivity	Ωm
	RES_BM	Medium button resistivity	Ωm
	RES_BD	Deep button resistivity	Ωm
	RES_BS_IMG	Shallow button resistivity image	Ωm
	RES_BM_IMG	Medium button resistivity image	Ωm
	RES_BD_IMG	Deep button resistivity image	Ωm
	TAB_RAB_BS	Shallow button resistivity time after bit	s
	TAB_RAB_BM	Medium button resistivity time after bit	s
	TAB_RAB_BD	Deep button resistivity time after bit	s
	AZIM	Measured azimuth from well survey	$^{\circ}$
	P1AZ	Pad 1 azimuth in horizontal plane (0 = true north)	$^{\circ}$
	P1NO	Pad 1 azimuth in horizontal orthogonal to tool axis (0 = true north)	$^{\circ}$
	ROP5	Rate of penetration averaged over the last 5 ft (1.5 m)	$^{\circ}$
	P1NO	Pad 1 rotation relative to north azimuth	$^{\circ}$
	TAB_GR	Gamma ray time after bit	h
	TAB_RES_BIT	Bit resistivity time after bit	h
	TAB_RES_RING	Ring resistivity time after bit	h
	TAB_RES_BS	Shallow button resistivity time after bit	h
	TAB_RES_BM	Medium button resistivity time after bit	h
	TAB_RES_BD	Deep button resistivity time after bit	h
	RPM	Rotational speed	rpm
	SHKL_AXL	Axial shock level	
	SHKL_RAD	Radial shock level	

LWD = logging while drilling, MWD = measurement while drilling. Receiver $i = 1, 2, 3, \text{ or } 4$.

**Table T4.** Measurement performance specifications of the geoVISION tool.

Measurement	Vertical resolution (inch)	Depth of investigation (inch)	Diameter of investigation (inch)		Horizontal resolution (inch)		Midpoints of extremes (inch)
			$R_t/R_{xo} = 10$	$R_t/R_{xo} = 0.1$	$R_t/R_{xo} = (10 \times \pi)/56$	$R_t/R_{xo} = (0.1 \times \pi)/56$	
Resistivity at the bit	12–24	12	32	32			
Ring resistivity	2–3	7	22	25			
Button resistivity							
Shallow focused	2–3	1	19	24	1.07	1.35	1.2
Medium focused	2–3	3	15	21	0.84	1.18	1
Deep focused	2–3	5	11	16	0.62	0.9	0.75
Gamma ray	12	10					

R_t = true resistivity of formation. R_{xo} = resistivity of zone invaded by drilling fluid. Invasion may be minimal due to measurement of resistivity soon after cutting of hole. Then $R_t/R_{xo} = 1$. Horizontal resolution for each of tools intermediate between extremes of R_t/R_{xo} in table above. Imaging tools record 56 times with each revolution of the tool. Accuracy of segment location is $\pm 1^\circ$.

Table T5. Measurement performance specifications of the sonicVISION tool.

Specification	Unit	Value
Slowness	μs/ft	40–170 (water-based mud) 40–200 (oil-based mud) 40–230 (synthetic oil-based mud)
Accuracy	μs/ft	±2
Acoustic aperture	ft	2
Transmitter to midpoint of receiver array	ft	11

Table T6. Classification of volcanic lithologies, Expedition 338.

Size fraction	Mixture		
	Tephra	Volcaniclastic deposits	Epiclastic deposits
>64 mm	Pyroclastic breccia	Volcaniclastic breccia/Conglomerate	Breccia/Conglomerate
2–64 mm	Lapillstone/Lapili tuff	Volcaniclastic gravel	Gravel
64 μm–2 mm	Coarse ash/Tuff	Volcaniclastic sandstone	Sandstone
2–64 μm	Fine ash/Tuff	Volcaniclastic siltstone	Siltstone
<2 μm	Volcanic dust	Volcaniclastic volcanic dust	Claystone
Amount of pyroclasts	≥75%	<75% to >25%	≤25%

Modified after Fisher and Schmincke (1984). If >25% of volcaniclasts are vitric pyroclasts, then material is tuffaceous.

Table T7. Characteristic X-ray diffraction peaks for semiquantitative area analysis, Expedition 338.

Mineral	Reflection	d-Value (Å)	Peak position (°2θ)
Composite clay	Multiple	4.478	19.4–20.4
Quartz	101	3.342	26.3–27.0
Feldspar	002	3.192	27.4–28.2
Calcite	104	3.035	29.1–29.7

Table T8. Normalization factors for calculation of relative mineral abundance using bulk powder X-ray diffraction analysis, Expedition 338.

Affected mineral in standard mixture	Normalization factor			
	Total clay minerals	Quartz	Feldspar	Calcite
Influencing mineral:				
Total clay minerals	0.11006193E-01	-0.20231483E-03	-0.29246596E-03	-0.11871842E-02
Quartz	-0.14089397E-04	0.58841606E-03	-0.24897352E-04	-0.23400669E-04
Feldspar	0.49289758E-03	-0.71762974E-04	0.11238736E-02	-0.41371561E-04
Calcite	0.56265158E-04	-0.41641979E-05	-0.50802228E-05	0.13876300E-02

Singular value decomposition was used to compute factors, following Fisher and Underwood (1995).

Table T9. Analytical conditions for major element analysis of glass beads on the Supermini (Rigaku) XRF spectrometer, Expedition 338.

Element line	Filter	Crystal	Peak angle (°)	Count time (s)	BG 1 angle (°)	Count time (s)	BG 2 angle (°)	Count time (s)	Detector
Na-K α	Out	RX25	47.125	40	49.000	10	45.250	10	PC
Mg-K α	Out	RX25	38.804	40	40.750	10	36.900	10	PC
Al-K α	Out	PET	144.607	40	147.150	10	140.400	10	PC
Si-K α	Out	PET	108.946	40	106.100	10	111.250	10	PC
P-K α	Out	PET	89.280	40	91.350	10	87.200	10	PC
K-K α	A 140	PET	50.632	40	49.200	10			PC
Ca-K α	Out	PET	45.154	40	43.650	10			PC
Ti-K α	Out	LiF1	86.155	20	85.240	10	87.120	10	SC
Mn-K α	Out	LiF1	62.997	20	62.200	10	63.820	10	SC
Fe-K α	Out	LiF1	57.535	20	58.180	10	56.900	10	SC

BG = background. PC = flow-proportioned counter, SC = scintillation counter.

Table T10. Average measured values and 3σ for major elements, Expedition 338.

Component	Standard Sample JB-3				Standard Sample JA-1			
	Reference value (100% normalized)	Measured value (average)	Standard deviation (3σ)	Relative standard deviation (%)	Reference value (100% normalized)	Measured value (average)	Standard deviation (3σ)	Relative standard deviation (%)
Na ₂ O	2.720	2.713	0.106	1.3	3.867	3.821	0.155	1.4
MgO	5.170	5.109	0.085	0.6	1.581	1.541	0.097	2.1
Al ₂ O ₃	17.135	17.173	0.08	0.2	15.325	15.300	0.092	0.2
SiO ₂	50.767	50.842	0.141	0.1	64.413	64.342	0.227	0.1
P ₂ O ₅	0.293	0.286	0.014	1.6	0.166	0.144	0.012	2.7
K ₂ O	0.777	0.764	0.02	0.9	0.775	0.783	0.034	1.5
CaO	9.753	9.789	0.049	0.2	5.739	5.691	0.031	0.2
TiO ₂	1.435	1.432	0.032	0.7	0.856	0.855	0.025	1.0
MnO	0.176	0.184	0.005	0.9	0.158	0.159	0.006	1.2
Fe ₂ O ₃	11.775	11.810	0.065	0.2	7.119	7.077	0.062	0.3

Values determined on the Supermini (Rigaku) X-ray fluorescence spectrometer from a selection of standard samples.

Table T11. Astronomically calibrated age estimates of calcareous nannofossil datums used as biostratigraphic tie points, Expedition 338. (Continued on next page.)

Nannofossil event	Zone (base)	Degree of reliability	Age (Ma)
X medium <i>Gephyrocapsa</i> (>3.5 µm)– <i>Emiliana huxleyi</i>			0.082–0.063
FO <i>Emiliana huxleyi</i>	NN21	B	0.291
LO <i>Pseudoemiliana lacunosa</i>	NN20	A	0.436
LCO <i>Reticulofenestra asanoi</i>		A	0.903–0.901*
RE medium <i>Gephyrocapsa</i> (≥4 µm) + FO <i>Gephyrocapsa</i> sp. 3 (<i>G. parallela</i>)		A	1.04
FCO <i>Reticulofenestra asanoi</i>		D	1.136–1.078*
LO large <i>Gephyrocapsa</i> (>5.5 µm)		A	1.24
LO <i>Helicosphaera sellii</i>		C	1.34
FCO large <i>Gephyrocapsa</i> (>5.5 µm)			1.46
FO large <i>Gephyrocapsa</i> (>5.5 µm)		B	1.560–1.617*
LO <i>Calcidiscus macintyrei</i> (≥11 µm)		C	1.6
FO medium <i>Gephyrocapsa</i> (>3.5 µm)		A	1.67
LO <i>Discoaster brouweri</i>	NN19	A	2.06
AB <i>Discoaster triradiatus</i>		A	2.135–2.216*
LO <i>Discoaster pentaradiatus</i>	NN18	C	2.393–2.512*
LO <i>Discoaster surculus</i>	NN17	C	2.52
LO <i>Discoaster tamalis</i>		C	2.87
LO <i>Sphenolithus</i> spp.		C	3.65
LO <i>Reticulofenestra pseudoumbilicus</i> (>7 µm)	NN16	A	3.79
FCO <i>Discoaster asymmetricus</i>	NN15–NN14	B	4.13
LO <i>Amaurolithus primus</i>			4.5
LO <i>Ceratolithus acutus</i>		B	5.04
FO <i>Ceratolithus rugosus</i>	NN13	D	5.12
LO <i>Triquetrorhabdulus rugosus</i>			5.279*
FO <i>Ceratolithus acutus</i>		B	5.32
LO <i>Discoaster quinquenarius</i>	NN12	A	5.59
LO <i>Nicklithus amplificus</i>		A	5.978–5.939*
FO <i>Nicklithus amplificus</i>		C	6.909–6.684*
PE <i>Reticulofenestra pseudoumbilicus</i> (>7 µm)		D	7.077–7.167*
FO <i>Amaurolithus</i> spp./ <i>Amaurolithus primus</i>	NN11b	A	7.362–7.424*
FCO <i>Discoaster surculus</i>		B	7.88
LCO <i>Minylitha convallis</i>		D	7.78–8.3
FO <i>Discoaster berggrenii</i>	NN11a	D	8.52
PB <i>Reticulofenestra pseudoumbilicus</i> (>7 µm)	NN10b	A	8.785–8.761*
FO <i>Discoaster pentaradiatus</i>			9.1
FO <i>Minylitha convallis</i>		D	9.416
LO <i>Discoaster hamatus</i>	NN10a	C	9.56
LO <i>Catinaster calyculus</i>		D	9.674*
LO <i>Catinaster coalitus</i>		D	9.687*
X <i>Discoaster hamatus</i> – <i>D. neohamatus</i>			9.762*
FO <i>Discoaster neohamatus</i>		C	9.867–10.521*
LCO <i>Discoaster exilis</i>			10.427
FO <i>Discoaster hamatus</i>	NN9	C	10.541
LO <i>Coccolithus miopelagicus</i>		C	10.613
FO <i>Discoaster calcaris</i>			10.676
FO <i>Discoaster bellus</i> gr.		C	10.72
FO <i>Discoaster brouweri</i>		A	10.734–10.764*
FO <i>Catinaster calyculus</i>		D	10.785*
FO <i>Catinaster coalitus</i>	NN8	D	10.886–10.733*
LCO <i>Discoaster kugleri</i>		A	11.578–11.596*
FCO <i>Discoaster kugleri</i>	NN7	B	11.863–11.905*
LO <i>Cyclicargolithus floridanus</i>		D	12.037
LO <i>Coronocyclus nitescens</i>			12.254
LCO <i>Calcidiscus premacintyrei</i>		A	12.447
FCO <i>Triquetrorhabdulus rugosus</i>			12.671
LCO <i>Cyclicargolithus floridanus</i>		A	13.294
LO <i>Sphenolithus heteromorphus</i>	NN6	C	13.532–13.654*
LO <i>Helicosphaera ampliapertura</i>	NN5		14.914*
AE <i>Discoaster deflandrei</i>			15.663*
FO <i>Discoaster signus</i>			15.702*
FCO <i>Sphenolithus heteromorphus</i>			17.721*
LCO <i>Sphenolithus belemnus</i>	NN4		17.973*
LO <i>Triquetrorhabdulus carinatus</i>		D	18.315*
FO <i>Sphenolithus belemnus</i>	NN3		18.921*
FO <i>Helicosphaera ampliapertura</i>			20.393*
X <i>Helicosphaera euphratis</i> – <i>Helicosphaera carteri</i>			20.894*
FCO <i>Helicosphaera carteri</i>			21.985*

Table T11 continued.

Nannofossil event	Zone (base)	Degree of reliability	Age (Ma)
LCO <i>Triquetrorhabdulus carinatus</i>			22.092
FO <i>Sphenolithus disbelemnos</i>		C	22.413
FO <i>Discoaster druggii</i>	NN2	D	22.824*
LO <i>Sphenolithus delphix</i>		A	23.089
FO <i>Sphenolithus delphix</i>		A	23.356
LO <i>Sphenolithus ciperoensis</i>	NN1	C	24.389

Datums are based on Pacific records if not otherwise stated. * = datums based on Atlantic or Mediterranean records. Age estimates adopted from Raffi et al. (2006). X = abundance crossover, FO = first occurrence, LO = last occurrence, LCO = last consistent occurrence, RE = reentrance, FCO = first consistent occurrence, AB = acme beginning, AE = acme end, PE = paracme end, PB = paracme beginning. Degree of reliability: A = distinct, well defined, and isochronous worldwide; B = indistinct and less well defined but reasonably isochronous; C = distinct and well defined but diachronous; D = indistinct, poorly defined, and diachronous. See Raffi et al. (2006) for detailed explanation.

Table T12. Planktonic foraminiferal datum events, Expedition 338.

Event	Zone (base)	Age (Ma)
LO <i>Globigerinoides ruber rosa</i>		0.12
LO <i>Truncorotalia tosaensis</i>		0.61
FO <i>Truncorotalia crassaformis hessi</i>		0.8
LO <i>Globoturborotalita obliquus</i>		1.3
SD2 <i>Pulleniatina</i> spp.		1.7–1.8
LO <i>Neogloboquadrina asanoi</i>		1.8
FO <i>Truncorotalia truncatulinoides</i>	N.22	1.93
FO <i>Pulleniatina finalis</i>		2.04
FO <i>Globoconella inflata</i> modern form		2.3–2.5
FO <i>Truncorotalia tosaensis</i>	N.21	3.35
LO <i>Dentoglobigerina altispira altispira</i>		3.47
LO <i>Sphaeroidinellopsis seminulina</i>		3.59
LO <i>Hirsutella margaritae</i>		3.85
SD1 <i>Pulleniatina</i> spp.		4.08
FO <i>Truncorotalia crassaformis</i>		4.31
LO <i>Globoturborotalita nepenthes</i>		4.37
FO <i>Globorotalia tumida</i>	N.18	5.57
FO <i>Globigerinoides conglobatus</i>		6.2
FO <i>Pulleniatina primalis</i>	N.17b	6.6
FO <i>Globorotalia plesiotumida</i>	N.17a	8.58
LO <i>Globoquadrina dehiscens</i>		8.5–9.4
FCO <i>Neogloboquadrina acostaensis</i>	N.16	10.57
LO <i>Paragloborotalia mayeri</i>	N.15	11.47
LO <i>Globigerinoides subquadratus</i>		11.54
FO <i>Globoturborotalita nepenthes</i>	N.14	11.63
FO <i>Fohsella lobata</i>	N.12	12.53
FO <i>Fohsella praefohsi</i>	N.11	12.76
FO <i>Fohsella peripheroacuta</i>	N.10	14.24
LO <i>Praeorbulina sicana</i>		14.53
FO <i>Orbulina universa</i>	N.9	14.74
FO <i>Praeorbulina sicana</i>	N.8	16.97
LO <i>Catapsydrax dissimilis</i>	N.7	17.54
FO <i>Globigerinatella insueta</i>	N.6	17.59
LO <i>Paragloborotalia kugleri</i>	N.5	21.12
FO <i>Paragloborotalia kugleri</i>	N.4	22.96

FO = first occurrence, FCO = first consistent occurrence, LO = last occurrence, SD = change in coiling direction from sinistral to dextral.

Table T13. Background concentrations of drilling mud water, Expedition 338.

Sample	Depth (mbsf)		IC (wt%)	CaCO ₃ (wt%)	TN (wt%)	TC (wt%)	TOC (wt%)	C/N	Remarks
	Top	Bottom							
5-LMT	NA	NA	0.32	2.70	0.04	17.33	17.00	440.2	
10-LMW	875.5	880.5	0.34	2.84	0.04	16.74	16.40	442.2	
147-LMW	1495.5	1500.5	0.31	2.57	0.03	14.58	14.27	429.6	
152-LMT	NA	NA	0.32	2.63	0.03	14.80	14.49	434.3	
179-LMT	NA	NA	0.32	2.69	0.04	14.51	14.18	401.9	
185-LMW	1600.5	1605.5	0.30	2.48	0.03	13.95	13.65	437.9	
Unnamed	1700.5	1700.5	0.30	2.52	0.04	13.97	13.67	378.4	102 written on bottle, sample is not registered to J-CORES
Unnamed	1717.5	1717.5	0.30	2.53	0.03	13.95	13.65	432.0	102 written on bottle, sample is not registered to J-CORES

NA = not applicable. IC = inorganic carbon, TN = total nitrogen, TC = total carbon, TOC = total organic carbon.

Table T14. Ages used for geomagnetic polarity timescale, Expedition 338.

Interval (Ma)		Chron/Subchron
Top	Bottom	
0	0.781	C1n
0.988	1.072	C1r.1n
1.173	1.185	C1r.2n
1.778	1.945	C2n
2.581	3.032	C2An.1n
3.116	3.207	C2An.2n
3.33	3.596	C2An.3n
4.187	4.3	C3n.1n
4.493	4.631	C3n.2n
4.799	4.896	C3n.3n
4.997	5.235	C3n.4n
6.033	6.252	C3An.1n
6.436	6.733	C3An.2n
7.14	7.212	C3Bn
7.251	7.285	C3Br.1n
7.454	7.489	C3Br.2n
7.528	7.642	C4n.1n
7.695	8.108	C4n.2n
8.254	8.3	C4r.1n
8.769	9.098	C4An
9.321	9.409	C4Ar.1n
9.656	9.717	C4Ar.2n
9.779	9.934	C5n.1n
9.987	11.04	C5n.2n
11.118	11.154	C5r.1n
11.554	11.614	C5r.2n
12.041	12.116	C5An.1n
12.207	12.415	C5An.2n
12.73	12.765	C5Ar.1n
12.82	12.878	C5Ar.2n
13.015	13.183	C5AAn
13.369	13.605	C5ABn
13.734	14.095	C5ACn
14.194	14.581	C5ADn
14.784	14.877	C5Bn.1n
15.032	15.16	C5Bn.2n
15.974	16.268	C5Cn.1n
16.303	16.472	C5Cn.2n
16.543	16.721	C5Cn.3n
17.235	17.533	C5Dn
18.056	18.524	C5En
18.748	19.722	C6n
20.04	20.213	C6An.1n
20.439	20.709	C6An.2n
21.083	21.159	C6AAn
21.659	21.688	C6AAr.2n
21.767	21.936	C6Bn.1n
21.992	22.268	C6Bn.2n
22.564	22.758	C6Cn.1n
22.902	23.03	C6Cn.2n

Data from Lourens et al., 2004.

Appendix A

Evaluation of GRIND and leaching methods for extracting interstitial water as an alternative to the standard squeezing method

An alternate method of pore water extraction from sediment with porosity <40% was used during Expedition 315. This method was initially developed by Cranston (1991) and later used by Wheat et al. (1994) to assess pore fluid composition under conditions where it was impossible to extract a sufficient volume of interstitial water by the standard squeezing method for chemical analysis (Expedition 315 Scientists, 2009a). In this method, an appropriate aliquot of indium standard solution is added to the sediment and ground in a ball mill to dilute the interstitial water. Because the water volume increases, the mixture of interstitial water and added standard solution is easier to squeeze from the sediment-fluid mixture than from the intact sediment. During Expedition 338, Hole C0002H planned to drill through the accretionary prism, which is older than 5.6 Ma (see “[Biostratigraphy](#)” in the “Site C0002” chapter [Strasser et al., 2014b]). These sediments were expected to have low porosity and permeability. Thus, the GRIND method would be more suitable to extract interstitial water instead of the standard squeezing method.

Before applying this method, the chemical analyses of interstitial water by the standard squeezing and GRIND methods were compared. The validity of the use of In- and rare earth element (REE)-spiked samples was checked to estimate the dilution of interstitial water by the additional water. A leaching test was also conducted to simplify the extraction procedure of soluble salts from interstitial water. Here, the results of these methods are described and compared.

Experiment 1: extraction methods

Eight different methods of extracting interstitial water from whole rounds are compared:

1. Standard squeezing (Method 1-A)
2. Previously developed GRIND method
 - a. Spike with In standard (Method 2-A)
 - b. Spike with Lu standard (Method 2-B)
3. Leaching method
 - a. Dry sample leaching (Method 3-A)
 1. Dry in air at 105°C (Method 3-A1)
 2. Dry in a vacuum chamber (Method 3-A2)
 - b. Wet sample leaching (Method 3-B)
 1. Adding Milli-Q water (Method 3-B1)
 2. Adding 20 μM $\text{CH}_3\text{COONH}_4$ solution (Method 3-B2)

3. Adding 100 μM $\text{CH}_3\text{COONH}_4$ solution (Method 3-B3)

Standard squeezing (Method 1-A)

The standard squeezing method for extracting interstitial water from whole-round core samples is described in “[Geochemistry](#).”

Previously developed GRIND method

GRIND Method 2-A. A 5 mL aliquot of Milli-Q water spiked with a 500 ppb In standard is added to 40 g of sediment, which is then ground in a ball mill. The sediment-water sample is squeezed using the conventional squeezing method to produce a spiked sample of interstitial fluid.

GRIND Method 2-B. A 5 mL aliquot of Milli-Q water spiked with a 500 ppb Lu standard is added to 40 g of sediment, which is then ground in a ball mill. The sediment-water sample is squeezed using the conventional squeezing method to produce a spiked sample of interstitial fluid.

Leaching method

The sample sediment is suspended in a centrifuge tube to dissolve the soluble salts. The combination of sample treatment and solutions are listed in Table [AT1](#). The following sections describe the processes for each leaching treatment.

Leaching Method 3-A. The sediment is dried in a convection oven at 105°C overnight (same as that for MAD analysis) (Method 3-A1) or dried in a vacuum oven (Method 3-A2). The latter was conducted to evaluate the effect of oxidation during drying in air. A 4 g (weighed accurately) aliquot of the dried sample is powdered and suspended in 40 mL Milli-Q water (weighed or volume measured accurately) in a centrifuge tube by hand shaking.

Leaching Method 3-B. Sediment is suspended without any treatment after being roughly crushed, placed in a centrifuge tube, and added to 40 mL of leachate. Leachates tested are as follows:

1. 40 mL Milli-Q water (Method 3-B1),
2. 40 mL of 20 μM $\text{CH}_3\text{COONH}_4$ (ammonium acetate) solution (Method 3-B2), and
3. 40 mL of 100 μM $\text{CH}_3\text{COONH}_4$ solution (Method 3-B3).

The centrifuge tube is shaken for 1 min using a tube mixer to mix the sediment and solution well and dissolve the soluble salts. After shaking the mixtures of sediment and solution, the tube is centrifuged at 10,000 rpm for 10 min to separate the solids and solution. After separating the solids and solution by centrifugation, the solution is stored in two plastic bottles until analysis; an appropriate amount of HCl

is added to one of the bottles to dissolve redox-sensitive metal ions. If the water content of sediment is ~20%, the interstitial water is diluted 50 times.

Analytical procedures

Chemical analysis of the liquid. Analytical procedures to quantify the dissolved elements follow those routinely applied in the geochemistry laboratory on board the *Chikyu* (see “[Geochemistry](#)”). All the extracted water samples were filtered through a 0.45 μm filter and stored in two plastic bottles; HCl was added to one of those bottles to a concentration of 0.01 M HCl. Just after the sample solution was stored in the plastic bottles, pH was measured using a glass electrode, and alkalinity was determined by titration using the same electrode. Chlorinity was determined by titration. The other major anions (Br^- and SO_4^{2-}) and cations (Na^+ , K^+ , Ca^{2+} , and Mg^{2+}) were analyzed by ion chromatography using anion and cation exchange columns, respectively. Nutrients PO_4^{3-} and NH_4^+ were analyzed by colorimetry. Minor elements B, Si, Fe, Li, Mn, Ba, and Sr were analyzed by ICP-AES. Trace metals V, Cu, Zn, Rb, Mo, Sc, Pb, and U were analyzed by ICP-MS. Indium (In), Y, and Lu were analyzed by ICP-MS only for the spiked samples and squeezed using Method 1-A as a reference (Table [AT2](#)).

Calculation of dilution ratio. The dilution ratio can be obtained by

$$R = (\text{water weight in the sediment} + \text{weight of added solution}) / (\text{water weight in the sediment}). \quad (43)$$

Densities of the added solution were close to 1, and the volume (mL) was assumed to be the same as weight (g). The water weight in the sediment is determined by

$$\frac{\text{wet sediment weight (g)} \times \text{water content (fraction)}}{\text{water weight in the sediment (g)}} = \quad (44)$$

The water content was measured by drying sediment in a convection oven at 105°C in the same manner as water content analyses routinely operated on board for MAD analyses and in a vacuum chamber.

Results

The water content determined by the two different ways of drying was almost the same (Table [AT3](#)). Thus, the sample used for the second experiment was dried in a convection oven at 105°C for determination of water content as usual.

The results of chemical analyses are shown in Table [AT4](#) and Figures [AF1](#), [AF2](#), and [AF3](#). The extracted solutions by the GRIND method give, in general, comparable values to those by the standard squeezing method. Among the major elements, chlorinity is in good agreement (within 5% error). Na^+ and Mg^{2+} concentrations are also within the range of 5% error, which is acceptable for major element analysis. SO_4^{2-} and Ca^{2+} concentrations of the extracted solution by the GRIND method are larger and Br^- is smaller than those by the standard squeezing method, but SO_4^{2-} , Ca^{2+} , and Br^- concentrations are within the range of 10% error. Among the minor and trace elements, both GRIND and standard squeezing methods give consistent values for NH_4^+ , B, and Sr within 5%–10% error. The concentrations of other elements determined by the GRIND method are not useful when compared to those by the standard squeezing method. The extracting solution in Method 2-A included an In standard and the solution in Method 2-B included Lu. Analytical results of these elements together with Y are listed in Table [AT2](#), which indicates that those elements were almost completely lost from the extracted solutions. This is probably because those elements were adsorbed onto mineral surfaces, especially onto clay minerals, during grinding. Thus, it is clear that the spikes are not a valuable addition to the solution before extraction. As described above, the dilution rate can be calculated from the water volume in sediment and added solution. Thus, it is not necessary to add elemental spikes to solutions prior to the extraction procedure.

Solutions prepared using the leaching method generally showed large variations. The anion concentrations of leaching solutions from dried sediment (Methods 3-A1 and 3-A2) give much higher values than those of the standard squeezed water. Alkaline element concentrations are much higher in the solutions prepared using the dried sediment, except Li. Mg and Sr concentrations of those solutions are much lower, whereas Ba in those solutions are much higher than those from the standard squeezed water. Ca concentration is comparable to that of standard squeezed water. Leaching solution from wet sediment (Methods 3-B1, 3-B2, and 3-B3) generally contained lower concentrations of major anions and cations and much higher concentrations of minor and trace elements. The concentrations of trace elements V, Mo, Cu, Zn, and U, especially, are more than three orders of magnitude higher than those in the standard squeezed water. Such differences must be attributed to the strong adsorbability of those elements onto the mineral surface; those are released into the solution when the water/sediment ratio becomes

high. Therefore, the leaching method is not suitable to extract dissolved elements because the solution condition drastically changes from the original interstitial water, which largely modifies the chemical composition.

Conclusion

Indium and REE used as spikes for determining dilution ratios are adsorbed onto mineral surfaces during grinding, so it is better to use water content for the determination of dilution ratios. In the leaching method, leachates drastically changed the solution condition from the original interstitial water, so this method is not suitable for extraction of dissolved elements from sediment.

Experiment 2: comparison of extracting solutions in the GRIND method

As described in “[Experiment 1: extraction methods](#),” the spiked elements were not detected or mostly lost in the extracted water. Thus, the chemical condition of the extraction solution was checked in an additional test. An 80 g sediment sample was ground with 10 g of the following solutions:

1. Milli-Q water (Method 2-C),
2. 100 μM $\text{CH}_3\text{COONH}_4$ (ammonium acetate) solution (Method 2-D),
3. Diluted HNO_3 solution with pH adjusted to 3 (Method 2-E), and
4. Diluted HNO_3 solution with pH adjusted to 5 (Method 2-F).

The weights of sediment and solution were twice those used in the previous studies. The extracting water was prepared using Milli-Q water flushed with N_2 for >48 h to remove dissolved oxygen. After addition of the extracting solution, interstitial water was extracted using the standard squeezing method (Method 1-B).

Results

Analytical results are given in Table [AT4](#) and Figures [AF4](#), [AF5](#), and [AF6](#). Chlorinity obtained using the GRIND method with four different extracting solutions (Milli-Q, ammonium acetate solution, and diluted HNO_3 solutions with pH adjusted to 3 and 5) is within 1% of that determined using the standard squeezing method. Alkalinity, SO_4^{2-} , and PO_4^{3-} concentrations tend to be higher in the extracted solutions by the GRIND method, and Br^- concentration is lower than in the standard squeezed water. For SO_4^{2-} , the Milli-Q water extracted solution gave an

extremely high concentration compared with that in the other solutions, for which concentrations are comparable (within 5% error) to that in the standard squeezed water. Alkalinity of solution extracted by ammonium acetate was higher than those of the other extracted solutions because of the addition of ammonium ion to increase alkaline component. It is also clear that NH_4^+ increased in the extracted solution using ammonium acetate. Na^+ , Mg^{2+} , and Ca^{2+} concentrations became higher in the solutions extracted using the GRIND method than those using the standard squeezing method (again within 5% error). Among the major cations, K^+ concentration exceeds the 5% error range and is higher than that of the standard squeezing method. Minor alkaline and alkaline earth elements tend to give higher concentrations in the extracted solutions using the GRIND method than those using the standard squeezing method, except Sr, which has a concentration similar to that using the standard squeezing method. It is notable that the different extracting solutions do not seriously affect the analytical results of those elements.

Minor and trace elements that behave as oxoacid (neutral molecules and anions) increase in the extracted solutions by the GRIND method (Si, V, Mn, Mo, and U; Fig. [AF6](#)). Transition metals Fe, Cu, Zn, and Pb tend to increase in the extracted solutions by the GRIND method, and their behavior is complicated compared with the above elements. Among the analyzed transition metals, Mn concentration decreases in the extracted solutions by the GRIND method. In general, minor and trace element concentrations determined by the GRIND method cannot be used as alternatives to those of the standard squeezing method, except Sr and B, which differ slightly (2% error) from those values obtained by the standard squeezing method.

Conclusion

For the GRIND method, Milli-Q shows the best performance for accuracy of IW chemistry as an additional solution (Method 2-C), but only some components allow for use of the GRIND method instead of the standard squeezing method: alkalinity, chlorinity, Li, Na^+ , Mg^{2+} , Sr, and B. As an exception, only SO_4^{2-} concentration using Milli-Q was not consistent with that using the squeezing method. Therefore, for SO_4^{2-} concentration, in addition to Method 2-C we adopt Method 2-E using HNO_3 solution adjusted to pH 3.

Figure AF1. Comparison of pH, alkalinity, chlorinity, and concentrations of SO_4^{2-} and Br^- of the extracted solutions by three methods and different extraction solution conditions. 1-A = standard squeezing method using Milli-Q water, 2-A = GRIND method using Milli-Q water spiked with 500 ppb In, 2-B = GRIND method using Milli-Q water spiked with 500 ppb Lu, 3-A1 = leaching method after dried in air at 105°C and using Milli-Q water, 3-A2 = leaching method after dried in vacuum and using Milli-Q water, 3-B1 = leaching method without drying and using Milli-Q water, 3-B2 = leaching method without drying and using 20 μM $\text{CH}_3\text{COONH}_4$ solution, 3-B3 = leaching method without drying using 100 μM $\text{CH}_3\text{COONH}_4$ solution. Error bar = 10% except where noted in the figure.

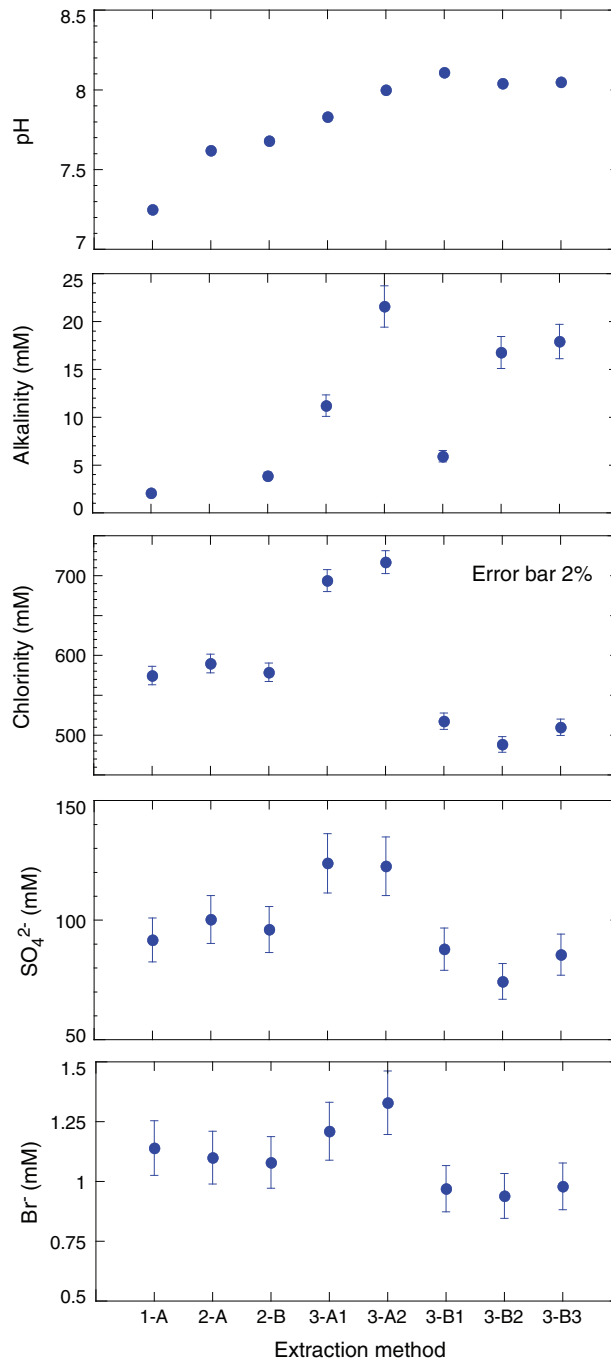


Figure AF2. Comparison of concentrations of Li, Na⁺, K⁺, Rb, Cs, NH₄⁺, Mg²⁺, Ca²⁺, Sr, and Ba. 1-A = standard squeezing method using Milli-Q water, 2-A = GRIND method using Milli-Q water spiked with 500 ppb In, 2-B = GRIND method using Milli-Q water spiked with 500 ppb Lu, 3-A1 = leaching method after dried in air at 105°C and using Milli-Q water, 3-A2 = leaching method after dried in vacuum and using Milli-Q water, 3-B1 = leaching method without drying and using Milli-Q water, 3-B2 = leaching method without drying and using 20 μM CH₃COONH₄ solution, 3-B3 = leaching method without drying using 100 μM CH₃COONH₄ solution. Error bar = 10% except where noted in the figure.

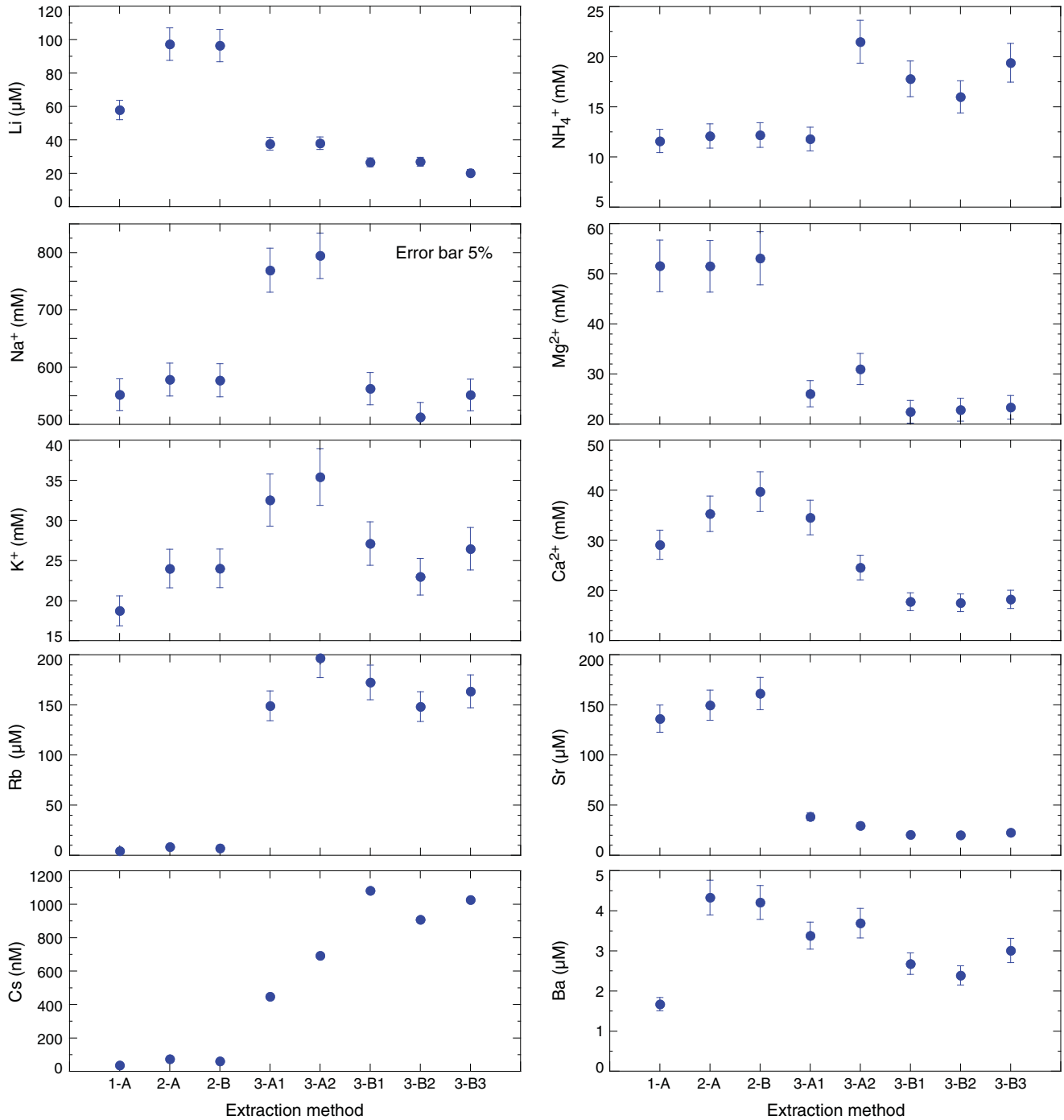


Figure AF3. Comparison of concentrations of B, Si, V, Mo, U, Mn, Fe, Cu, Zn, and Pb. 1-A = standard squeezing method using Milli-Q water, 2-A = GRIND method using Milli-Q water spiked with 500 ppb In, 2-B = GRIND method using Milli-Q water spiked with 500 ppb Lu, 3-A1 = leaching method after dried in air at 105°C and using Milli-Q water, 3-A2 = leaching method after dried in vacuum and using Milli-Q water, 3-B1 = leaching method without drying and using Milli-Q water, 3-B2 = leaching method without drying and using 20 μM $\text{CH}_3\text{COONH}_4$ solution, 3-B3 = leaching method without drying using 100 μM $\text{CH}_3\text{COONH}_4$ solution. Error bar = 10% except where noted in the figure.

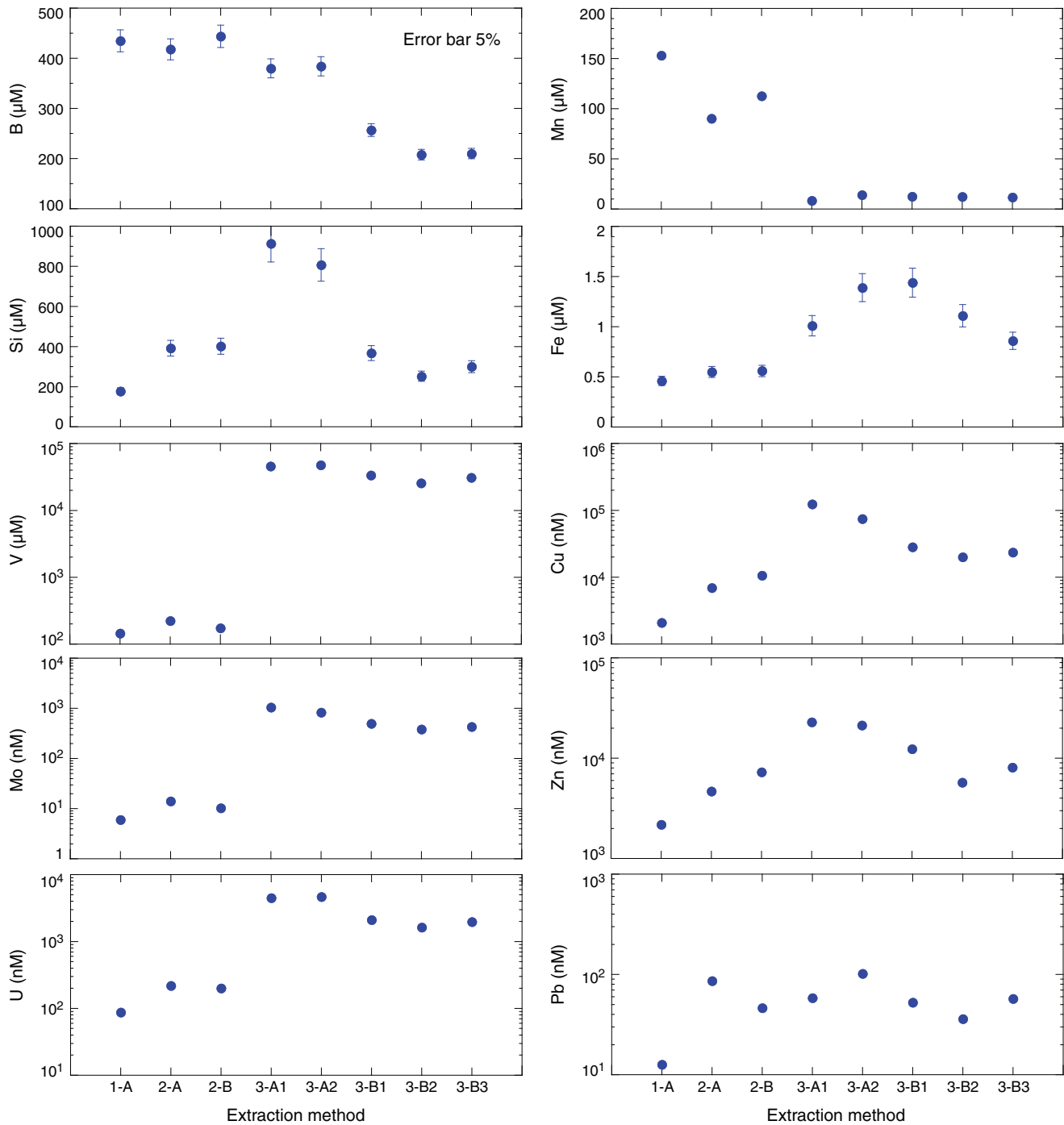


Figure AF4. Comparison of pH, alkalinity, chlorinity, and concentrations of SO_4^{2-} and Br^- of the extracted solutions by the standard squeezing and GRIND methods. 1-B = standard squeezing method using Milli-Q water, 2-C = GRIND method using Milli-Q water, 2-D = GRIND method using $100 \mu\text{M}$ $\text{CH}_3\text{COONH}_4$ solution, 2-E = GRIND method using diluted HNO_3 solution with pH adjusted to 3, 2-F = GRIND method using diluted HNO_3 solution with pH adjusted to 5. Error bar = 10% except where noted in the figure.

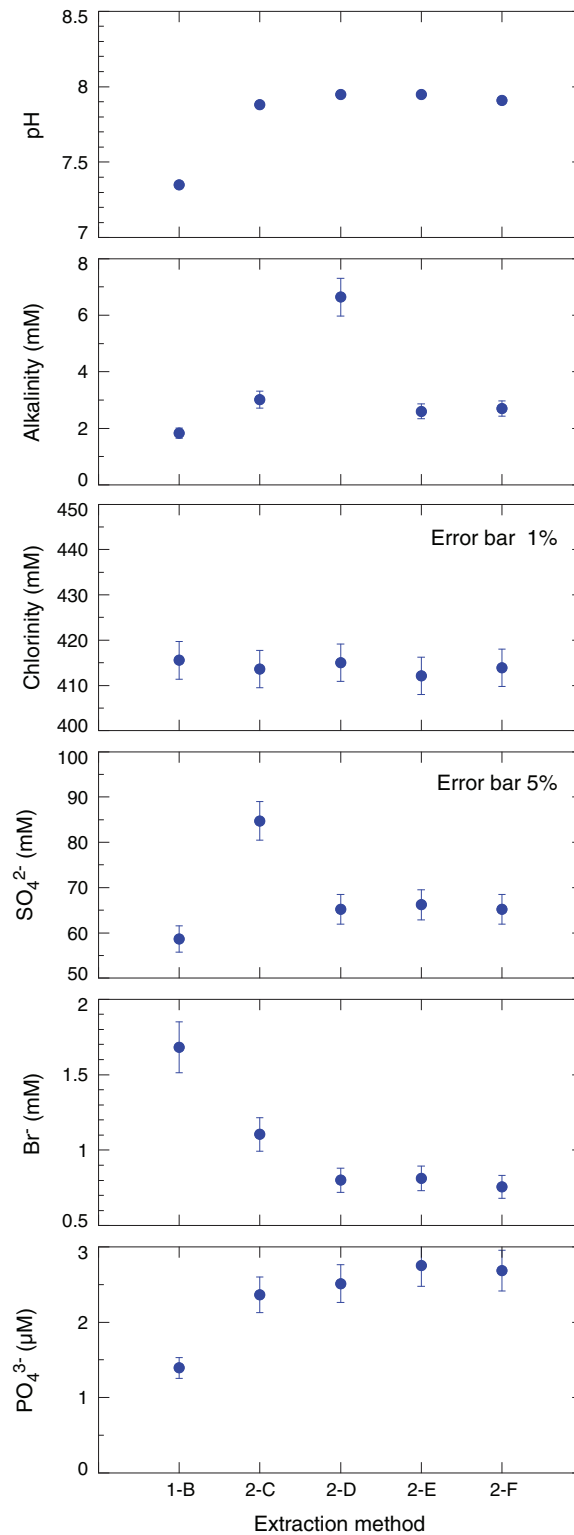


Figure AF5. Comparison of concentrations of Li, Na⁺, K⁺, Rb, Cs, NH₄⁺, Mg²⁺, Ca²⁺, Sr, and Ba. 1-B = standard squeezing method using Milli-Q water, 2-C = GRIND method using Milli-Q water, 2-D = GRIND method using 100 μM CH₃COONH₄ solution, 2-E = GRIND method using diluted HNO₃ solution with pH adjusted to 3, 2-F = GRIND method using diluted HNO₃ solution with pH adjusted to 5. Error bar = 10% except where noted in the figure.

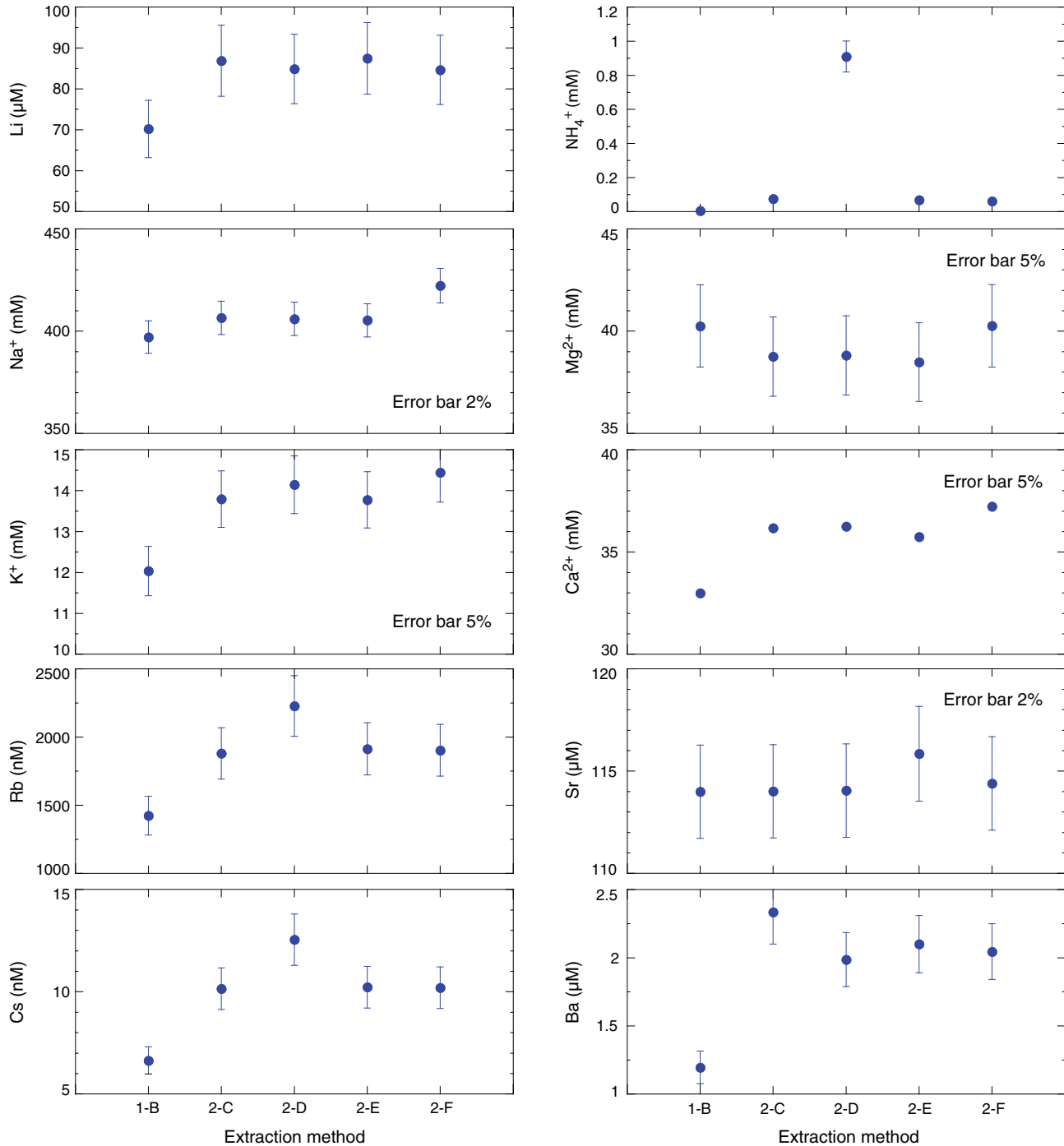


Figure AF6. Comparison of concentrations of B, Si, V, Mo, U, Mn, Fe, Cu, Zn, and Pb. 1-B = standard squeezing method using Milli-Q water, 2-C = GRIND method using Milli-Q water, 2-D = GRIND method using 100 μM $\text{CH}_3\text{COONH}_4$ solution, 2-E = GRIND method using diluted HNO_3 solution with pH adjusted to 3, 2-F = GRIND method using diluted HNO_3 solution with pH adjusted to 5. Error bar = 10% except where noted in the figure.

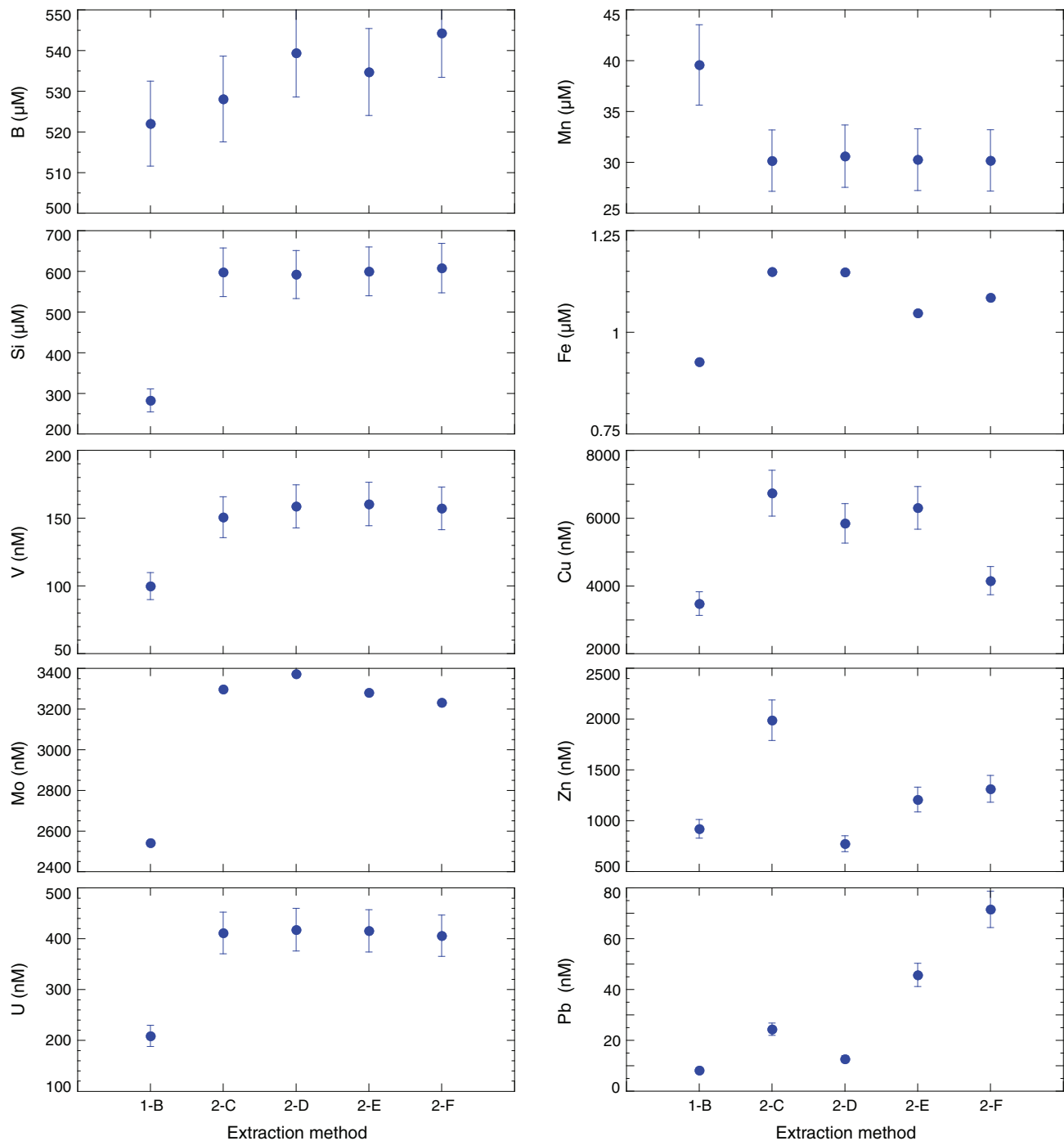


Table AT1. Interstitial water extraction methods tested, Expedition 338.

Experiment	Sample	Method	Sediment weight (g)	Sediment condition	Solution
1	1-A	Squeezing	~200	Untreated whole core	None
	2-A	GRIND	40	Crushed	5 mL 500 ppb In solution
	2-B	GRIND	40	Crushed	5 mL 500 ppb RLA solution
	3-A1	Leaching	4	Dried in air at 110°C and powdered	40 mL Milli-Q water
	3-A2	Leaching	4	Dried in vacuum and powdered	40 mL Milli-Q water
	3-B1	Leaching	4	Not treated	40 mL Milli-Q water
	3-B2	Leaching	4	Not treated	40 mL 20 μM $\text{CH}_3\text{COONH}_4$ solution
	3-B3	Leaching	4	Not treated	40 mL 100 μM $\text{CH}_3\text{COONH}_4$ solution
2	1-B	Squeezing	~200	Untreated whole core	None
	2-C	GRIND	80	Crushed	10 g Milli-Q water
	2-D	GRIND	80	Crushed	10 g 20 μM $\text{CH}_3\text{COONH}_4$ solution
	2-E	GRIND	80	Crushed	10 g pH 3 diluted HNO_3 solution
	2-F	GRIND	80	Crushed	10 g pH 5 diluted HNO_3 solution

GRIND = ground rock interstitial normative determination.

Table AT2. Concentration of spiked elements in the extracted solution, Expedition 338.

Extraction method	In (ppb)	Y (ppb)	Lu (ppb)
1-A	ND	0.2	ND
2-A	0.027	ND	0.008
2-B	ND	0.3	0.013
3-A1	ND	11.3	0.191
3-A2	ND	10.9	0.225
3-B1	ND	8.0	0.165
3-B2	ND	6.4	0.138
3-B3	ND	8.3	-0.058
In standard solution	506	ND	ND
REE standard solution	ND	432	427

ND = not detected. REE = rare earth element.

Table AT3. Comparison of water content analysis methods, Expedition 338.

Experiment	Extraction method	Drying condition	Sample weight (g)		Water content (wt%)
			Initial	Final	
1	3-A	105°C in air	21.0361	16.1362	23.3
	3-B	In a vacuum	21.2199	16.3483	23.0
					Average:
2	3-A	105°C in air	24.2288	16.4709	32.0



Table AT4. Analytical results of extracted solution chemistry, Expedition 338.

Extraction method	Dilution ratio	pH	Alkalinity (mM)	Chlorinity (mM)	Br ⁻ (mM)	SO ₄ ²⁻ (mM)	PO ₄ ³⁻ (μM)	NH ₄ ⁺ (mM)	Na ⁺ (mM)	K ⁺ (mM)	Mg ²⁺ (mM)	Ca ²⁺ (mM)	Li (μM)	B (μM)	Mn (μM)	Fe (μM)	Si (μM)
1-A	1.0	7.25	2.1	574.8	1.14	92	ND	11.6	552	18.7	51.6	29.1	57.9	435	153	0.46	177
2-A	1.5	7.62	NA	589.9	1.10	100	ND	12.1	578	24.0	51.5	35.3	97.3	418	90	0.55	392
2-B	1.5	7.68	3.9	578.9	1.08	96	ND	12.2	577	24.0	53.1	39.7	96.5	444	113	0.56	402
3-A1	38.3	7.83	11.2	693.9	1.21	124	ND	11.8	769	32.5	26.1	34.6	37.7	380	9	1.01	913
3-A2	44.0	8.00	21.6	717.0	1.33	123	ND	21.5	795	35.4	31.0	24.6	38.0	384	14	1.39	807
3-B1	42.0	8.11	5.9	517.5	0.97	88	ND	17.8	562	27.1	22.5	17.8	26.8	257	13	1.44	368
3-B2	38.6	8.04	16.8	488.5	0.94	74	ND	16.0	513	23.0	22.9	17.6	27.0	208	12	1.11	252
3-B3	45.3	8.05	17.9	510.0	0.98	86	ND	19.4	552	26.5	23.4	18.2	20.3	210	12	0.86	300
1-B	1.0	7.35	1.8	415.6	1.68	59	1.39	0.0	397	12.0	40.3	33.0	70.2	522	40	0.93	283
2-C	1.4	7.88	3.0	413.6	1.10	85	2.37	0.1	407	13.8	38.8	36.2	86.9	528	30	1.15	598
2-D	1.4	7.95	6.7	415.0	0.80	65	2.51	0.9	406	14.2	38.8	36.3	84.9	539	31	1.15	592
2-E	1.4	7.95	2.6	412.1	0.81	66	2.75	0.1	405	13.8	38.5	35.7	87.5	535	30	1.05	600
2-F	1.4	7.91	2.7	413.9	0.76	65	2.68	0.1	422	14.4	40.3	37.2	84.7	544	30	1.09	608

NA = not analyzed. ND = not detected.

Extraction method	Sr (μM)	Ba (μM)	V (nM)	Cu (nM)	Zn (nM)	Rb (nM)	Mo (nM)	Cs (nM)	Pb (nM)	U (nM)
1-A	136	1.67	145	2,092	2,180	4,264	6	36	13	87
2-A	150	4.33	224	6,966	4,688	8,450	14	74	86	219
2-B	161	4.21	175	10,623	7,276	7,210	10	62	46	201
3-A1	39	3.38	46,005	123,799	22,943	149,140	1,049	448	58	4,501
3-A2	30	3.69	47,756	74,747	21,325	196,817	830	694	102	4,653
3-B1	21	2.68	33,595	28,144	12,397	172,446	500	1,082	53	2,108
3-B2	20	2.39	25,578	20,105	5,723	148,289	383	908	36	1,634
3-B3	23	3.01	31,042	23,533	8,094	163,601	431	1,027	57	1,974
1-B	114	1.20	100	3,483	921	1,424	2,541	7	8	209
2-C	114	2.33	151	6,739	1,990	1,880	3,298	10	24	411
2-D	114	1.99	159	5,850	774	2,228	3,373	13	13	418
2-E	116	2.10	160	6,305	1,209	1,914	3,281	10	46	416
2-F	114	2.05	157	4,155	1,313	1,903	3,232	10	72	406

Appendix B

Contamination check for mud-gas monitoring

Method

Standard gas

We analyzed organic component gas using a GC-NGA, a MCIA, and a PGMS. The standard gas contains methane, ethane, propane, *iso*-butane, *n*-butane, and nitrogen. The concentration of each component except for nitrogen is 1%.

Settings

Standard gas was connected at the inlet of the mud trap (Fig. [BF1](#)). Secondary pressure of standard gas was slightly higher than atmospheric pressure. Pump settings in the mud-gas monitoring laboratory are shown in Table [BT1](#).

Devices

MCIA and PGMS were used to analyze standard gases. GC-NGA was applied in the same manner as for mud-gas monitoring (measuring with FID and TCD) during the contamination check.

Results

Gas flow rate injected into devices

During the contamination check, gas flow into the PGMS was controlled at 50 mL/min. For GC-NGA,

MCIA, and the radon analyzer, gas flow rate was confirmed (Table [BT2](#)). With the pump set at 0.5 L/min, gas flows for devices except for PGMS were not high enough.

Standard gas measurement

To evaluate contamination, standard gas was directly sampled and measured by MCIA and PGMS. These results are shown as a red line in Figure [BF2](#).

MCIA. Standard gas was taken with a gas-tight syringe and measured in syringe injection mode. Results are shown in Table [BT3](#).

PGMS. Standard gas was taken in a sampling bag. Then, the sampling bag was connected to the PGMS and standard gas was measured. Results are shown in Table [BT4](#).

Contamination check

Concentrations measured with MCIA and PGMS are shown in Figure [BF2](#). During the contamination check, oxygen concentrations were lower than 3%, and concentrations of other components were close to certified values. Methane concentrations measured by MCIA were almost the same as the results of syringe injection (see “[MCIA](#)”; Table [BT3](#)) while sufficient gas flowed into the MCIA. Consequently, the effects of air contamination between the mud trap and pump are probably small.

Figure BF1. Diagram of standard gas connection.

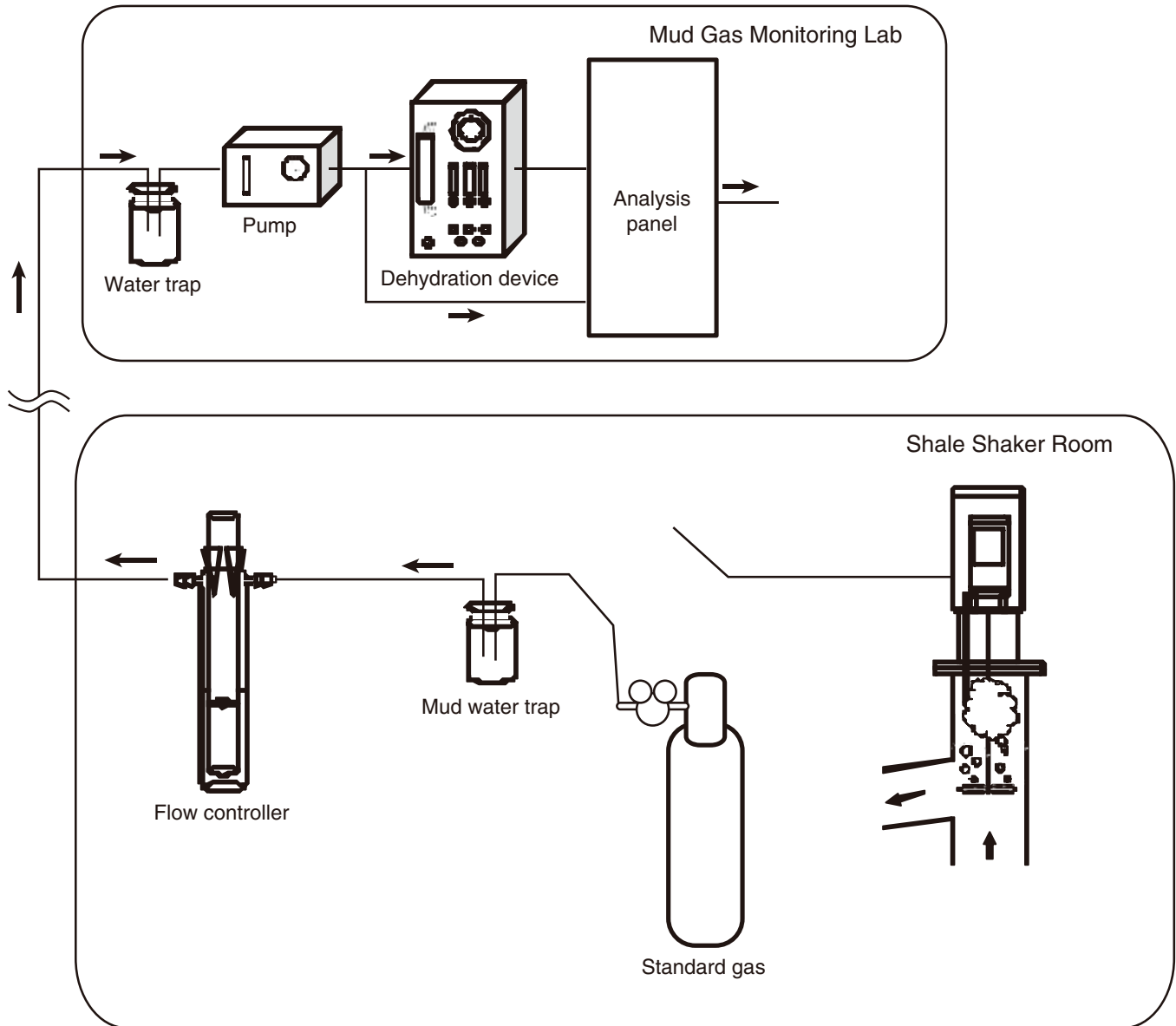


Figure BF2. Results of contamination check. MCIA = methane carbon isotope analyzer.

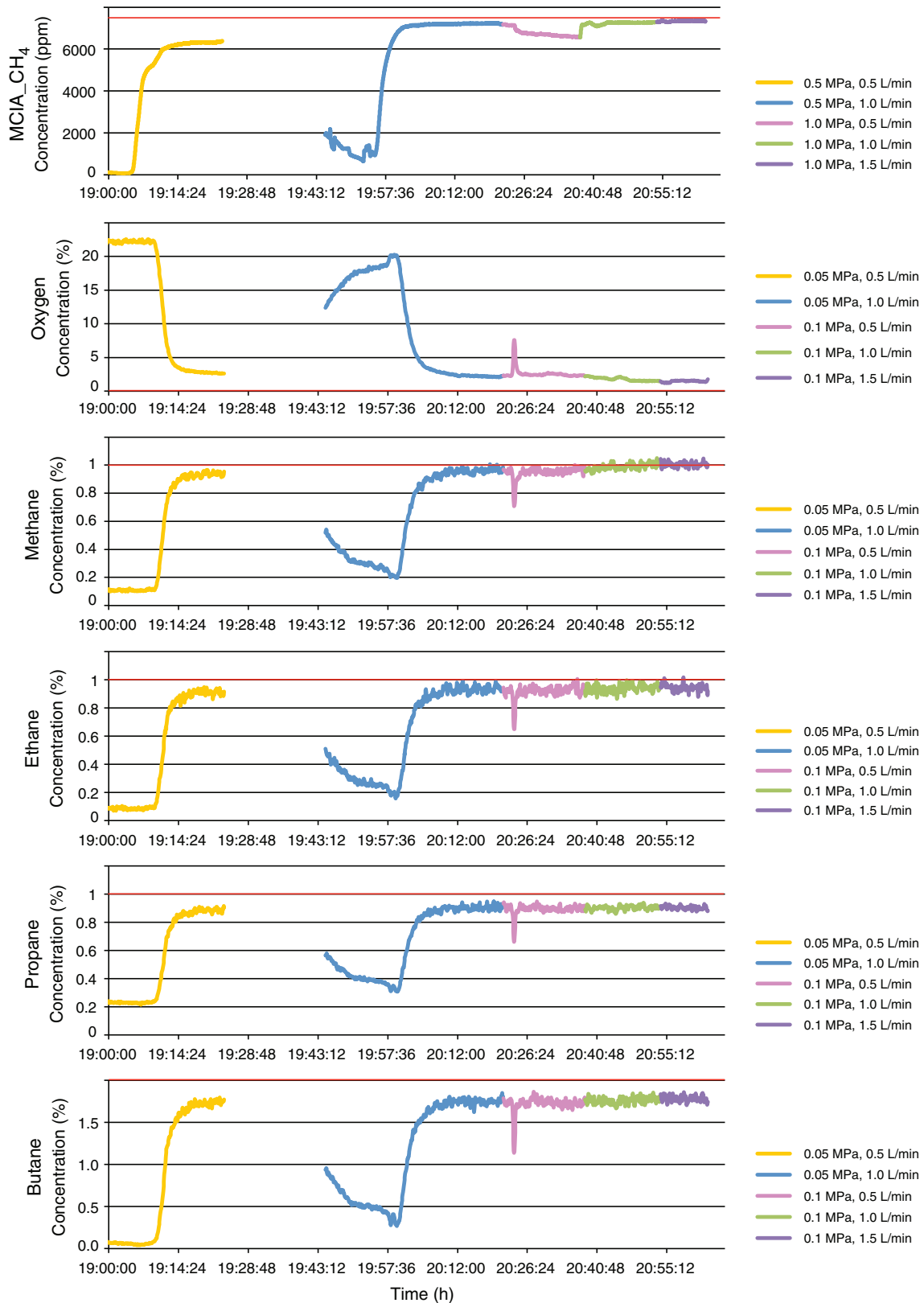


Table BT1. Pump settings.

	Pressure (MPa)	Flow rate (L/min)
1	0.05	0.5
2	0.05	1.0
3	0.1	0.5
4	0.1	1.0
5	0.1	1.5

Table BT2. Gas flow rate injected into each device.

	Pump settings		Gas flow rate		
	Pressure (MPa)	Flow rate (L/min)	GC-NGA 50 mL/min	MCIA 180 mL/min is needed	Rn analyzer 65 mL/min is needed
1	0.05	0.5	50	80	0
2	0.05	1.0	50	180	70
3	0.1	0.5	20	100	30
4	0.1	1.0	50	190	70
5	0.1	1.5	90	160	120

During gas chromatograph–natural gas analyzer (GC-NGA) measurement, flow rate is usually controlled at ~50 mL/min. MCIA = methane carbon isotope analyzer.

Table BT3. Result of standard gas measurement with MCIA.

Component	Concentration
CH ₄ (ppm)	7494.828 ± 0.51536
δ ¹³ C-CH ₄ (‰)	1.2882 ± 0.04097

Table BT4. Result of standard gas measurement with PGMS.

Component	Concentration (%)
H ₂	0.169434
He	0.002863
O ₂	0.271266
Ar	0.098272
Xe	0.000858
N ₂	93.82255
CO	0.21639
CO ₂	0.384431
CH ₄	1.063113
C ₂ H ₆	1.039551
C ₃ H ₈	0.997674
C ₄ H ₁₀	1.93361